AD_____

Award Number: W81XWH-06-1-0367

TITLE: Combined Contrast-Enhanced MRI and Fluorescence Molecular Tomography for Breast Tumor Imaging

PRINCIPAL INVESTIGATOR: Scott C. Davis

CONTRACTING ORGANIZATION: Dartmouth College
Hanover, NH 03755

REPORT DATE: March 2009

TYPE OF REPORT: Annual Summary

PREPARED FOR: U.S. Army Medical Research and Materiel Command
Fort Detrick, Maryland 21702-5012

DISTRIBUTION STATEMENT: Approved for Public Release;
Distribution Unlimited

The views, opinions and/or findings contained in this report are those of the author(s) and should not be construed as an official Department of the Army position, policy or decision unless so designated by other documentation.

REPORT DOCUMENTATION PAGE

Form Approved
OMB No. 0704-0188

Public reporting burden for this collection of information is estimated to average 1 hour per response, including the time for reviewing instructions, searching existing data sources, gathering and maintaining the data needed, and completing and reviewing this collection of information. Send comments regarding this burden estimate or any other aspect of this collection of information, including suggestions for reducing this burden to Department of Defense, Washington Headquarters Services, Directorate for Information Operations and Reports (0704-0188), 1215 Jefferson Davis Highway, Suite 1204, Arlington, VA 22202-4302. Respondents should be aware that notwithstanding any other provision of law, no person shall be subject to any penalty for failing to comply with a collection of information if it does not display a currently valid OMB control number. **PLEASE DO NOT RETURN YOUR FORM TO THE ABOVE ADDRESS.**

1. REPORT DATE *(DD-MM-YYYY)*	**2. REPORT TYPE**	**3. DATES COVERED** *(From - To)*
01-03-2009	Annual Summary	15 Feb 2006 - 14 Feb 2009

4. TITLE AND SUBTITLE

Combined Contrast-Enhanced MRI and Fluorescence Molecular Tomography for Breast Tumor Imaging

5a. CONTRACT NUMBER

5b. GRANT NUMBER
W81XWH-06-1-0367

5c. PROGRAM ELEMENT NUMBER

6. AUTHOR(S)
Scott C. Davis

E-Mail: scott.c.davis@dartmouth.edu

5d. PROJECT NUMBER

5e. TASK NUMBER

5f. WORK UNIT NUMBER

7. PERFORMING ORGANIZATION NAME(S) AND ADDRESS(ES)

Dartmouth College
Hanover, NH 03755

8. PERFORMING ORGANIZATION REPORT NUMBER

9. SPONSORING / MONITORING AGENCY NAME(S) AND ADDRESS(ES)
U.S. Army Medical Research and Materiel Command
Fort Detrick, Maryland 21702-5012

10. SPONSOR/MONITOR'S ACRONYM(S)

11. SPONSOR/MONITOR'S REPORT NUMBER(S)

12. DISTRIBUTION / AVAILABILITY STATEMENT
Approved for Public Release; Distribution Unlimited

13. SUPPLEMENTARY NOTES

14. ABSTRACT

A unique fluorescence molecular tomography system which couples fluorescence data acquisition into the bore of a clinical MRI to image the spatial distribution of fluorescence activity in tissue volumes has been developed and characterized. Signal-to-noise and system sensitivity to fluorophore concentration have been studied extensively. In homogeneous 70 mm diameter cylindrical phantoms, the system shows a linear response to fluorophore concentration down to 1 nM and is sensitive down to 10 pM. Images in realistic phantoms simulating breast tissue reveal the importance of the complimentary MRI information, especially in cases where the tumor to normal tissue fluorophore uptake is less than perfect. Reconstructing images using tissue morphology information from simultaneously acquired MRI images recover tumor regions down to contrasts of 1.5 to 1while images reconstructed without the MR information show no tumor specificity even at contrasts above 6 to 1.

15. SUBJECT TERMS
Tomography, fluorescence, imaging, near-infrared, diffuse optical tomography, fluorescence molecular tomography

16. SECURITY CLASSIFICATION OF:			**17. LIMITATION OF ABSTRACT**	**18. NUMBER OF PAGES**	**19a. NAME OF RESPONSIBLE PERSON**
a. REPORT	**b. ABSTRACT**	**c. THIS PAGE**			USAMRMC
U	U	U	UU	75	**19b. TELEPHONE NUMBER** *(include area code)*

Table of Contents

Page

Introduction…….. 4

Body……. 4

Key Research Accomplishments…….. 13

Reportable Outcomes……. 14

Conclusion……. 16

References……. 16

Appendices……. 16

Introduction

The scientific objective of this research was to develop and characterize an MRI-coupled fluorescence molecular tomography (FMT) system and associated reconstruction algorithms to image exogenous fluorescent agents in human breast. Imaging the spatial distribution of unspecific and/or targeted fluorescent probes may help determine whether a suspect region in an MRI image is indeed malignant, thus reducing the high number of false positives and associated biopsies, and aiding in treatment planning. Fluorescence imaging at depth in tissue is challenging for a number of reasons. The nature of non-invasive diffuse imaging requires detection at the tissue surface, making the data set fairly sparse compared with the volume of interest. This results in relatively poor resolution, depth dependent sensitivity, and inaccurate quantification, especially in complex tissue volumes such as human breast. Secondly, low levels of fluorescence emission are often swamped by excitation cross-talk from the exciting laser source. The FMT system here seeks to address both of these issues. Image resolution and quantification performance is addressed by incorporating the system into a clinical MRI for dual-modality image acquisition and using the MR image as a tissue structure template to guide the FMT image formation. Excitation contamination is addressed by using spectrometer-based detection systems which provide a unique opportunity to de-couple fluorescence and excitation signals using a spectral fitting routine. This report summarizes the major accomplishments completed during this fellowship.

Body

The work completed for this traineeship accomplished the proposed aims.

Aim 1: It was shown that the system is appropriately sensitive for FMT imaging during standard breast-MR protocols.

Aim 2: All results from numerical and phantom data showed dramatic improvements in imaging performance with MRI prior information incorporated into the imaging algorithm. In most cases, the MR information was required for accurate imaging and the image reconstruction problem was intractable without the MRI images.

Aim 3: Numerical and phantom data was used demonstrate FMT imaging in heterogeneous domains. It was shown that the MRI information is required to produce meaningful images in these complex, though realistic volumes.

Aim 4: This aim was revised when Pharmacyclics halted manufacturing of LuTex. The fluorescent drug used in these studies was transitioned to Indocyanine green (ICG), a non-specific fluorophore approved for use in humans. It was shown that ICG can be quantified down to at least 1 nM, much lower than the 50 μM concentrations required for most gadolinium-based MRI contrast agents.

Aim 5: It was shown that the signal producing the most sensitive measurement depends on the concentration of the drug. As drug concentration increases, the signal providing the most sensitive measurement transitions from fluorescence to absorption.

Imaging System

One of the primary accomplishments of this project was the design and development of a parallel spectrometer-based tomographic imaging system which couples into a Philips 3T MRI magnet. The system was developed to acquire spectrally resolved transmission, fluorescence emission, and bioluminescence spectra. Photographs and a diagram of the system are presented in Fig. 1. The spectroscopy system is composed of sixteen Insight spectrometers (Acton Research) with Pixis cooled CCD cameras which provide highly sensitive spectrally resolved detection of the collected light. Each spectrometer is coupled to the patient interface via a 13 meter bifurcated silica fiber (a total 16 fibers) custom designed for this system. These custom designed bifurcated fibers circumscribe the tissue volume being imaged and are used for both source delivery and detection. One end of each bifurcated fiber is coupled into a spectrometer through a custom designed and manufactured input optical unit, each of which contains an automated, six-position filter wheel to help filter the excitation laser source from the fluorescence signal. The input optics collimate the light from the fiber, pass it through a filter

of the user's choice, then focus the light on the spectrometer entrance slit matching the f-number of the spectrometer system. All spectrometers are controlled simultaneously with programs written in Labview which cycle the laser source sequentially through each fiber while the other 15 fibers detect the emitted light from the tissue volume, resulting in a total of 240 data points for a given acquisition. Exposure times are determined automatically during acquisition to optimize the SNR.

Imaging system characterization

In funding year two, a comprehensive characterization of the spectrometer-based fluorescence imaging system which included methodical assessments of measurement repeatability and system sensitivity to fluorescence activity was completed. Most of the information in this section is presented in a recent publication[1] (attached as Appendix), though the highlights are provided here. Repeatability measurements were made for two imaging modes, one records the intensity of the excitation source while the other filters the excitation light and measures the fluorescence emission intensity. An 8.6cm diameter homogeneous phantom composed of silicone, titanium dioxide, and India ink was used to measure the repeatability of transmission mode measurements using the spectroscopy system. Optical properties of the phantom were 0.004 mm^{-1} and 1.91 mm^{-1} for the absorption and reduced scattering coefficients respectively. The average and maximum standard errors are 0.28% and 0.37% for fibers remaining in contact with the phantom and 14.8% and16.3% for re-positioned fibers, indicating the larges source of error is fiber position. However, this can be addressed, as described below.

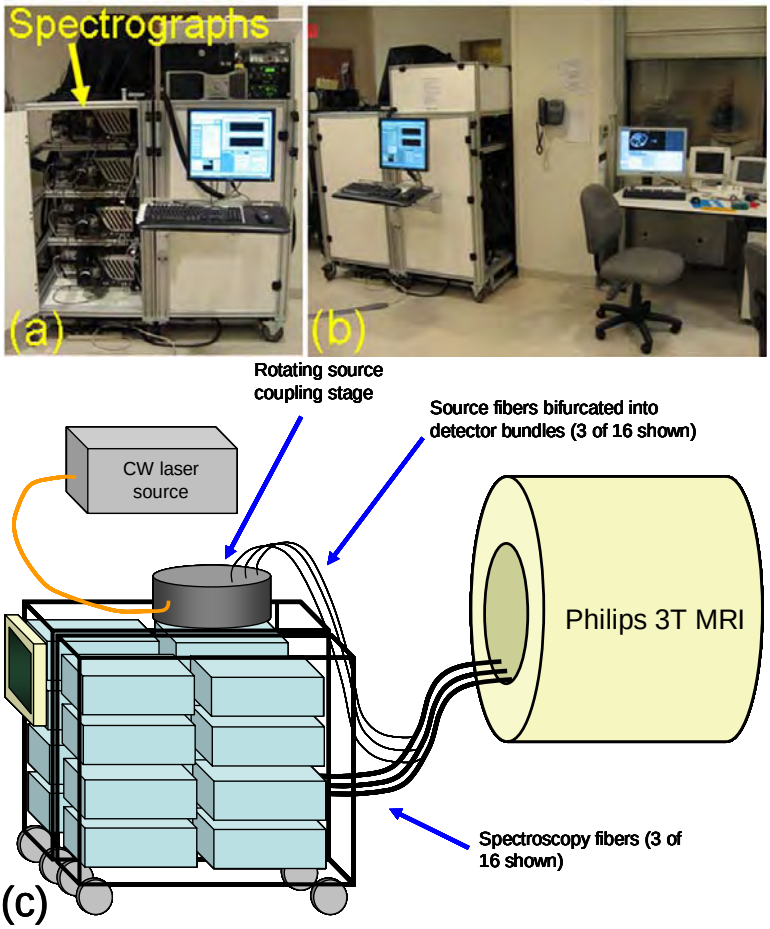

Figure 1. Photographs (a) and (b) and a diagram (c) of the experimental system in the MRI control room. Long fiber optics penetrate ports in the wall, extend into the bore of the magnet, and couple to the tissue with custom designed fiber arrays attached to a standard breast RF coil.

Determining measurement repeatability in fluorescence mode is less straightforward given the signal dependence on fluorophore concentration, absorption spectrum, and quantum yield. For this study, a 70 mm diameter liquid phantom containing DPBS, 1% intralipid, India ink. The fluorophore used in this study was indocayanine green (ICG), perhaps the most commonly used fluorophore for fluorescence tomography in phantoms. A concentration of 10nM ICG was used to determine measurement repeatability. Repeatability was calculated in two ways, one considered only the raw data for a given binned pixel array and resulted in a mean standard error of 0.7% and maximum standard error of 1.4% for the pixel array at the fluorescence peak. The second measure was determined based on the integrated intensity from the full calibration and spectral fitting routine, resulting in an average standard error of 0.6% and maximum standard error of 1.8%. It is clear that fiber positioning variability would dominate the data error for

fluorescence measurements in this case. However, fluorescence measurement data offers a unique opportunity to account for fiber coupling variability by calibrating the fluorescence measurements to the transmission measurements in the same geometry. This provides inherent stability to systematic error.

A 70 mm diameter liquid phantom containing DPBS, 1% intralipid and India ink was used to investigate the overall sensitivity of the system to Indocyanine green (ICG) fluorescence. Fluorescence emission and excitation transmission measurements were recorded for each phantom, with a maximum allowed camera integration time of 120 seconds applied to the fluorescence measurements. The typical data measured across the emission spectrum are shown in Fig. 2 (a) for a strong fluorescence signal and Fig. 2 (c) for a weak signal. The spectral fitting procedure was used to recover the true fluorescence signal and the non-specific background contributions, as shown in (b) and (d), respectively. Additionally, to quantitatively compare the spectral fitting procedure to more conventional means of fluorescence filtering, the measured, un-fitted spectra were integrated to simulate 720 nm long-pass filtering.

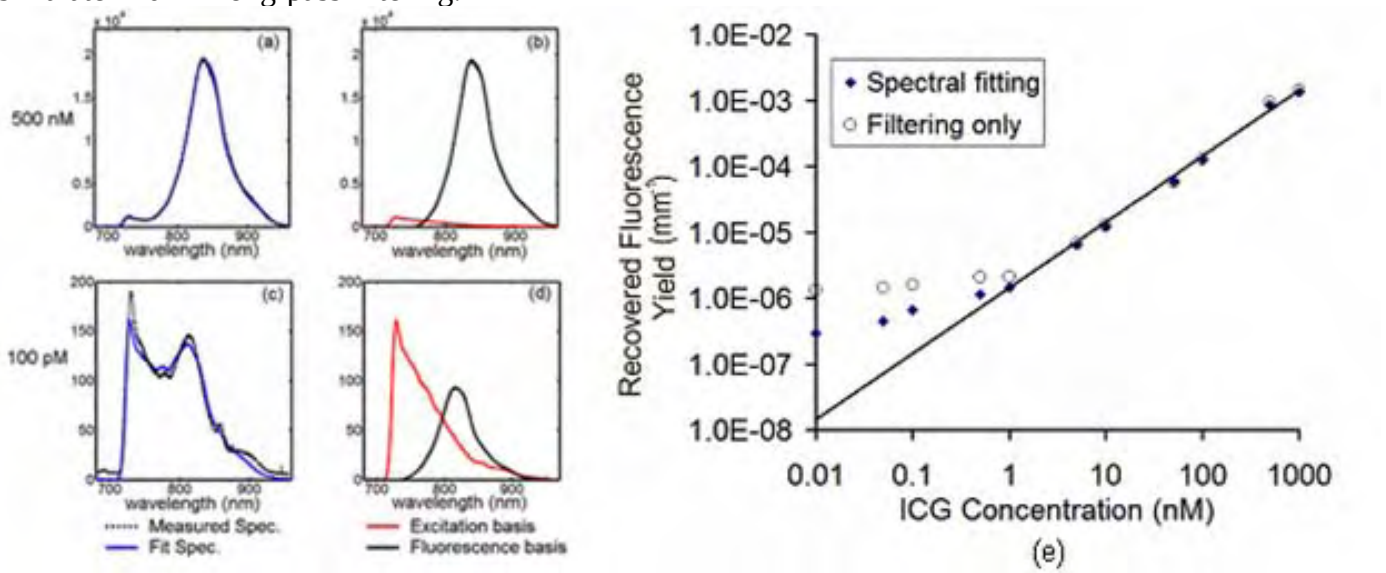

Figure 2. A spectral fitting routine is used to decouple fluorescence spectra from the measured signal. The spectral fitting algorithm determines the relative contribution of the basis spectra [right column, (b) and (d)] which best fits the measured spectrum. Two examples are presented above, both for a 70 mm diameter homogeneous phantom containing intralipid, ink and ICG [500 nM for graphs (a) and (b) and 100pM for graphs (c) and (d)]. Recovered values of fluorescence yield as a function of ICG concentration in a 70 mm liquid phantom using two methods to process the recorded data are shown in (e). One method implements the spectral-fitting technique to decouple background contamination across the fluorescence emission spectrum while the other simply integrates the measured spectrum, as would be the case if the experimental system relied on long pass filtering alone.

Values of fluorescence yield recovered using the two data pre-processing techniques are plotted as a function of known ICG concentration in Fig. 2 (e). The linear fit shown in the figure was computed using the spectrally fit data with the y-intercept forced to zero and indicates a strong linear correlation of recovered fluorescence yield and ICG concentration (R^2 = 0.99). At concentrations above 1 nM, the fluorescence yield values calculated using data that was filtered only, with no spectral fitting, closely matches the spectrally fit results. Fluorescence signals produced at these fluorophore concentrations dominate the detected signal, a finding consistent with the data shown in Fig. 2 (a-d). However, fluorescence yield values recovered with spectrally fit data maintain the linear relationship at lower concentrations than those recovered using data without the spectral separation of background contamination. Clearly, the two techniques diverge at 1 nM. At this concentration, the residuals between the recovered value of fluorescence yield and the linear approximation are 0.4% and 48% for the

spectrally fit and filtering-only approaches, respectively. As the fluorophore concentration drops below 1 nM, both techniques lose the consistent linear response observed at higher concentrations, though the filtered-only shows even less sensitivity to changes in fluorophore concentration. At 500 pM, the residuals increase to 57% and 192% for the spectrally fit and filtered-only data processing responses, respectively. Below this level, accurate quantification of fluorescence activity is unlikely in this phantom configuration, however, the spectrally fit data still shows a stronger response to changes in fluorophore concentration down to 10 pM. The residuals calculated at the lowest concentration measured were almost 5 times larger without spectral fitting, clearly indicating a more sensitive, if not accurate, response of the spectral pre-processing technique. It should be noted that since fluorophore quantum yield is not explicitly known in this solution, the calculated slope of the linear regression does not provide information on the actual relationship between true and recovered concentration, however, the linearity itself is a critical measure of system performance.

Imaging clinically relevant volumes

Funding year 2006-2007 resulted in a series of phantom images of fluorescence yield in cases where perfect drug uptake was assumed and demonstrated dramatic improvements in imaging performance when MRI structural information was used to guide the fluorescence recovery procedure [2]. These studies provided an initial feasibility validation, however, perfect uptake experimental conditions are unrealistic for clinical applications since even targeted drugs are expected to produce background signals in healthy tissue regions. In this report, images of clinically relevant breast-sized tissue volumes were produced showing recovered images of low contrast fluorescence activity.

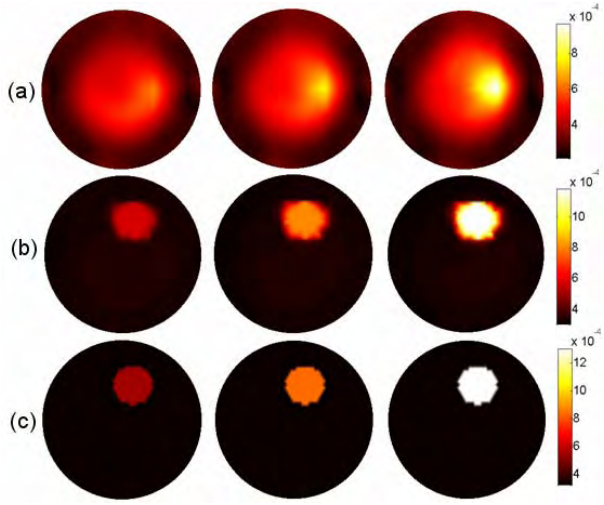

Figure 3. Reconstructed images of fluorescence yield for liquid phantoms containing intralipid, ink and ICG, using no spatial priors (a), soft priors (b) and hard priors (c). In this case, the simulated tumor region was close to the edge. Columns correspond to different tumor-to-background ICG contrasts, 1.5:1, 3.3:1, and 6.6:1 from left to right.

Ninety two millimeter diameter cylindrical liquid phantoms composed of DPBS, 1% intralipid, and India ink were used to investigate the imaging sensitivity for cases of imperfect drug uptake. A 22 mm diameter cylindrical plastic tube was suspended in the larger phantom volume to simulate a tumor region of elevated fluorophore concentration. The background liquid contained 300 nM of ICG while the tumor region was composed of the same intralipid solution but with varying concentrations of the fluorophore, to produce a range of tumor to background fluorophore concentrations between 6.6:1 to 1.5:1, or 560% to 50% contrast, respectively. Images were produced using three reconstruction techniques. One technique assumes only the outer boundary of the domain is known. The other two techniques use the internal structure of the phantom, as would be determined by simulateneously acquired MR images, to guide the fluorescence recovery. This information is applied either as strict knowledge of the internal anatomy, ("hard priors"), or as a regulatization filter matrix which is more flexible in terms of guiding the solution ("soft priors") [2].

Reconstructed images using all techniques are shown in Fig. 3. It is clear that in this relatively large domain with imperfect drug uptake, reconstructing images without the tissue morphology information produces qualitatively inaccurate and misleading images. The tumor region is not qualitatively or quantitatively recovered even at the higher contrast levels. The spatial priors techniques, on the other hand, essentially reduce the imaging problem from one of both localization and quantification to one of quantification only since the

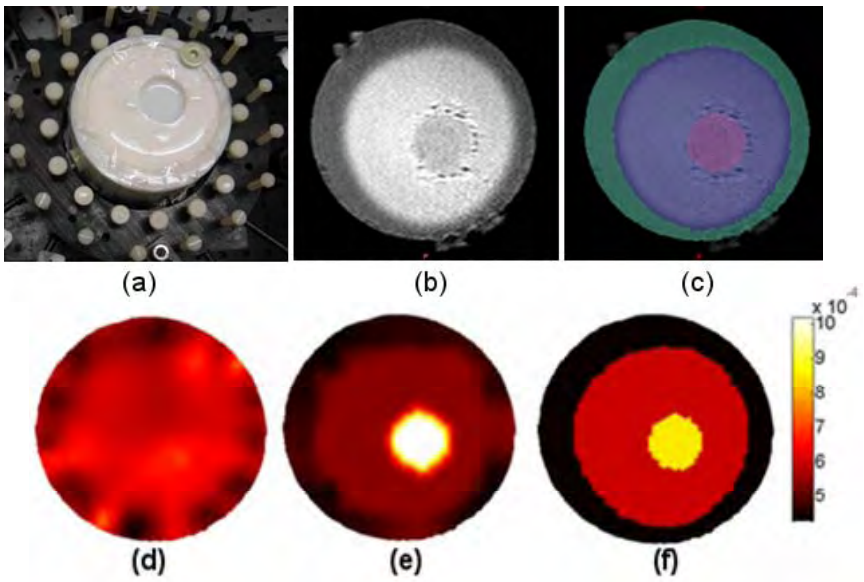

Figure 4. A photograph of the phantom in the optical fiber array is shown in (a). The second layer contained gadolinium, which provided MR image contrast, (b), for easy image segmentation using Mimics software (c). Fluorescence yield images of the three layer phantom reconstructed using no spatial guidance (d), soft-priors (e), and hard-priors (f). All images are plotted using the same color scale.

boundaries of the tumor are specified by the MR image. In this case, the tumor region is clearly visible in the image, even down to the lowest contrasts of 50%. The improvement provided by the spatially guided reconstruction is even more dramatic for cases of imperfect uptake, presented here, than for infinite contrast cases. This is an important result since in vivo concentrations will likely be closer to those used in this study.

Despite the added difficulty of imaging imperfect drug uptake, the phantoms used above are still relatively simple compared to the heterogeneous structure of breast tissue. Optically, the organ can be considered as a composition of a small number of optically significant tissue types; adipose tissue, fibro-glandular tissue, and suspect regions (benign and malignant tumors, cysts). In order to investigate the imaging capabilities of the fluorescence tomography system in heterogeneous imaging volumes, a more complex phantom was created using gelatin. The 91mm diameter cylindrical phantom was composed of water, gelatin, TiO_2 for scattering, and ICG. The resulting phantom is pictured in Fig. 4 which shows the three layers; the outer layer represents adipose tissue, the second layer fibroglandular tissue, and the small cylindrical inclusion is the simulated tumor region. ICG concentrations provide a tumor to adipose contrast of 10 to 1 and a tumor to fibroglandular contrast of around 3.3 to 1. Gadolinium was also added to the second layer so that each simulated tissue region would be discernable an MRI scan for use as spatial prior information. MRI and optical data were collected and the MR images segmented to provide spatial guidance (hard and soft priors techniques) of the fluorescence reconstructions. Resulting images are shown in Fig. 4 for the spatially guided and unguided reconstructions. As is clear from the images, spatial information is critical to obtain accurate images in complex domains.

Absorption tomography for imaging exogenous contrast

Another approach to image exogenous contrast uses the optical absorption characteristics of a contrast agent rather than the emitted light from a fluorescent contrast agent. A "spectrally constrained" approach which recovers images of endogenous tissue chromophore (oxy and deoxy hemoglobin, water) concentrations and scattering parameters using the chromophores' known spectral absorption profiles as prior information has been shown in previous studies to accurately image the endogenous chromophore concentration in human breast [3] [4] [5, 6]. Under the current grant, this approach has been expanded to incorporate exogenous absorbing drugs. Simulation studies have been completed which demonstrate simultaneous recovery of endogenous and exogenous chromophores and scattering parameters using multi-wavelength spectrally-constrained absorption tomography. The target values of endogenous and exogenous Lutex chromophore concentrations depicted in Fig. 5 were used to generate simulated noisy frequency domain data at ten discrete wavelengths. This data was used to complete a spectrally constrained reconstruction to recover images of the target domain. The results presented in Fig. 5 indicate reasonable qualitative and quantitative accuracy for the recovery of both the endogenous chromophores as well as LuTex.

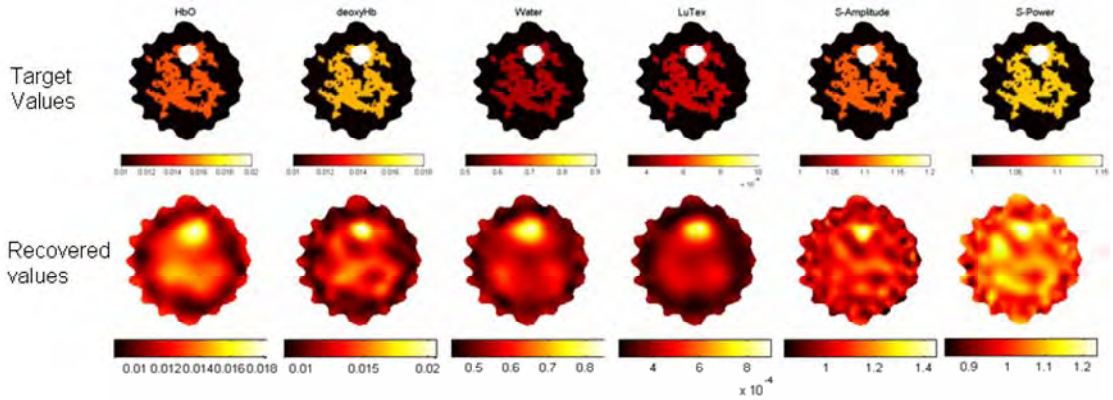

Figure 5. Target and recovered values of endogenous and exogenous chromophore in a realistic breast volume. Images were reconstructed using a spectrally constrained technique which incorporates the spectral absorption features as prior knowledge.

Comparing absorption and fluorescence imaging

This study addressed the question of which optical property provides the best opportunity for imaging exogenous optical contrast directly by comparing the intensity perturbation of boundary data caused by the presence of an exogenous absorber to that caused by an exogenous fluorophore. A breast-shaped domain derived from an MRI scan provides the imaging test field for this simulation study. The "background" domain contains no tumor region and presents endogenous chromophore contrast only between the fatty and fibro-glandular regions, as shown in Fig. 6. Also represented in the study are two different tumor-to-normal drug uptake situations, one an idealized case with infinite contrast [Fig. 6 (a)], and the other a more realistic drug uptake case resulting in finite contrast (ranging from 2:1 to 3:1) in drug concentration [Fig. 6 (b)]. In both cases exogenous absorption and fluorescence contrast was introduced as a simulated drug with absorbing properties of Lutex. Fluorescence quantum yield was varied as an independent variable for the fluorescence emission measurements.

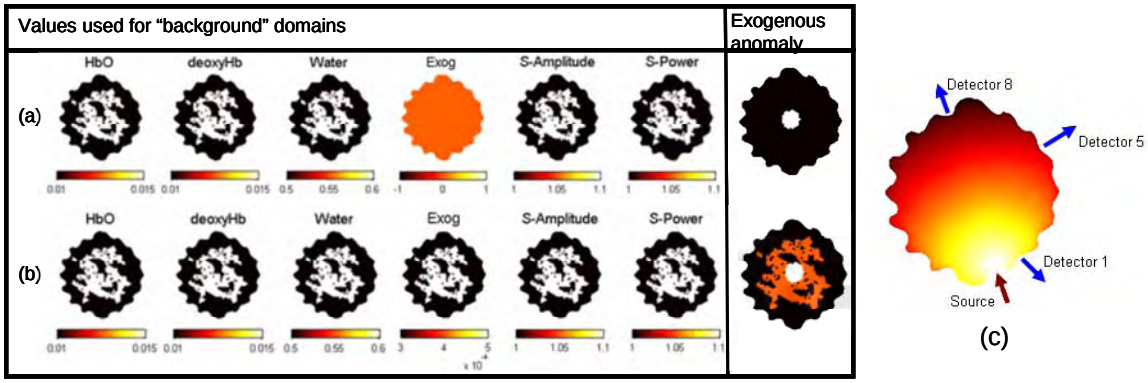

Figure 6. Two test domains for investigating perturbations caused by absorption and fluorescence exogenous contrast. In (a), exogenous contrast tumor specificity is assumed to be perfect, while in (b), the uptake profile is more realistic. The source-detector configuration is shown in (c).

The parameter of interest in this study is the relative perturbation in boundary data intensity caused by a drug-enhanced tumor. Data from perturbations caused only by exogenous *absorption* are termed "transmission" measurements, for which 735 nm was used as the laser source wavelength. Fluorescence data was generated for excitation and emission wavelengths of 690 and 761 nm and the fluorescence emission perturbation was recorded as a function of fluorescence quantum yield for excitation filtering efficiencies of 3 OD, 5 OD and 7 OD. Perturbation values were calculated for three detector positions relative to a single source, as shown in Fig. 6 (c), for both transmission and fluorescence measurements.

Figure 7 presents graphs of relative intensity perturbation as a function of fluorescence quantum yield at three detector positions for infinite exogenous agent contrast, corresponding to the test domain in Fig. 6 (a). The graphs include perturbations of transmission intensity resulting only from an increase in the concentration of the exogenous agent as well as fluorescence emission intensity degraded by different amounts of excitation bleed-through. The perturbation caused by absorption is unaffected by quantum yield while perturbations in fluorescence signals are proportional to quantum yield.

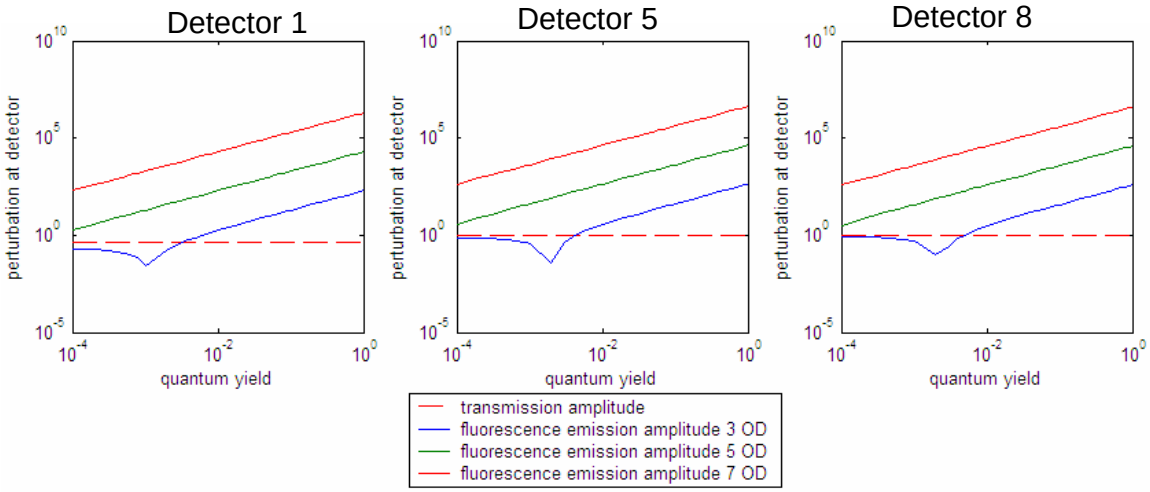

Figure 7. Perturbations in transmission amplitude and fluorescence amplitude, given different filtering efficiencies and quantum yield values, caused by a centrally located object with perfect drug uptake. Under these conditions, fluorescence signals appear to be more sensitive to the object.

It is clear from Fig. 7 that if the tissue contains infinite tumor-to-background contrast of exogenous agent concentration the fluorescence signal is more sensitive to the presence of the drug within the imaging domain. This is consistent for all source-detector pairs and filtering efficiency of 5 OD and higher given quantum yields of 0.0001 and above. These results substantiate a conclusion favoring fluorescence imaging, however, many contrast agents, including all optical agents currently approved for in vivo human use, will not provide infinite specificity and imperfect uptake must also be considered.

Figure 8 provides results for the case with drug uptake of 2:1 for tumor-to-fibro-glandular tissue layer and 3:1 for tumor-to-fatty tissue. For this case, the absorption perturbation is shown to be more significant for all values of quantum yield and filtering efficiencies tested. Significantly, these values represent the maximum expected perturbation for fluorescent anomalies and are significantly lower than perturbations caused by the absorption profile of the exogenous drug.

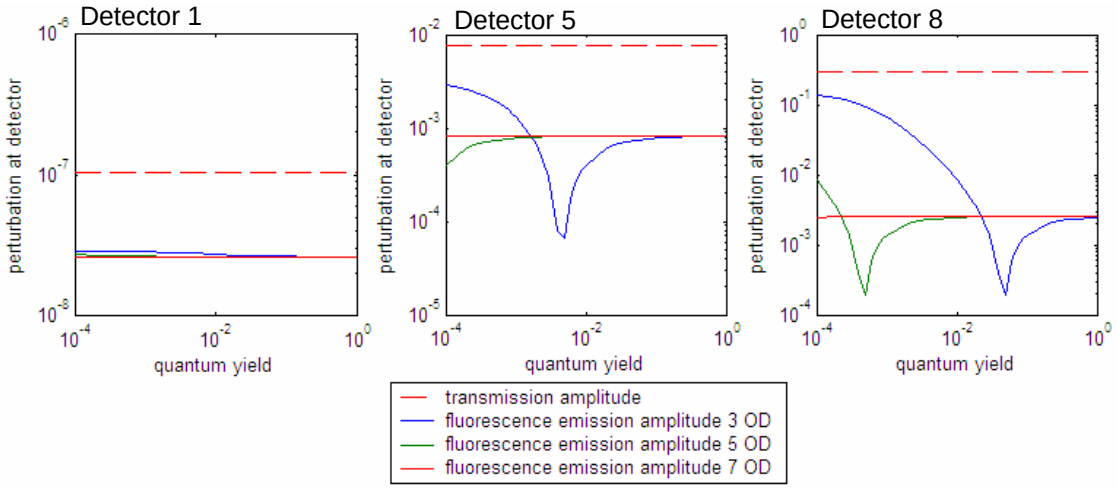

Figure 8. Perturbations in transmission amplitude and fluorescence amplitude, given different filtering efficiencies and quantum yield values, caused by a centrally located object with imperfect drug uptake. For this lower drug contrast case, absorption measurements are more sensitive to the object than fluorescence emission, regardless of fluorescence quantum yield.

The quantum yield value at which fluorescence and transmission perturbations intersect, i.e. the quantum yield threshold, was determined for drug contrasts ranging from 1.1:1 to 10:1, and background concentrations ranging from 10 nM to 1000 nM. The secant root finding method, initialized with the output of a bisection method algorithm, was used to determine the quantum yield value which minimizes the difference between fluorescence and transmission perturbations over the range $\eta = 10^{-6}$ to $\eta = 1$ for each combination of contrast and background concentration. The exogenous contrast distribution was assumed to be homogeneous except for the tumor region and only detector #4 was considered for this experiment.

Threshold quantum yield values as a function of background drug concentration for a single contrast value (5:1 in this case) are presented in Fig. 9. These curves represent the minimum value of quantum yield required to ensure fluorescence measurements are more sensitive to the tumor region than transmission measurements for a range of excitation filtering efficiencies. In this manner, regimes may be defined based on contrast agent quantum yield and expected background concentration. Regions above and to the left of a given curve represent a "fluorescence sensitive" regime while background/quantum yield combinations below and to the right of each curve can be considered "absorption sensitive", assuming a 5:1 target-to-background contrast. This is illustrated in Fig. 9 (b) for the 7 OD filter results. Conditions clearly favor transmission measurements when background drug concentration approaches 150 nM, regardless of filtering efficiency. On the lower concentration side of this hard limit, excitation filtering efficiency has a large impact on threshold quantum yield values. As filtering

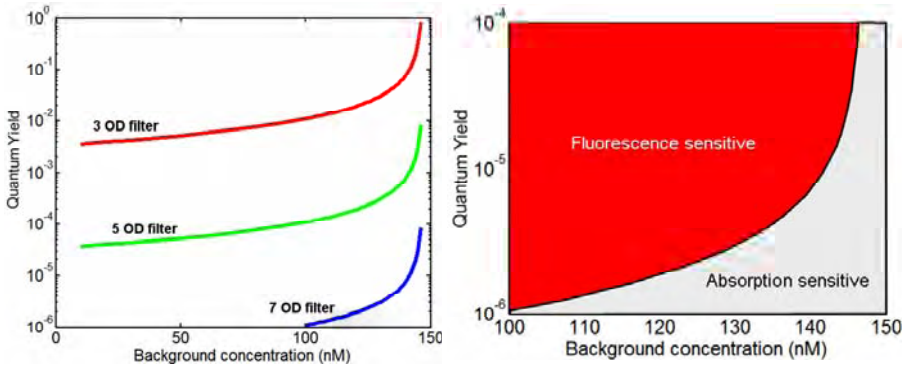

Figure 9. Threshold quantum yield values plotted as a function of background drug concentration for a 5:1 tumor-to-background contrast (a). The quantum yield threshold curves delineate between experimental conditions which favor fluorescence and absorption measurements (b).

efficiency degrades, higher and higher quantum yields are required to produce meaningful fluorescence perturbations at the tissue boundary.

LuTex fluorescence emission peak shift in turbid phantoms

The influence of tissue optical properties on the shape of near-infrared (NIR) fluorescence emission spectra propagating through multiple centimeters of tissue was investigated. The results of this study will be appearing in the Journal of Applied Physics [7] and the highlights are summarized here. Experimentally measured fluorescence emission spectra measured in 6 cm homogeneous tissue phantoms shows dramatic spectral distortion which results in emission peak shifts of up to 60 nm in wavelength. Measured spectral shapes are highly dependent on the photon path-length and the highly scattered photon field in the NIR amplifies the wavelength-dependent absorption of the fluorescence spectra. Simulations of the peak propagation using diffusion modeling describe the experimental observations and confirm the path-length dependence of fluorescence emission, as shown in Fig. 10. Spectral changes are largest for longer path-length measurements, and this will be most dominant in human tomography studies in the NIR. Spectrally resolved or multi-wavelength band-pass measurements are required to detect these changes, and may be essential to interpret such effects, which would otherwise be attributed to erroneous intensity measurement. This phenomenon is analogous to beam hardening in x-ray tomography, which can lead to image artifacts without appropriate compensation. The peak shift toward longer wavelengths, and therefore lower energy photons, observed for NIR luminescent signals propagating through tissue may readily be described as a "beam softening" phenomenon. These spectral changes should be considered for fluorescence tomographic imaging through several centimeters of tissue. Use of spectrally resolved detection allows quantification of this change, and may be the only reliable

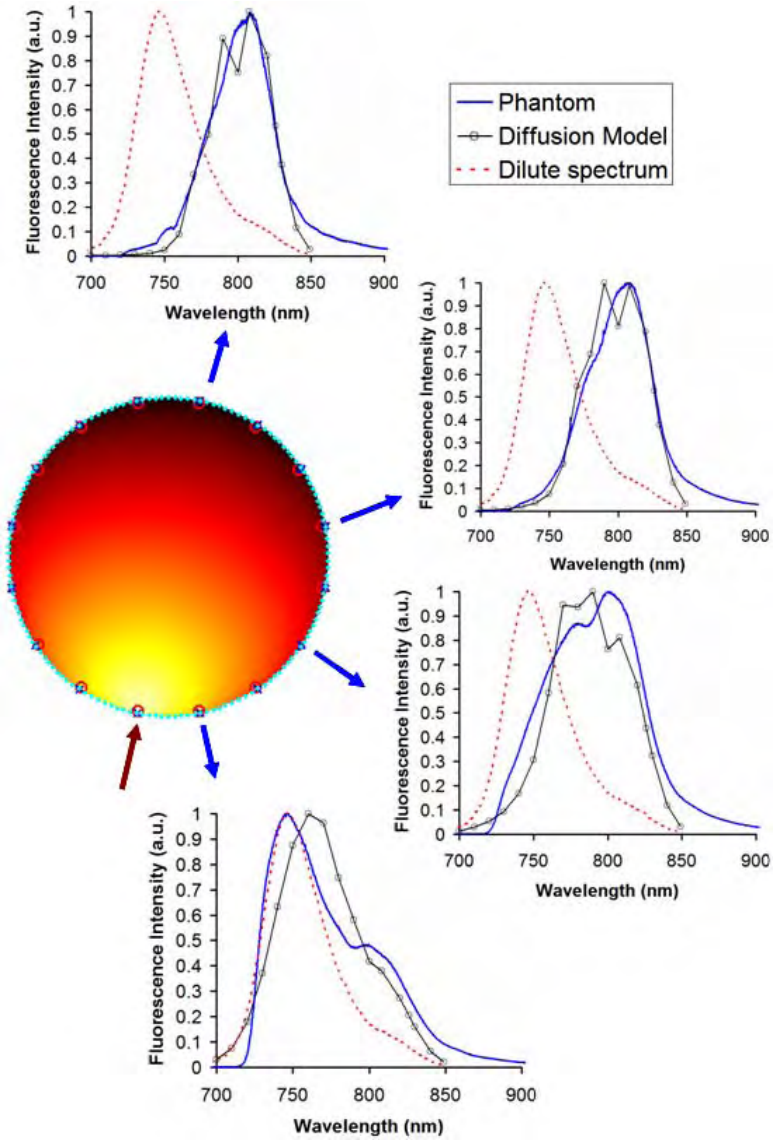

Figure 10. Diffusion based modeling of the fluorescence peak through a 60 mm diameter phantom. The dilute emission spectrum of LuTex is shown as dotted lines, and the calculated emission spectrum from diffuse emission through the region is shown at discrete wavelengths (black circles). Experimental measurements are shown in blue for intralipid liquid phantoms. The circular domain shown represents a cross-section of the cylindrical phantom upon which the intensity (logarithm) of the excitation field calculated from the diffusion equation is plotted for illustration purposes.

way to track intensity changes which would otherwise appear erroneous.

Contrast-detail analysis

A contrast-detail study using simulated data was completed to determine the imaging limits of the reconstruction algorithm[8]. Two circular domains, one 51 and the other 86 mm diameter, were used as test fields and object (simulated tumor) locations near the edge and center of each domain were considered. The contrast-detail results for a threshold contrast-to-noise limit of three or greater are plotted in Fig. 11 for two test fields and object positions. Objects which are recovered with greater than CNR = 3 have contrast-detail characteristics which are above and to the right of the lines shown in Fig. 11 and are thus considered detectable, while those below and to the left are too small or have too little contrast to be recovered with CNR>3 in the image. Accordingly, the limiting diameter for an object near the edge of the field is approximately 1.7 mm for both test field diameters. There seems to be little influence of test field diameter on CNR limits for high-contrast objects near the edge. Above an object contrast of about 8, the continued decrease in the minimum size for CNR = 3, is very small with increasing contrast, indicating that this size is a fundamental limit of the imaging algorithm for this geometry. This high contrast, small detail portion of the curve is often referred to as a "spatial resolution limited" regime. It does not appear that the fundamental limits have been reached for objects near the center of either test field for the contrast range studied and expected to be encountered experimentally. Furthermore, CNR value of objects near the center is strongly influenced by the test field size. For a 51 mm test object, the limiting diameter is approximately 4 mm, for the maximum object contrast (10). This increases to approximately 8.5 mm for the larger test field. These results indicate the dramatic decrease in sensitivity for objects deeper in the test field.

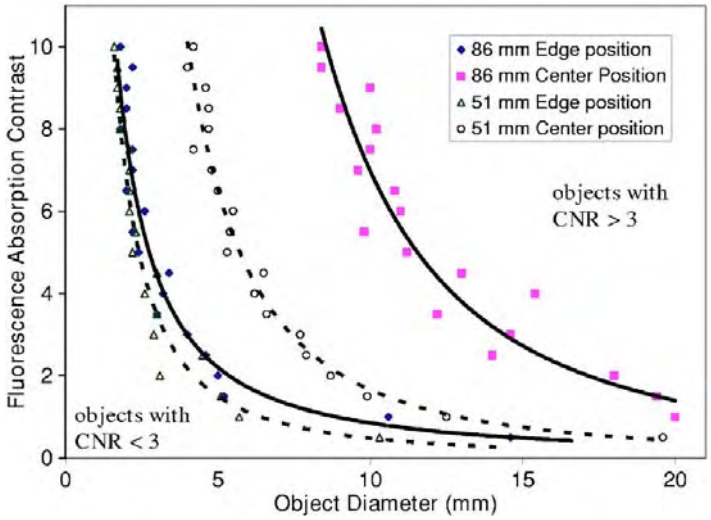

Figure 11. Contrast-detail curve showing the contrast-to-noise ratio (CNR) of 3 to approximate limits of detectable contrast and diameter for two anomaly positions in 51 mm (dashed lines) and 86 mm (solid lines) diameter test fields. In this analysis, objects above and to the right of each line are in the region where CNR ≥ 3 and detection is considered possible.

Key research accomplishments

- Constructed and calibrated experimental system and completed comprehensive system performance studies to determine signal-to-noise and sensitivity to contrast agent concentration characteristics.
- Incorporated tissue structural information obtained from MR images into the image reconstruction algorithms and demonstrated a dramatic qualitative and quantitative improvement in imaging performance using numerical and phantom data.
- Developed and tested algorithms for simultaneous reconstruction of endogenous and exogenous chromophores based on absorption.
- Produced images of fluorescence yield in breast-sized phantoms with imperfect drug uptake.
- Compared measurement sensitivity to contrasts arising from optical absorption and fluorescence signals in simulated breast domains and defined regions for which each signal provides more sensitive measurements based on contrast and overall concentration.
- Observed fluorescence emission peak shift propagating through turbid media and developed software to

model phenomenon accurately.
- Determined imaging limits of the numerical algorithm using contrast-detail analysis.

Reportable outcomes

This fellowship led to three first peer-reviewed publications, three oral presentations and two poster presentations. These are listed below along with non-first author publications and conference proceedings.

Peer-reviewed publications

1. Dehghani H, **Davis SC**, Jiang SD, Pogue BW, Paulsen KD, Patterson MS, "Spectrally resolved bioluminescence optical tomography," Optics Letters, 31(3):365–367 (2006).
2. Pogue BW, **Davis SC**, Song XM, Brooksby BA, Dehghani H, Paulsen KD, "Image analysis methods for diffuse optical tomography," J. Biomed Optics, 99(3):033001:1-12 (2006).
3. Kepshire DS, **Davis SC**, Dehghani H, Paulsen KD, Pogue BW, "Sub-Surface Diffuse Optical Tomography can Localize Absorber and Fluorescent Objects but Recovered Image Sensitivity in Non-Linear with Depth," Applied Optics, 46(10):1669–1678 (2007).
4. **Davis SC**, Dehghani H, Wang J, Jiang S, Pogue BW, Paulsen KD, "Image-guided diffuse optical fluorescence tomography implemented with Laplacian-type regularization," Optics Express, 15(7):4066–4082, 2007.
5. Kepshire D, **Davis SC**, Dehghani H, Paulsen KD, Pogue BW, "Fluorescence tomography characterization for sub-surface imaging with protoporphyrin IX," Optics Express 16(12):8581-8593 (2008).
6. **Davis SC**, Pogue BW, Springett R, Leussler C, Mazurkewitz P, Tuttle SB, Gibbs-Strauss SL, Jiang S, Dehghani H, , Paulsen KD, "Magnetic resonance-coupled fluorescence tomography scanner for molecular imaging of tissue," Review of Scientific Instruments, 79-064302-1-10 (2008).
7. Dehghani H, Eames ME, Yalavarthy PK, **Davis SC**, Srinivasan S, Carpenter CM, Pogue BW, Paulsen KD, "Near-infrared optical tomography using NIRFAST: Algorithms for numerical model and image reconstruction algorithms," Communications in Numerical Methods in Engineering , (Accepted 2008).
8. Wang J, **Davis SC**, Srinivasan S, Jiang S, Pogue BW, Paulsen KD, "Spectral tomography with diffuse near-infrared light: inclusion of broadband frequency-domain spectral data," Journal of Biomedical Optics (In press 2008).
9. **Davis SC**, Pogue BW, Tuttle SB, Dehghani H, Paulsen KD, "Luminescence peak distortion in diffuse molecular spectroscopy of tissue," Journal of Applied Physics, (Accepted 2008).

First author conference presentations and posters

1. Poster: "MR-coupled multi-spectral diffuse NIR imaging system for exogenous fluorescence and absorption Tomography," Optical Society of America: Biomedical Optics Topical Meeting, Ft. Lauderdale, FL (March, 2006).
2. Poster: "Multi-spectral, MR-guided diffuse optical tomography for imaging fluorescence and absorption Exogenous Contrast," Society for Molecular Imaging: Hilton Waikoloa Village, HI (August 2006).
3. Presentation: "MR-guided reconstruction of fluorescence diffuse optical tomography," SPIE: Photonics West, San Jose, CA (January 2007).
4. Presentation: "MR-coupled molecular imaging of cancer in nude mice and breast-sized domains," SPIE: Photonics West, San Jose, CA (January 2008).
5. Presentation: "MR-coupled molecular imaging of tissue," Optical Society of America: Biomedical Optics Topical Meeting," St. Petersburg, FL (March, 2008).

Conference Proceedings

1. **Davis SC**, Pogue BW, Srinivasan S, Dehghani H and Paulsen KD, "Development of spectrally-constrained diffuse optical tomography for imaging exogenous contrast agents", Biomedical Optics Topical Meeting on CD-ROM (The Optical Society of America, Washington, DC), March 19-22, (2006).
2. Jiang S, Pogue BW, **Davis SC**, Paulsen KD, "Multispectral NIR diffuse optical tomography system development", Biomedical Optics Topical Meeting on CD-ROM (The Optical Society of America, Washington, DC), March 19-22, (2006).
3. Kepshire DS, Gibbs SL, **Davis SC**, Dehghani H, Paulsen KD, Pogue BW, "Diffuse fluorescence tomography analysis of B-scan mode geometry", Biomedical Optics Topical Meeting on CD-ROM (The Optical Society of America, Washington, DC), March 19-22, (2006).
4. Carpenter CM, Pogue BW, Yalavarthy PK, **Davis SC**, Jiang S, Dehghani H, Paulsen KD, "Analysis of 3-dimensional reconstruction in a MR-guided NIR tomography system", Biomedical Optics Topical Meeting on CD-ROM (The Optical Society of America, Washington, DC), March 19-22, (2006).
5. **Davis SC**, Dehghani H, Yalavarthy PK, Pogue BW, Paulsen KD, "Comparing two regularization techniques for diffuse optical tomography," Proc. SPIE 6434, 64340X (2007).
6. Kepshire DS, **Davis SC**, Dehghani H, Paulsen KD, Pogue BW, "Challenges in sub-surface fluorescence diffuse optical imaging," Proc. SPIE 6434, 64340R (2007).
7. Srinivasan S, Pogue BW, **Davis SC**, and Leblond F, "Improved quantification of fluorescence in 3-D in a realistic mouse phantom," Proc. SPIE 6434, 64340S (2007).
8. Dehghani H, Pogue BW, **Davis SC**, Patterson MS, "Modeling and image reconstruction in spectrally resolved bioluminescence tomography," Proc. SPIE 6434, 64340V (2007).
9. Wang J, **Davis SC**, Jiang S, Pogue BW, Paulsen KD, "Convergence analysis and preliminary experimental feasibility for MRI-localized region spectroscopy with NIR diffuse optical tomography," Proc. SPIE 6434, 64341B (2007).
10. Kepshire DS, Gibbs SL, **Davis SC**, Dehghani H, Paulsen KD, Pogue BW, "Sub-surface fluorescence imaging of Protoporphyrin IX with B-Scan mode tomography," Proc. SPIE 6139, 61391F (2006)
11. Pogue BW, Zhou X, Gibbs SL, **Davis SC**, Kepshire D, Paulsen KD, Hasan T, "Comparison of techniques for quantification of fluorescence from tissue." Proc. SPIE 6139, 61390N (2006)
12. Pogue BW, Li Z, Carpenter CM, Laughney AL, Krishnaswamy V, **Davis SC**, Jiang S, Paulsen KD, "System design for spectrally encoded video-rate near infrared tomography during magnetic resonance imaging of the breast," Proc. of SPIE 6850, 68500K (2008).
13. Gibbs-Strauss SL, **Davis SC**, O'Hara JA, Hoopes JP, Hasan T, Pogue BW, "Noninvasive murine glioma detection improved following photobleaching of skin PpIX fluorescence," Proc. of SPIE 6845, 68450D (2008).
14. **Davis SC**, Gibbs-Strauss SL, Tuttle SB, Jiang S, Springett R, Dehghani H, Pogue BW, Paulsen KD, "MRI-coupled spectrally-resolved fluorescence tomography for in vivo imaging," Proc. of SPIE 6850, 68500K (2008).
15. **Davis SC**, Gibbs-Strauss SL, Dehghani H, Pogue BW, Paulsen KD, "MRI-coupled fluorescence tomography of murine glioma metabolic activity," Biomedical Optics Topical Meeting on CD-ROM (The Optical Society of America, Washington, DC), March 16-20 (2008).

Conclusions

The work completed as part of this fellowship has produced a working MRI-FMT system and comprehensive assessments of the critical parameters. Results using this system demonstrate a linear response to fluorophore concentration down to 1 nM in 70 mm cylindrical phantoms. Importantly, images were produced of complex

phantoms simulating relatively low tumor to normal tissue contrasts, i.e., poor drug specificity, using spatially guided reconstruction techniques available only to systems incorporated into clinical imaging modalities which provide morphological information of the breast tissue. In all cases studied, the multi-modal imaging approach improved fluorescence imaging performance dramatically and in many cases, was a necessary condition for producing extracting any fluorescence activity contrast in the image.

Simulation studies of realistic breast domains compared perturbations caused by changes in fluorescence and absorption signals arising from tumor uptake of a fluorescent or absorbing optical agent. Results indicate drug concentration is a major factor determining which optical signal provides the stronger data response. Finally, an observed fluorescence peak shift in turbid media was modeled numerically. These spectral changes should be considered for fluorescence tomographic imaging through several centimeters of tissue. Use of spectrally resolved detection allows quantification of this change, and may be the only reliable way to track intensity changes which would otherwise appear erroneous.

References

1. S. C. Davis, B. W. Pogue, R. Springett, C. Leussler, P. Mazurkewitz, S. B. Tuttle, S. L. Gibbs-Strauss, S. S. Jiang, H. Dehghani, and K. D. Paulsen, "Magnetic resonance-coupled fluorescence tomography scanner for molecular imaging of tissue," Rev. Sci. Instr. **79** (2008).
2. S. C. Davis, H. Dehghani, J. Wang, S. Jiang, B. W. Pogue, and K. D. Paulsen, "Image-guided diffuse optical fluorescence tomography implemented with Laplacian-type regularization," Optics Express **15**, 4066-4082 (2007).
3. A. Corlu, T. Durduran, R. Choe, M. Schweiger, E. M. Hillman, S. R. Arridge, and A. G. Yodh, "Uniqueness and wavelength optimization in continuous-wave multispectral diffuse optical tomography," Optics Letters **28**, 2339-2341 (2003).
4. A. Li, Q. Zhang, J. Culver, E. Miller, and D. Boas, "Reconstructing chromophore concentration images directly by continuous-wave diffuse optical tomography," Optics Letters **29**, 256-258 (2004).
5. S. Srinivasan, B. W. Pogue, B. Brooksby, S. Jiang, H. Dehghani, C. Kogel, W. A. Wells, S. P. Poplack, and K. D. Paulsen, "Near-Infrared Characterization of Breast Tumors In Vivo using Spectrally-Constrained Reconstruction," Technology in Cancer Research and Treatment **4**, 513-526 (2005).
6. S. Srinivasan, B. W. Pogue, S. Jiang, H. Dehghani, C. Kogel, S. Soho, J. J. Gibson, T. D. Tosteson, S. P. Poplack, and K. D. Paulsen, "In vivo hemoglobin and water concentrations, oxygen saturation, and scattering estimates from near-infrared breast tomography using spectral reconstruction," Acad. Radiol. **13**, 195-202 (2006).
7. S. C. Davis, B. W. Pogue, S. B. Tuttle, H. Dehghani, and K. D. Paulsen, "Spectral Distortion in Diffuse Molecular Luminescence Tomography of Tissue," Applied Physics (in press) (2008).
8. S. C. Davis, B. W. Pogue, H. Dehghani, and K. D. Paulsen, "Contrast-detail analysis characterizing diffuse optical fluorescence tomography image reconstruction," Journal of Biomedical Optics Letters **10**, 1-3 (2005).

Appendix

The relevant journal article manuscripts have been attached.

Image-guided diffuse optical fluorescence tomography implemented with Laplacian-type regularization

Scott C. Davis,[1] Hamid Dehghani,[1,2] Jia Wang[1], Shudong Jiang[1], Brian W. Pogue[1] and Keith D. Paulsen[1]

[1]*Thayer School of Engineering, Dartmouth College, Hanover, New Hampshire 03755*
[2]*School of Physics, University of Exeter, Exeter, UK EX4 4QL*
Scott.C.Davis@dartmouth.edu, Brian.W.Pogue@dartmouth.edu

Abstract: A promising method to incorporate tissue structural information into the reconstruction of diffusion-based fluorescence imaging is introduced. The method regularizes the inversion problem with a Laplacian-type matrix, which inherently smoothes pre-defined tissue, but allows discontinuities between adjacent regions. The technique is most appropriately used when fluorescence tomography is combined with structural imaging systems. Phantom and simulation studies were used to illustrate significant improvements in quantitative imaging and linearity of response with the new algorithm. Images of an inclusion containing the fluorophore Lutetium Texaphyrin (Lutex) embedded in a cylindrical phantom are more accurate than in situations where no structural information is available, and edge artifacts which are normally prevalent were almost entirely suppressed. Most importantly, spatial priors provided a higher degree of sensitivity and accuracy to fluorophore concentration, though both techniques suffer from image bias caused by excitation signal leakage. The use of spatial priors becomes essential for accurate recovery of fluorophore distributions in complex tissue volumes. Simulation studies revealed an inability of the "no-priors" imaging algorithm to recover Lutex fluorescence yield in domains derived from T1 weighted images of a human breast. The same domains were reconstructed accurately to within 75% of the true values using prior knowledge of the internal tissue structure. This algorithmic approach will be implemented in an MR-coupled fluorescence spectroscopic tomography system, using the MR images for the structural template and the fluorescence data for region quantification.

© 2007 Optical Society of America

OCIS codes: (170.0110) imaging systems; (170.6280) spectroscopy, fluorescence and luminescence; (170.6960) tomography; 170.3010 image reconstruction techniques; (170.1610) clinical applications.

References

1. D. Y. Paithankar, A. U. Chen, B. W. Pogue, M. S. Patterson, and E. M. Sevick-Muraca, "Imaging of fluorescent yeild and lifetime from multiply scattered light reemitted from random media," Appl. Opt. **36**, 2260-2272 (1997).
2. H. B. Jiang, "Frequency-domain fluorescent diffusion tomography: a finite- element-based algorithm and simulations," Appl. Opt. **37**, 5337-5343 (1998).
3. D. J. Hawrysz, and E. M. Sevick-Muraca, "Developments toward diagnostic breast cancer imaging using near-infrared optical measurements and fluorescent contrast agents," Neoplasia **2**, 388-417 (2000).
4. M. J. Eppstein, D. J. Hawrysz, A. Godavarty, and E. M. Sevick-Muraca, "Three-dimensional, Bayesian image reconstruction from sparse and noisy data sets: near-infrared fluorescence tomography," Proc. Natl. Acad. Sci. USA **99**, 9619-9624 (2002).
5. A. B. Milstein, O. Seungseok, K. J. Webb, C. A. Bouman, Q. Zhang, D. A. Boas, and R. P. Millane, "Fluorescence optical diffusion tomograhy," Appl. Opt. **42**, 3081-3094 (2003).
6. V. Ntziachristos, and R. Weissleder, "Experimental three-dimensional fluorescence reconstruction of diffuse media by use of a normalized Born approximation," Opt. Lett. **26**, 893-895 (2001).

#78716 - $15.00 USD Received 4 January 2007; revised 22 February 2007; accepted 13 March 2007
(C) 2007 OSA

7. V. Ntziachristos, and R. Weissleder, "Charge-coupled-device based scanner for tomography of fluorescent near-infrared probes in turbid media," Med. Phys. **29**, 803-809 (2002).
8. E. Graves, J. Ripoll, R. Weissleder, and V. Ntziachristos, "A submillimeter resolution fluorescence molecular imaging system for small animal imaging," Med. Phys. **30**, 901-911 (2003).
9. A. Godavarty, A. B. Thompson, R. Roy, M. Gurfinkel, M. J. Eppstein, C. Zhang, and E. M. Sevick-Muraca, "Diagnostic imaging of breast cancer using fluorescence-enhanced optical tomography: phantom studies," J. Biomed. Opt. **9**, 488-496 (2004).
10. R. B. Schulz, J. Ripoll, and V. Ntziachristos, "Experimental fluorescence tomography of tissue with noncontact measurements," IEEE Trans. Med. Imaging **23**, 492-500 (2004).
11. S. V. Patwardhan, S. R. Bloch, S. Achilefu, and J. P. Culver, "Time-dependent whole-body fluorescence tomography of probe bio-distribution in mice," Opt. Exp. **13**, 2564-2577 (2005).
12. A. Godavarty, M. J. Eppstein, C. Zhang, and E. M. Sevick-Muraca, "Detection of single and multiple targets in tissue phantoms with fluorescence-enhanced optical imaging: feasibility study," Radiol. **235**, 148-154 (2005).
13. B. Brooksby, S. Jiang, C. Kogel, M. Doyley, H. Dehghani, J. B. Weaver, S. P. Poplack, B. W. Pogue, and K. D. Paulsen, "Magnetic resonance-guided near-infrared tomography of the breast," Rev. Sci. Instrum. **75**, 5262-5270 (2004).
14. X. Intes, C. Maloux, M. Guven, B. Yazici, and B. Chance, "Diffuse Optical tomography with physiological and spatial a priori constraints," Phys. Med. Biol. **49**, N155-N163 (2004).
15. M. Guven, B. Yazici, X. Intes, and B. Chance, "Diffuse optical tomography with a priori anatomical information," Phys. Med. Biol. **50**, 2837-2858 (2005).
16. P. K. Yalavarthy, H. Dehghani, B. W. Pogue, C. M. Carpenter, H. B. Jiang, and K. D. Paulsen, "Structural information within regularization matrices improves near infrared diffuse optical tomography," IEEE Trans. Med. Imaging **In review** (2006).
17. G. Kostenich, A. Orenstein, L. Roitman, Z. Malik, and B. Ehrenberg, "In vivo photodynamic therapy with the new near-IR absorbing water soluble photosensitizer lutetium texaphyrin and a high intensity pulsed light delivery system," Photochem. & Photobiol. **39**, 36-42 (1997).
18. K. W. Woodburn, Q. Fan, D. R. Miles, D. Kessel, Y. Luo, and S. W. Young, "Localization and efficacy analysis of the phototherapeutic lutetium texaphyrin (PCI-0123) in the murine EMT6 sarcoma model," Photochem. & Photobiol. **65**, 410-415 (1997).
19. M. Zellweger, A. Radu, P. Monnier, H. van den Bergh, and G. Wagnieres, "Fluorescence pharmacokinetics of Lutetium Texaphyrin (PCI-0123, Lu-Tex) in the skin and in healthy and tumoral hamster cheek-pouch mucosa," Photochem. & Photobiol. B **55**, 56-62 (2000).
20. A. Synytsya, V. Kral, P. Matejka, P. Pouckova, K. Volka, and J. L. Sessler, "Biodistribution assessment of a lutetium(III) texaphyrin analogue in tumor-bearing mice using NIR Fourier-transform Raman spectroscopy," Photochem. & Photobiol. **79**, 453-460 (2004).
21. H. Dehghani, B. Brooksby, K. Vishwanath, B. W. Pogue, and P. K. D., "The effects of internal refractive index variation in near infrared optical tomography: A finite element modeling approach," Phys. Med. Biol. **48**, 2713-2727 (2003).
22. S. R. Arridge, M. Schweiger, M. Hiraoka and D. T. Delpy, "A finite element approach for modeling photon transport in tissue," Med. Phys. **20**, 299-309 (1993).
23. K. D. Paulsen, and Jiang H., "Spatially varying optical property reconstruction using a finite element diffusion equation approximation," Med. Phys. **22**, 691-701 (1995).
24. S. R. Arridge, and M. Schweiger, "Photon-measurement density functions. Part2: Finite-element-method calculations," Appl. Opt. **34**, 8026-8037 (1995).
25. A. Borsic, W. R. B. Lionheart, and C. N. McLeod, "Generation of anisotropic-smoothness regularization filters for EIT," IEEE Trans. Med. Imaging **21**, 579-587 (2002).
26. B. Brooksby, H. Dehghani, B. W. Pogue, and K. D. Paulsen, "Near infrared (NIR) tomography breast image reconstruction with a priori structural information from MRI: algorithm development for reconstructing heterogeneities," IEEE J. STQE **9**, 199-209 (2003).
27. K. D. Paulsen, Jiang, H., "Enhanced frequency-domain optical image reconstruction in tissues through total-variation minimization," Appl. Opt. **35**, 3447-3458 (1996).
28. K. D. Paulsen, P. Meaney, M. Moskowitz, and J. Sullican, Jr., "A dual mesh for finite element based reconstruction algorithms," IEEE Trans. Med. Imaging **14**, 504-514 (1995).
29. M. Schweiger, and S. R. Arridge, "Optical tomographic reconstruction in a complex head model using a priori boundary information," Phys. Med. Biol. **44**, 2703-2722 (1999).
30. B. Brooksby, B. W. Pogue, S. Jiang, H. Dehghani, S. Srinivasan, C. Kogel, T. D. Tosteson, J. Weaver, S. P. Poplack, and K. D. Paulsen, "Imaging breast adipose and fibroglandular tissue molecular signatures using hybrid MRI-guided near-infrared spectral tomography," Proc. Natl. Acad. Sci. USA **103**, 8828-8833 (2006).
31. S. Srinivasan, B. W. Pogue, S. Jiang, H. Dehghani, C. Kogel, S. Soho, J. J. Gibson, T. D. Tosteson, S. P. Poplack, and K. D. Paulsen, "In vivo hemoglobin and water concentrations, oxygen saturation, and scattering estimates from near-infrared breast tomography using spectral reconstruction," Acad. Radiol. **13**, 195-202 (2006).
32. T. O. McBride, B. W. Pogue, S. Jiang, U. L. Osterberg, K. D. Paulsen, and S. P. Poplack, "Initial studies of in vivo absorbing and scattering heterogeneity in near-infrared tomographic breast imaging," Opt. Lett. **26**, 822-824 (2001).

#78716 - $15.00 USD Received 4 January 2007; revised 22 February 2007; accepted 13 March 2007
(C) 2007 OSA

33. B. W. Pogue, McBride, T. O., Prewitt, J., Osterberg, U. L., Paulsen, K. D., "Spatially variant regularization improves diffuse optical tomography," Appl. Opt. **38**, 2950-2961 (1999).
34. S. Jiang, B. W. Pogue, T. O. McBride, and K. D. Paulsen, "Quantitative analysis of near-infrared tomography: sensitivity to the tissue-simulating precalibration phantom," J. Biomed. Opt. **8**, 308-315 (2003).
35. B. Pogue, and M. Patterson, "Review of tissue simulating phantoms for optical spectroscopy, imaging and dosimetry," J. Biomed. Opt. **11**, 0411021-04110216 (2006).

1. Introduction

Imaging the spatial distribution of fluorescence activity at depth in tissue is a challenging problem that has yet to impact clinical practice. The most popular approach is diffuse optical fluorescence tomography (DOFT), a model-based method which approximates photon propagation as a diffuse field and computationally matches model parameters to measured boundary data. The theoretical framework is well established [1-5] and feasibility studies have demonstrated fluorescence yield imaging in various phantom geometries [6-9]. Much of the most recent research has focused on high-throughput, full body imaging of small animals [10, 11] but no human images have been published to date. DOFT produces low resolution images compared to standard clinical modalities such as x-ray CT and MRI due to the highly scattered photon fields and relatively sparse measurement sampling of the tissue volume. The reconstruction problem is ill-posed and underdetermined and large heterogeneity in tissue optical properties caused by complex tissue morphology further challenges the imaging algorithm. Sensitivity drops with increasing depth resulting in a non-linear responsivity across the imaging field, making it more difficult to image larger tissue volumes. Experiments in larger volumes that more closely resemble a human breast typically consider unrealistically high fluorophore contrasts and simple geometries [9, 12]. Though these studies are important for advancing the understanding of the modality, improving image resolution and contrast sensitivity is critical for identifying a clinical role for DOFT.

DOFT is an extension of the more widely studied diffuse optical tomography (DOT) which suffers similarly from low resolution and depth-dependent contrast sensitivity in the absence of spatial or spectral prior information to guide the solution. However, methods to incorporate highly-resolved anatomical data obtained from standard clinical modalities have improved the quantification of the optically derived images [13-15]. These hybrid approaches lead to a conceptually new application of optical tomography, one in which the highly resolved imaging system provides a structural template upon which volumetric optical spectroscopic images are constructed. This framework may be applied to either absorption and scatter spectroscopy, or fluorescence spectroscopy. Additional challenges specific to the fluorescence case include lower signal intensity, excitation source contamination of the fluorescence emission measurements due to filter leakage, and tissue optical property effects on both the excitation and emission photon propagation. Applying spatial guidance techniques to the more complicated DOFT problem may yield even larger gains in imaging capability.

This paper introduces a method to dramatically improve fluorescence imaging at depth in tissue by coupling MRI and fluorescence tomography. Tissue structural information determined from standard T1 and T2 MR images is encoded as a spatial filter in the DOFT reconstruction algorithm and used to guide the recovery of fluorescence activity. In this implementation, reconstruction parameters are loosely grouped into regions based on tissue-type determined from the MR images but are permitted to update independently, giving rise to the term “soft” spatial priors [16]. The algorithm is tested with phantom data of Lutetium Texaphyrin, a near-infrared photosensitizer shown to accumulate preferential in a variety of malignancies [17-20], recorded from a newly developed MR-coupled spectroscopy-based fluorescence tomography system. A simulation study based on realistic geometries generated from MR images of a normal human breast serves as an initial illustration of expected improvements provided by the spatial priors approach in complex domains.

#78716 - $15.00 USD Received 4 January 2007; revised 22 February 2007; accepted 13 March 2007
(C) 2007 OSA

2. Theory

Assuming highly diffuse media, the transport of light at a given modulation frequency ω in the presence of fluorescence generated by an external source at the excitation wavelength (λ_x) of the fluorescing agent, is modeled by two diffusion equations, where the solution of the first equation provides the driving source term of the second [5]:

$$-\nabla\cdot\kappa_x(r)\nabla\Phi_x(r,\omega)+(\mu_{a_x}(r)+\frac{i\omega}{c(r)})\Phi_x(r,\omega)=q_0(r,\omega) \quad (1)$$

$$-\nabla\cdot\kappa_m(r)\nabla\Phi_m(r,\omega)+(\mu_{a_m}(r)+\frac{i\omega}{c(r)})\Phi_m(r,\omega)=\Phi_x(r,\omega)\eta\mu_{a_f}(r)\frac{1-i\omega\tau(r)}{1+[\omega\tau(r)]^2} \quad (2)$$

where subscripts *x* and *m* represent the excitation and emission fluence at wavelengths λ_x and λ_m, respectively. The intrinsic optical parameters $\mu_{a_{x,m}}$ and $\mu'_{s_{x,m}}$ are the absorption and reduced scattering coefficients respectively, $q_0(r,\omega)$ is an isotropic source and $\Phi_{x,m}(r,\omega)$ is the photon fluence rate at position ***r***. The diffusion coefficient is given by $\kappa_{x,m}=\frac{1}{3(\mu_{a_{x,m}}+\mu'_{s_{x,m}})}$ and *c(r)* is the speed of light in the medium at any point, defined by $c_o/n(r)$, where *n(r)* is the index of refraction at the same location and c_o is the speed of light in vacuum. The fluorescence parameters are the lifetime $\tau(r)$ and the fluorescence yield $\eta\mu_{a_f}(r)$, the latter a product of the fluorophore's quantum efficiency η and its absorption coefficient $\mu_{a_f}(r)$.

The most appropriate description of the air-tissue boundary is derived with an index-mismatched type III condition (also known as Robin or mixed), in which some fraction of the fluence at the external boundary of the tissue exits and does not return. The flux leaving the external boundary is equal to the fluence rate at the boundary weighted by a factor that accounts for the internal reflection of light back into the tissue. This relationship is described in the following equation:

$$\Phi_{x,m}(\xi,\omega)+2A\hat{\mathbf{n}}\cdot\kappa_{x,m}(\xi)\nabla\Phi_{x,m}(\xi,\omega)=0 \quad (3)$$

where ξ is a point on the external boundary, and *A* depends upon the relative refractive index (RI) mismatch between tissue Ω and air. *A* can be derived from Fresnel's law:

$$A=\frac{2/(1-R_0)-1+\left|\cos\theta_c\right|^3}{1-\left|\cos\theta_c\right|^2} \quad (4)$$

where $\theta_c=\arcsin(n_{AIR}/n_1)$, the angle at which total internal reflection occurs for photons moving from region Ω with RI n_1 to air with RI n_{AIR}, and $R_0=\frac{(n_1/n_{AIR}-1)^2}{(n_1/n_{AIR}+1)^2}$. At the external boundaries, $n_{AIR}=1$.

2.1 Finite element implementation:

When the refractive index is homogenous (assumed to be 1.33 [21]), the finite element discretization of a volume Ω can be obtained by subdividing the domain into D elements joined at V vertex nodes. In the finite element method (FEM), $\Phi_{x,m}(\mathbf{r})$ is approximated by

#78716 - $15.00 USD Received 4 January 2007; revised 22 February 2007; accepted 13 March 2007
(C) 2007 OSA

the piecewise continuous polynomial function $\Phi^h_{x,m}(r,w) = \sum_i^V \Phi_{x,m_i} u_i(r) \Omega^h$, where Ω^h is a finite dimensional subspace spanned by basis functions $\{u_i(r); i = 1 \ldots V\}$ chosen to have limited support. The problem of solving for $\Phi^h_{x,m}$ becomes one of sparse matrix inversion, and in this work, a bi-conjugate gradient stabilized solver is used. As developed previously [22, 23], the coupled diffusion Eqs. (1) and (2) in the FEM framework can be expressed as a system of linear algebraic equations:

$$\left(K_x(\kappa) + C_x(\mu_{a\,x} + \frac{i\omega}{c(r)}) + \frac{1}{2A} F_x \right) \Phi_x = Q_0 \tag{5}$$

$$\left(K_m(\kappa) + C_m(\mu_{a\,m} + \frac{i\omega}{c(r)}) + \frac{1}{2A} F_m \right) \Phi_m = -Q_m \tag{6}$$

where the matrices $K_{x,m}(\kappa)$, $C_{x,m}(\mu_a + \frac{i\omega}{c(r)})$, and $F_{x,m}$ have entries given by:

$$K_{x,m_{ij}} = \int_\Omega \kappa_{x,m}(r) \nabla u_i(r) . \nabla u_j(r) d^n r \tag{7}$$

$$C_{x,m_{ij}} = \int_\Omega (\mu_{a_{x,m}}(r) + \frac{i\omega}{c(r)}) u_i(r) u_j(r) d^n r \tag{8}$$

$$F_{x,m_{ij}} = \oint_{\partial\Omega} u_i(r) u_j(r) d^{n-1} r \tag{9}$$

and the source vector Q_0 has terms

$$Q_{0_i} = \int_\Omega u_i(r) q_0(r) d^n r \tag{10}$$

The source term is defined as a Gaussian distribution, matching the intensity profile at the tip of the optical fiber. Because the source is assumed spherically isotropic, modeling is more accurate when it is centered one scattering distance within the outer boundary. The source vector Q_m for fluorescence re-emission is expressed as

$$Q_{m_i} = \int_\Omega u_i(r) \left[\Phi_x(r,\omega) \eta \mu_{a_f}(r) \frac{1 - j\omega\tau(r)}{1 + [\omega\tau(r)]^2} \right] d^n r \tag{11}$$

and is distributed throughout the domain.

2.2 The inverse model

2.2.1 No spatial priors

In the inverse problem, the goal is the recovery of optical properties at each FEM node using surface measurements of light fluence at both the excitation and emission wavelength sequentially (assuming the use of two externally applied sources, one at each wavelength), followed by fluorescence yield reconstruction at the emission wavelength. The computational approach is to minimize the difference between measured fluence, $\Phi^{Meas}_{x,m}$, at the tissue surface and calculated data, $\Phi^C_{x,m}$, from the model Eqs. (1) and (2) by adjusting the spatial distribution of the unknown parameters through minimization of the 'objective' function. The objective function for recovering the optical properties at the excitation wavelength, $\mu_x = (\mu_{a_x}, \kappa_x)$, is given as

#78716 - $15.00 USD Received 4 January 2007; revised 22 February 2007; accepted 13 March 2007
(C) 2007 OSA

$$\chi^2 = \sum_{i=1}^{NM} \left(\Phi_{x_i}^{Meas} - \Phi_{x_i}^{C} \right)^2 + \lambda \sum_{j=1}^{NN} I \left(\mu_{x_j} - \mu_{x_0} \right)^2 \quad (12)$$

where *NM* is the total number of measurements given by the imaging system, *NN* is the number of parameters representing the optical property distribution which corresponds to the number of nodes in the reconstruction mesh, and *I* is an *NN* × *NN* identity matrix. In general, χ^2 will not equal zero, but the values of μ_x for which $\frac{\partial \chi^2}{\partial \mu_x}$ is close to zero can be determined, based on an initial estimate of μ_x. Following the Taylor series method for deriving Newton's method, $\frac{\partial \chi^2}{\partial \mu_x}$ is evaluated at μ_x based on an expansion around some nearby point μ_{x_0}, where the second and higher order terms are ignored, leading to the iterative update equation:

$$\Delta \mu_x = \left[J^T J + \lambda I \right]^{-1} J^T \left(\Phi_x^{Meas} - \Phi_x^{C} \right) \quad (13)$$

where J is the Jacobian matrix, here calculated using the Adjoint method [24]. Equation (13) is known as the Moore-Penrose generalized inverse and is found to be suitable for problems where the number of unknowns to be recovered is much larger than the amount of information (measurements) available. In standard practice, *I* is an identity matrix, and in this work λ is some fixed fraction multiplied by the maximum value on the diagonal of the Hessian matrix $J^T J$, and is therefore updated at each iteration. To recover the optical properties at the emission wavelength, $\mu_m = \left(\mu_{a_m}, \kappa_m \right)$, the externally applied illuminating source is changed to one at the emission wavelength and the formulation presented in Eq. (13) is used.

The recovered optical properties are used in the fluorescence yield reconstruction which also adheres to the minimization formulation presented in Eq. (12). The unknown parameter in Eq. (13) becomes $\eta \mu_{a_f}(r)$, and the Jacobian can be calculated by similar Adjoint properties described above and in Ref. [5].

2.2.2 Spatial priors

Spatial prior information is incorporated by assuming a 'generalized Tikhonov' penalty term which is similar in structure to Eq. (12) except that the identity matrix is replaced with a Laplacian-type matrix, presented here for the excitation field:

$$\chi^2 = \sum_{i=1}^{NM} \left(\Phi_{x_i}^{Meas} - \Phi_{x_i}^{C} \right)^2 + \beta \sum_{j=1}^{NN} \left(L(\mu_{x_j} - \mu_{x_0}) \right)^2 \quad (14)$$

where *NN* is the number of unknowns in the model [16, 25, 26]. The constant, β, balances the effect of the parameters with the model-data mismatch in the same manner as λ in Eq. (13). The dimensionless 'filter' matrix, *L*, is generated using MRI-derived priors and its construction is flexible. In this application, each node in the FEM mesh is labeled according to the region, or tissue type, with which it is associated (in the MR image). The L-matrix represents a Laplacian-type structure, the diagonal of which is $L_{i,i}$=1 where *i* is the nodal index. When nodes *i* and *j* are in the same region containing *n* nodes, $L_{i,j}$=-1/n, otherwise $L_{i,j}$=0. This effectively relaxes the smoothness constraints at the interface between different tissues, in directions normal to their common boundary. The effect on image quality is similar to that achieved through total variation minimization schemes [27] but easily encodes internal

#78716 - $15.00 USD Received 4 January 2007; revised 22 February 2007; accepted 13 March 2007
(C) 2007 OSA

boundary information from MR images. Following the same procedure as in the no-priors case, the parameter update is given by

$$\Delta\mu_x = \left[J^T J + \beta L^T L\right]^{-1} J^T \left(\Phi_x^{Meas} - \Phi_x^C\right) \tag{15}$$

where much like λ in Eq. (12), β is a fixed fraction multiplied by the maximum value on the diagonal of $J^T J$. This update formulation is also used to recover the optical properties at the emission wavelength as well as the fluorescence yield, as described in Section 2.2.1.

2.2.3 Reconstruction basis

A number of different strategies for defining the reconstruction basis are possible, including second mesh and pixel basis [28, 29]. The choice of reconstruction basis allows for computational efficiency which serves to reduce the number of unknowns in the algorithm. The problem at hand is twofold: The forward problem requires that the volume of interest is subdivided into adequate number of sub-domains which allow for an accurate description of the calculated fields, whereas a reduction in the number of unknowns improves the ill-posedness of the problem in the reconstruction algorithm. This is addressed by defining a separate reconstruction basis (different from the meshes used in the FEM implementation), upon which the unknowns are updated in Eqs. (13) and (15) [23]. In cases where no prior structural information is available, a pixel basis which defines a set of regularly spaced pixels for the update of the quantities of interest is used. However, when spatial priors are involved, it is crucial to ensure that enough pixels are used to adequately define small structural regions. In this case, a set of regular pixel bases are introduced in each region of interest, which account for the region's individual shape and size. A semi-adaptive method which allows the number of pixels in each region to be selected was used in the studies presented here. The same region-based pixel basis is used throughout the iterative reconstruction process.

3. Methods

3.1 Simulation studies

Test domains for simulation studies were derived from a T1 weighted MR image of a human breast which measured approximately 10.5 cm in diameter. A 2-D slice of the breast volume was discretized into a mesh of approximately 2000 nodes and MR image intensity thresholds were used to assign adipose and fibro-glandular tissue volumes into mesh regions. Figure 1 shows the original MR breast image and its associated discretized, region-labeled mesh. The MR image originated from a clinical exam with our MR coupled frequency domain NIR system and therefore reveals an irregularly shaped breast boundary caused by the fiber optic array slightly compressing the breast at the contact positions. A cancerous tumor region was added as a target anomaly or region of interest for these studies and is depicted in the figure. A second test case with a tumor region located near the center of the domain was used to explore the nonlinear sensitivity of diffuse optical tomographic techniques. The source-detector positions were determined directly from the MR image and represent 16 optical fibers circumscribing the breast domain in a single plane. Light is detected at all non-source fiber positions providing a total of 240 measurements of intensity and phase per wavelength. This simulated configuration matches our experimental fluorescence tomography system.

#78716 - $15.00 USD Received 4 January 2007; revised 22 February 2007; accepted 13 March 2007
(C) 2007 OSA

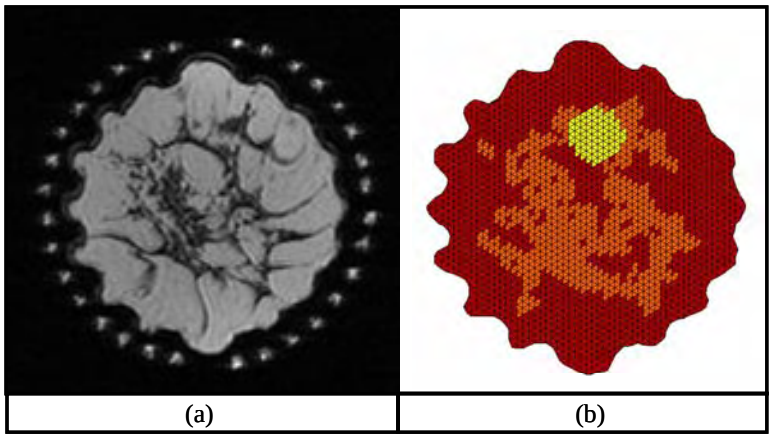

Fig. 1. An axial T1 weighted MR slice of a human breast is shown in (a), from which the test domain for simulation studies was derived. Darker regions indicate fibro-glandular tissue imbedded in adipose tissue indicated by lighter values. The image was acquired during a clinical exam with one of our MR-coupled NIR tomography systems and shows the indentations caused by the fiber optic probes. The test domain (b) was a discretization of the MR image thresholded into regions. The yellow anomaly was added to simulate a targeted cancerous tumor.

In this set of studies, regions were assigned values in terms of biologically relevant optical absorbing (HbO, dHb, Water, Lutetium Texaphyrin) as well as scattering parameters (Mie scattering amplitude and power). These values, provided in Table 1, represent typical known in vivo levels of endogenous chromophores and are consistent with previous clinical work [30, 31]. Though it is unknown exactly how Lutetium Texaphyrin (LuTex) will distribute in a human breast, the concentrations used are similar to those reported in ex vivo studies [17] and at least represent a reasonably complex distribution for demonstrating recovery of fluorescence yield. Tissue chromophore concentrations were used to calculate total optical absorption and scattering values at the excitation and emission wavelengths based on experimentally determined values of molar extinction coefficients. Simulated noisy data was generated based on these optical properties in the following manner: 1) frequency domain data for a light source at the excitation wavelength, 2) frequency domain data for a light source at the emission wavelength, and, 3) Continuous Wave (CW) fluorescence emission data at the emission wavelength. This represents a total of 3 data sets for a given imaging session: two frequency domain data sets for determining background optical properties and one CW fluorescence emission data set. CW fluorescence emission data was used to match the capabilities of our experimental system and results in a simplification of Eq. (2) which can be handled by setting $\omega = 0$.

Table 1. Chromophore concentrations and scattering parameter values assigned to the mesh regions in the simulation studies

	Oxy-hemoglobin (μM)	Deoxy-hemoglobin (μM)	Water (%)	Lutetium Texaphyrin (μM)	Scattering Amplitude	Scattering Power
Adipose	10	10	50	0.3	1.0	1.0
Fibro-glandular	15	15	60	0.5	1.1	1.1
Tumor	20	18	90	1.0	1.2	1.15

Given the modest Stoke's shift of LuTex, depicted in Fig. 2, the choice of excitation wavelength has practical implications for experimental work. The difficulty in filtering the excitation signal precludes the use of Lutex's NIR absorption peak (about 735 nm) to excite

#78716 - $15.00 USD Received 4 January 2007; revised 22 February 2007; accepted 13 March 2007
(C) 2007 OSA

the fluorophore. In this study, a 690 nm excitation wavelength was used for both simulated and experimental data acquisition. In addition to normally distributed random noise added to the frequency domain data (5% amplitude and 1 degree phase) and CW fluorescence emission (10% intensity), excitation signal leakage through the filter was added to the CW fluorescence emission intensity to simulate a typical 7 OD rejection of the excitation intensity. This number comes directly from experimentally measured rejection estimates for the filters in the tomography system used in the experiments performed here.

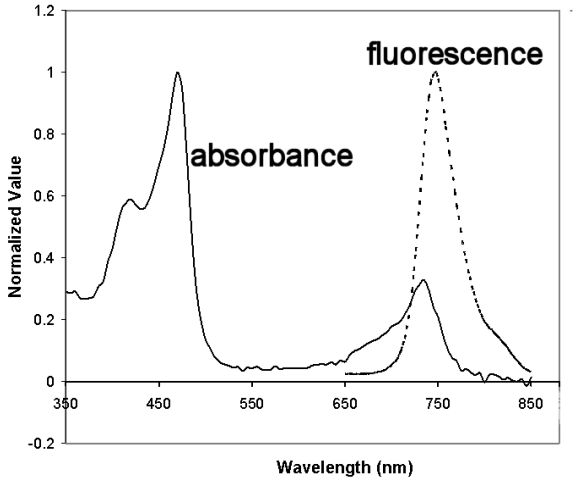

Fig. 2. The normalized absorbance and fluorescence emission spectra of Lutetium Texaphyrin are shown.

The general image reconstruction protocol was as follows:

1) Reconstruct for optical properties at the excitation wavelength, μ_{ax} and μ_{sx}', with frequency domain data,
2) Reconstruct for optical properties at the emission wavelength, μ_{am} and μ_{sm}', with frequency domain data collected using a laser source at the emission wavelength,
3) Use the reconstructed optical properties and fluorescence intensity data to recover fluorescence yield.

The same reconstruction algorithm was used to determine background optical properties in steps (1) and (2) and is based on previously reported work [32, 33]. Initial estimates for all parameters were generated using homogenous fitting algorithms which enforce a single value for all nodes. The Jacobian matrix was calculated on a fine mesh of approximately 2000 nodes and interpolated onto a course reconstruction pixel basis for inversion. A 30 by 30 pixel reconstruction basis was used for the no-priors case. The spatial priors reconstruction used a newly developed semi-adaptive pixel basis that redistributes the pixels based on the region information, as described in section 2.2.3. This method ensures that each region contains an adequate number of nodes to approximate the internal structure of the domain. Convergence was defined as less than a 2% change in projection error between successive iterations for the frequency domain optical properties algorithm and less than a 1% change in projection error between iterations for the fluorescence yield reconstruction. Similar algorithmic parameters were used for the phantom studies and are described in further detail below.

3.2 Phantom studies

A spectrometer based tomographic imaging system which couples directly into a Philips 3T MRI magnet was used to acquire fluorescence emission spectra. The system, depicted in Fig.

#78716 - $15.00 USD Received 4 January 2007; revised 22 February 2007; accepted 13 March 2007
(C) 2007 OSA

3, is composed of 16 spectrometers with low noise CCD cameras cooled to -70 C. Sixteen 13 meter long silica fiber bundles circumscribe the imaging domain in contact mode and couple into the spectrometers via custom designed input optics with a six position automated filter wheel. Fluorescence emission signals are processed with long pass interference filters before entering the spectrometer. Each fiber bundle contains eight 400 μm fibers, seven of which directly couple the tissue surface to the spectrometer input while the eighth couples the tissue surface to the light source. This detector configuration minimizes coupling losses and provides parallel detection of full spectra for each source position. Inter-fiber tissue coupling calibration factors were determined prior to imaging using a cylindrical homogenous phantom with a centrally located source/detector. The custom manufactured input optics were designed to optimize filtering and maximize the light detection efficiency of the spectrometers. Camera exposure times can be adjusted to the detected light level to maximize the signal to noise ratio. With 15 detectors per 16 source positions, a total of 240 measurements are recorded for a given acquisition.

Fig. 3. The experimental spectrometer-based system depicted at left couples directly into the MR via 13 meter fiber optic bundles. Sixteen spectrometers are computer controlled for rapid image acquisition (left photograph). An animal interface (right photograph) is composed of a rodent MR coil custom built by Philips Research Hamburg to accommodate the optical fiber array for simultaneous MR and NIR fluorescence imaging.

Lutetium Texaphyrin provided by Pharamcyclics was diluted in water and used as the imaging fluorophore. The test domain was a solid 5.5 cm diameter hardened epoxy phantom with scatterer and absorbers created by titanium dioxide powder and India ink, respectively [34, 35]. The phantom had a 14 mm hole located approximately 12 mm from the phantom center. The background optical properties were μ_{ax} = 0.005 and μ_{sx}' = 1.0 mm^{-1}, measured with a frequency domain system near the excitation wavelength. Unlike the simulation experiments, the optical properties were assumed constant throughout the domain in this experiment. These values were also used as the optical properties at the emission wavelength. The hole was filled with a solution of 1% Intralipid to match the scattering value of the background, and varying concentrations of Lutex (0.3125 μM to 5 μM) were added. This represents a simple test case for investigating the imaging response to varying concentrations of fluorophore. The excitation source was a 690 nm laser diode which matches the wavelength used in the simulation studies. Total acquisition time for the fluorescence emission was less than 4 minutes (total of 240 data points).

Even after processing the collected light with a 720 nm long pass interference filter (Omega Optics) which provides 7 OD rejection of the excitation light as well as the filtering offered by the spectrograph grating, emission spectra recorded by the detector are composed of a sum of the pure fluorescence signal and excitation bleed-through. In order to decouple these signals, previously recorded "basis spectra" of the bleed-through signal and the pure fluorescence signal are fit to the data. The process is illustrated in Fig. 4 for one measurement

#78716 - $15.00 USD Received 4 January 2007; revised 22 February 2007; accepted 13 March 2007
(C) 2007 OSA

at a single detector. A linear least squares algorithm operating on the basis spectra quantifies the amount of excitation bleed-through and true fluorescence signal that exists in each spectral recording, further reducing the effect of excitation bleed-through. This is accomplished by minimizing the summation

$$S = \sum_{i=1}^{N} \left[y_i - \left(aF(\lambda_i) + bG(\lambda_i) \right) \right]^2 \tag{16}$$

with respect to a and b, where y_i is the measured intensity at a given wavelength pixel, F and G are the excitation and fluorescence basis spectra, a and b are the coefficients recovered in the minimization procedure, and N is the number of wavelength pixels per spectrum. Once fit, the fluorescence signal is integrated and becomes the fluorescence emission intensity data for the reconstruction algorithm.

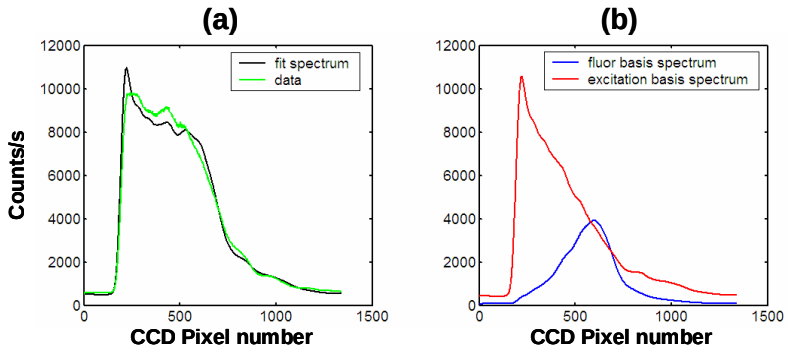

Fig. 4. An example of a pair of basis spectra for the excitation and fluorescence light (in counts/s as a function of CCD pixel number) is shown in (b). These spectra are recorded for each detector prior to imaging. In practice, the basis spectra are used to perform a least squares fit (a) to the spectrum measured for each source-detector pair to determine the relative contribution of the fluorescence and excitation light to the measured response.

To investigate the improved imaging capability of reconstructing data with spatial priors, each data set was reconstructed with and without spatial "soft" priors. Since the domain was easily characterized geometrically, spatial prior information was determined by direct manual measurement of the phantom. This information was encoded in the fine mesh used for reconstruction. Since background optical properties were previously determined with our frequency domain system, they were assumed known for image reconstruction. Convergence was defined as less than a 1 % change in projection error between iterations. All images were reconstructed using a 2GHz Centrino Duo laptop with 2GB RAM running Windows XP.

4. Results

4.1 Simulation results

Figures 5 and 6 display the target values of the two test cases along with images reconstructed using no priors and spatial soft prior information. Qualitatively, image recovery using spatial priors produces significantly more accurate images. Spatial priors preserve the general internal structure of the Lutex distribution, detail that is lost almost entirely in the no-priors case. Images of fluorescence yield show the most dramatic difference between the spatial priors and no priors reconstructions. Without spatial priors, the algorithm appears to have no ability to recover "cancer" regions of elevated fluorescence yield for these complicated cases. However, incorporating spatial priors results in images that qualitatively appear accurate and quantitatively are reasonably close to the true values. Figure 7 provides 1-D cross-sections near the y-axis of each domain. These plots confirm an inability of the no-priors imaging algorithm to recover the simulated fluorescent tumor in either test field. Alternatively, the

#78716 - $15.00 USD Received 4 January 2007; revised 22 February 2007; accepted 13 March 2007
(C) 2007 OSA

spatial prior-based imaging algorithm not only picks out the objects of interest, but provides fairly accurate reproductions of the complicated structure of simulated fibro-glandular layers. Mean values for the simulated cancer region near the domain center are 79% and 51% of the true values for the spatial priors and no-priors reconstructions, respectively. These numbers change to 75% and 45% for the case with the cancer region closer to the edge of the domain. They represent a significant improvement in imaging performance; however, they alone do not illustrate the full impact of incorporating spatial priors. The cross-sectional plots indicate that the no-priors images contain virtually no spatial discrimination of the cancer regions. Regional contrasts are depicted in Table 2 and further illustrate a dramatic overall improvement in cancer region quantification with spatial priors.

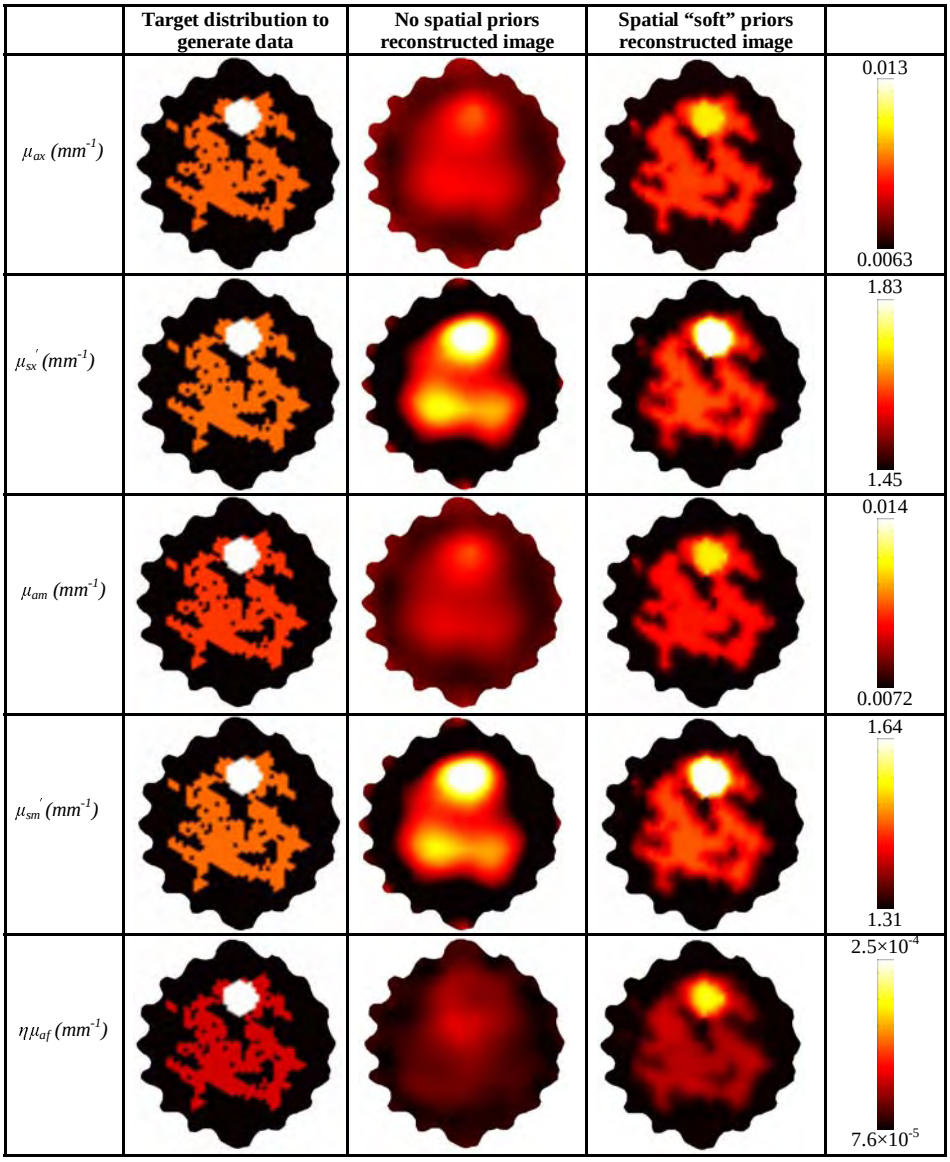

Fig. 5. Target and recovered values of $\mu_{a,x}$, $\mu'_{s,x}$, $\mu_{a,m}$, $\mu'_{s,m}$, and fluorescence yield, $\eta\mu_{af}$, for reconstruction implementations using no prior information and with spatial prior information. In this case, the simulated cancer region is near the edge, which is known to be easier to recover without spatial priors. The image scales are at right.

#78716 - $15.00 USD Received 4 January 2007; revised 22 February 2007; accepted 13 March 2007
(C) 2007 OSA

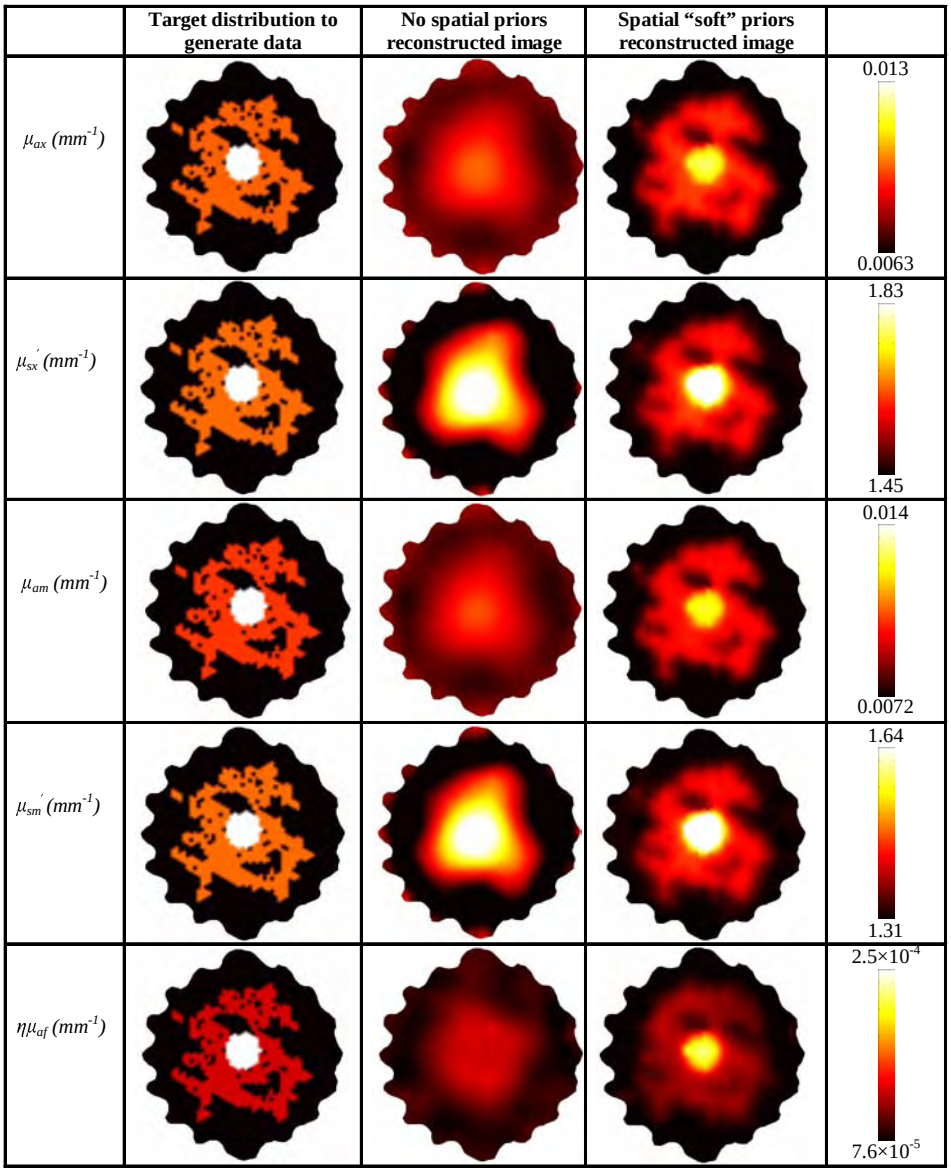

Fig. 6. Target and recovered values of $\mu_{a,x}$, $\mu'_{s,x}$, $\mu_{a,m}$, $\mu'_{s,m}$, and fluorescence yield, $\eta\mu_{af}$, for reconstruction implementations using no priors and spatial priors. In this case, the simulated tumor region is near the center of the imaging domain, which is known to be more difficult to recover accurately. Image scales are at right.

#78716 - $15.00 USD Received 4 January 2007; revised 22 February 2007; accepted 13 March 2007
(C) 2007 OSA

Table 2. Target and recovered fluorescence yield regional contrasts for the images in Figs. 4 and 5.

Shallow tumor	Target Contrast	No spatial priors	Spatial "soft" priors
Tumor : fibro-glandular	2.0 : 1	1.1 : 1	1.6 : 1
Tumor : adipose	3.3 : 1	1.3 : 1	2.3 : 1

Deep tumor	Target Contrast	No spatial priors	Spatial "soft" priors
Tumor : fibro-glandular	2.0 : 1	1.2 : 1	1.8 : 1
Tumor : adipose	3.3 : 1	1.4 : 1	2.4 : 1

Reported ratios were calculated using the mean values in each region.

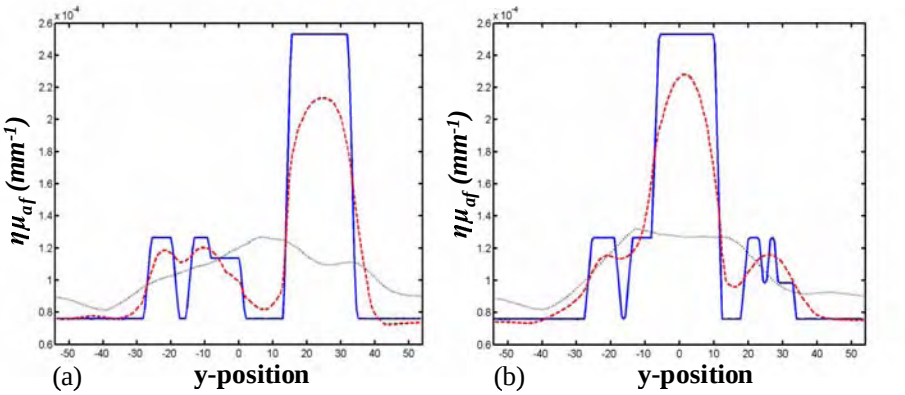

Fig. 7. Cross sectional plots of fluorescence yield are shown for the simulated imaging domains in (a) the case with an object near the edge and (b) the case with an object near the center. In both cases, the cross section is in the y-direction just off center from x = 0. The solid line represents the target value, the small dotted line the recovered value using a no-priors based algorithm, and the dashed line the recovered value using spatially guided reconstruction.

In addition to improved qualitative and quantitative accuracy, the spatial prior algorithm reduced the reconstruction time significantly. The full reconstruction time for the no-priors case, including background optical property estimation, was just under 9 minutes for both the central and superficial tumor cases. These times were reduced to less than 3 minutes and 90 seconds using spatial priors. In both cases, structural information guided the algorithm to a convergent solution in far fewer iterations than the no-priors cases.

4.2 Phantom results

Figure 8 shows fluorescence yield images recovered from phantom data using both no-prior and spatial prior image reconstruction approaches. A qualitative assessment of the images reveals a dramatic benefit of the spatial prior on image formation. The fluorescent object's borders are more clearly defined for all concentrations of Lutex when using spatial priors. Furthermore, the values of fluorescence yield throughout the region of interest are more homogeneous, and therefore, more similar to the actual distribution for spatially guided reconstructions. Incorporating spatial priors also suppresses edge artifacts significantly. This is most apparent in images of phantoms with low Lutex concentration. Figure 9 shows a full scale image of the 0.3125 μM phantom. Artifacts near the boundary virtually dominate the no-priors image and represent the largest fluorescent yield values in that imaging domain. None of these artifacts exist in the spatially guided image generated from the same fluorescence emission data. The spatially guided image also includes an easily discernable

#78716 - $15.00 USD Received 4 January 2007; revised 22 February 2007; accepted 13 March 2007
(C) 2007 OSA

fluorescent object at the correct location which is difficult to define in the no-priors case. These results indicate that for low fluorophore concentrations in this imaging domain, the correct fluorescent object would be identified only if prior structural information were incorporated in the reconstruction.

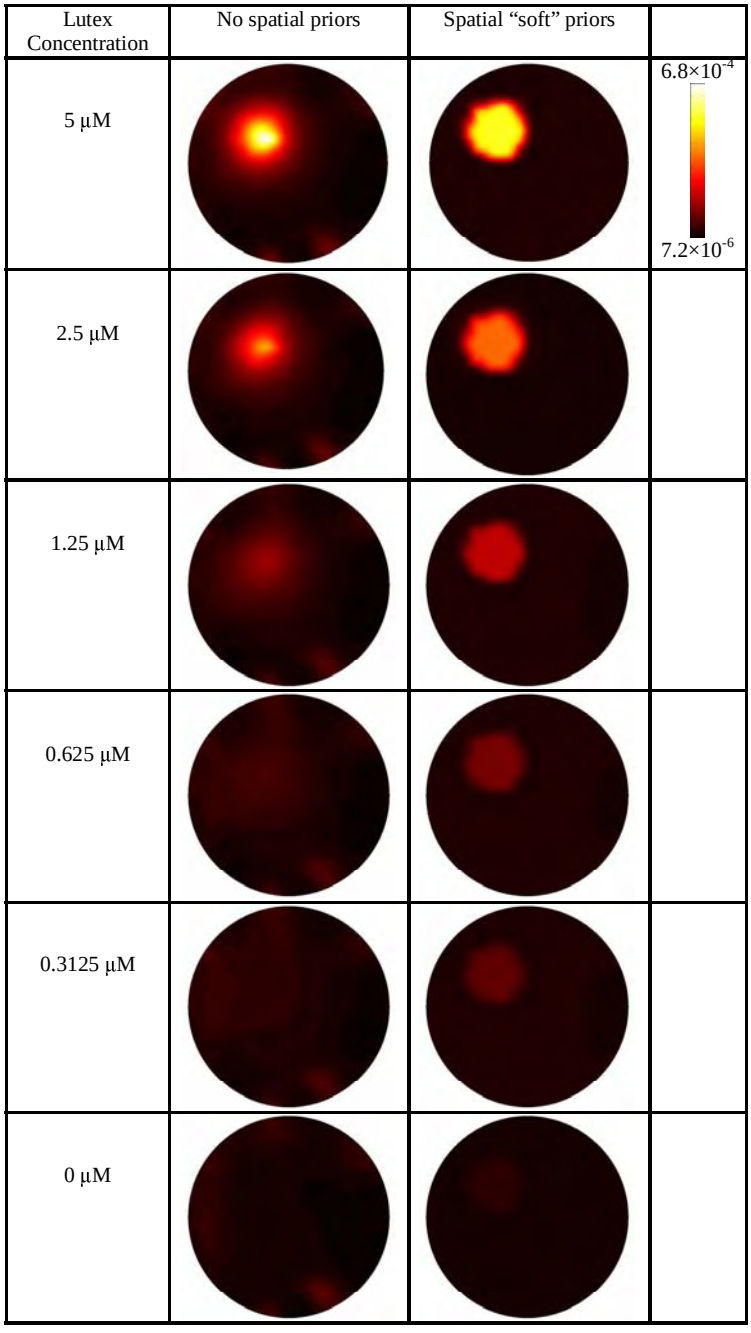

Fig. 8. Recovered images of fluorescence yield are shown for varying concentrations of Lutex. The 14 mm diameter fluorescent inclusion was embedded in a 55 mm diameter solid epoxy tissue simulating phantom. Images were generated from the same data using algorithms based on no-priors and spatial soft prior implementations.

#78716 - $15.00 USD Received 4 January 2007; revised 22 February 2007; accepted 13 March 2007
(C) 2007 OSA

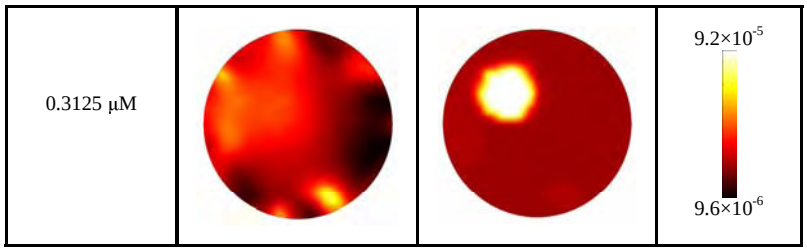

Fig. 9. A narrower colorbar-scale version of the 0.3125 μM Lutex phantom images shown in Fig. 8 further illustrates the improvement in image accuracy for the spatially guided algorithm.

Both techniques suffer from a bias in the recovered fluorescence yield which results in a positive value in the region of interest for the case with no fluorophore. This is most likely caused by bleed-through of the excitation light in the emission measurements coupled with an imperfect spectral fitting technique which results in positive values for fluorescence emission intensity even in phantoms containing no Lutex fluorophore. Incorporating additional filtering, such as band-pass source filtering, and optimizing the spectral fitting routine should address the bias signal and decrease the potential for incorrect quantification.

In addition to improving image quality and fluorescence yield quantification, spatial prior-based reconstructions converged in substantially less time than the no-priors algorithms. Reconstruction times ranged from 50 – 90 seconds when not using spatial priors and approximately 22 seconds for spatially guided reconstructions, marking an improvement of just over 75% in some cases. These numbers represent only the fluorescence yield reconstructions and not the recovery of background optical properties since μ_a and μ_s' were assumed known from prior measurements. In cases requiring the recovery of background optical properties, the improvement in reconstruction time will be similar to that previously quoted in the simulation results.

5. Discussion

This study introduced an effective method to incorporate MR-derived tissue morphology for imaging fluorescence yield at depth in tissue. The conceptual assertion is that diffuse tomography will be more successful as an imaging modality when combined with pre-existing imaging systems which have higher spatial resolution, such as MRI. Simulation and phantom studies were used here to validate the method prior to implementation as a full scale system. Using Lutex phantom data, the soft spatial prior implementation improved qualitative and quantitative imaging response of fluorescence yield. Prior information also suppressed image artifacts and more accurately represented the internal distribution of fluorophore. In the no-priors case, edge artifacts dominate the image for lower concentrations of fluorophore, and provide a misleading interpretation of the internal distribution of the fluorescent agent. The phantom studies represented simple distributions of optical properties and fluorophore concentration and improvements in image quality were still substantial. It is expected that soft prior implementations will benefit imaging performance to an even greater extent in complex tissue domains, an assertion born out in the simulation studies.

A simulated breast mesh derived directly from an MR image of a human breast served as the test bed for a complex tissue domain. The simulations demonstrated no ability to recover the internal distribution of the complicated domain without the use of spatially guided reconstructions. Qualitatively, fluorescence yield images generated without spatial priors had little resemblance to the target domain and completely disregarded the 18mm simulated cancer region, as evidenced by 1-D cross-sectional plots of fluorescence yield. Breakdown of the images in the no-priors case is likely due to poorly recovered background optical properties as well as the complexity of the fluorescence yield distribution itself. Certainly,

#78716 - $15.00 USD Received 4 January 2007; revised 22 February 2007; accepted 13 March 2007
(C) 2007 OSA

part of the improvement in fluorescence yield image accuracy can be attributed to improved images of background optical properties.

In these studies, it was assumed that the fluorophore distribution correlates directly to the fatty, fibro-glandular, and tumor tissue layers, which themselves exhibit no significant intra-region heterogeneity, in a given imaging domain. While this assumption appears reasonable based upon the biology of the tissue for endogenous chromophores [30, 31], further studies of the uptake of Lutex in-vivo are required to determine a correlation between tissue type and fluorophore localization. Should this assumption prove to be unrealistic, the "soft" spatial prior approach offers some latitude in terms of correctly identifying structural prior information. The algorithmic implementation groups tissue regions together in a region-specific regularization and allows individual nodes in those regions to update independently. As opposed to "hard" prior approaches where nodal values in a given region are assumed homogenous, a soft prior technique may recover positive fluorescent objects not directly encoded in the spatial prior information. This is a subject of further investigation.

The experimental system introduced here couples directly into a Philips 3T MRI to provide simultaneous MR and NIR fluorescence imaging. Simultaneous imaging simplifies co-registration of the MR image with the NIR reconstruction domains and reduces overall acquisition time. Optimization of this system for in vivo imaging is underway for both small animal and human breast imaging.

6. Conclusion

A spatially guided image reconstruction implementation based on prior knowledge of tissue morphology was shown to provide significant improvements in fluorescence yield recovery in complicated tissue volumes and to be highly beneficial for simple domains. Specifically, both phantom and simulation results demonstrated dramatic improvements in recovery and quantification of features in the fluorescence distribution. Structural guidance also reduced image reconstruction time substantially. A newly developed experimental system couples full-volume deep-tissue fluorescence spectroscopy capabilities directly into the MR bore for simultaneous MR-NIR fluorescence image acquisition. The results presented here show promise for this approach in all cases and tissue volumes considered. Extensions of this study are underway to determine the effect of incorrectly identifying the structural prior, especially in cases where the MR images produce false negative or false positive readings. A full characterization of the imaging limits of the experimental system will further complement the results presented here. It is clear that incorporating anatomical features derived from MR images in DOFT image reconstruction will improve sensitivity to lower concentrations of fluorophore, qualitative accuracy, and fluorescence yield quantification in-vivo.

Acknowledgments

This work was funded by the National Institutes of Health grants RO1 CA109558, RO1 CA69544, U54 CA105480, as well as Department of Defense Breast Cancer pre-doctoral fellowship BC051058.

#78716 - $15.00 USD Received 4 January 2007; revised 22 February 2007; accepted 13 March 2007
(C) 2007 OSA

Magnetic resonance–coupled fluorescence tomography scanner for molecular imaging of tissue

Scott C. Davis,[1,a)] Brian W. Pogue,[1,b)] Roger Springett,[2] Christoph Leussler,[3] Peter Mazurkewitz,[1] Stephen B. Tuttle,[1] Summer L. Gibbs-Strauss,[1] Shudong S. Jiang,[1] Hamid Dehghani,[1,4] and Keith D. Paulsen[1]
[1]*Thayer School of Engineering, Dartmouth College, Hanover, New Hampshire 03755, USA*
[2]*Dartmouth Medical School, Dartmouth College, Hanover, New Hampshire 03755, USA*
[3]*Philips Research Europe, Sector Medical Imaging Systems, Hamburg 22335, Germany*
[4]*School of Physics, University of Exeter, Exeter EX4 4QL, United Kingdom*

(Received 19 November 2007; accepted 13 April 2008; published online 6 June 2008)

A multichannel spectrally resolved optical tomography system to image molecular targets in small animals from within a clinical MRI is described. Long source/detector fibers operate in contact mode and couple light from the tissue surface in the magnet bore to 16 spectrometers, each containing two optical gratings optimized for the near infrared wavelength range. High sensitivity, cooled charge coupled devices connected to each spectrograph provide detection of the spectrally resolved signal, with exposure times that are automated for acquisition at each fiber. The design allows spectral fitting of the remission light, thereby separating the fluorescence signal from the nonspecific background, which improves the accuracy and sensitivity when imaging low fluorophore concentrations. Images of fluorescence yield are recovered using a nonlinear reconstruction approach based on the diffusion approximation of photon propagation in tissue. The tissue morphology derived from the MR images serves as an imaging template to guide the optical reconstruction algorithm. Sensitivity studies show that recovered values of indocyanine green fluorescence yield are linear to concentrations of 1 nM in a 70 mm diameter homogeneous phantom, and detection is feasible to near 10 pM. Phantom data also demonstrate imaging capabilities of imperfect fluorophore uptake in tissue volumes of clinically relevant sizes. A unique rodent MR coil provides optical fiber access for simultaneous optical and MR data acquisition of small animals. A pilot murine study using an orthotopic glioma tumor model demonstrates optical-MRI imaging of an epidermal growth factor receptor targeted fluorescent probe *in vivo*. © *2008 American Institute of Physics.* [DOI: 10.1063/1.2919131]

I. INTRODUCTION

Imaging fluorescent molecular targets to characterize tissue pathology *in vivo* is an important objective with broad implications for drug development in small animals and clinical diagnosis. Given the availability of targeted molecular imaging agents for animal research, several small animal fluorescence tomography scanners have been developed to provide volumetric images of fluorescence activity.[1–6] Other studies have focused on the systematic development and assessment of diffuse optical fluorescence tomographic (DOFT) imaging techniques in tissue volumes relevant to human imaging, if targeted probes earn clinical approval.[7–11] Most previous work involving human breast imaging has been completed using tissue simulating phantoms, though fluorescence tomography images of human breast using the nontargeted fluorophore indocyanine green (ICG) have very recently been published.[7]

Pursuing noninvasive optical molecular imaging at depth implies that the interrogating photons are measured only at the tissue surface, making the image inversion problem severely underdetermined and ill posed, even with dense source and detector configurations. The highly scattered photon field limits the resolution of diffuse optical tomographic (DOT) images and quantitative interpretation can be difficult. However, researchers have found that using tomographic data acquired at discrete near infrared (NIR) wavelengths and incorporating the spectral features of dominant tissue chromophores in the imaging algorithm improves imaging performance.[12–18] In general, greater quantitative accuracy is expected as the number of wavelengths increases; however, image resolution is still relatively poor compared to many clinical imaging systems. Additional information may be used to guide image recovery by noting that variation in tissue optical properties can be loosely associated with the tissue's anatomical structure, providing an opportunity to incorporate anatomical information from highly resolved conventional imaging systems in the recovery of images of optically relevant molecules. In practice, standard magnetic resonance (MR) images have been used to guide diffusion-based image reconstruction of endogenous tissue chromophores[19–21] and recently of fluorescent molecules.[8] An imaging system that combines fully resolved spectra of transmitted or emitted light and simultaneously acquired

[a)]Electronic mail: scott.c.davis@dartmouth.edu.
[b)]Electronic mail: brian.w.pogue@dartmouth.edu.

 © 2008 American Institute of Physics

Downloaded 16 Jul 2008 to 129.170.203.126. Redistribution subject to AIP license or copyright; see http://rsi.aip.org/rsi/copyright.jsp

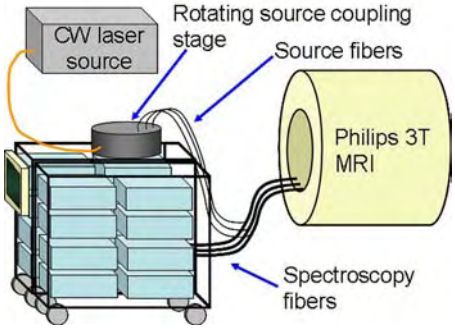

FIG. 1. (Color online) Diagram of the MRI-coupled 16 channel spectroscopy system for fluorescence tomography. Long, bifurcated spectroscopy fibers couple contact mode source-detection directly into the MR bore (3 of 16 fiber bundles are depicted).

MRI data can provide a particularly rich data set for a variety of imaging applications. A design goal of the system presented here was the development of a multiwavelength capable detection system with a large spectral bandwidth, providing a platform to explore the limits of broadband spectroscopic tomography inside MRI scanners.

This work describes a unique multichannel spectrometer-based detection system for imaging fluorescence yield in small animals and breast-sized domains. The system operates in continuous wave (cw) mode, so fully quantitative imaging of tissues requires the use of frequency domain measurements obtained with a separate detector system. The broadband cw detection system facilitates the use of unique spectral fitting preprocessing techniques to decouple the fluorescence emission from background contamination. The spectroscopic detection system directly couples into a Philips 3T magnet for simultaneous MRI and optical data acquisition. In this configuration, the highly resolved MR images are used as templates for imaging fluorescence yield from emission measurements of an injected fluorophore. A custom designed and manufactured rodent coil produced by Philips Research, Hamburg integrates the fiber optic array into a small-diameter radio frequency (rf) pickup coil for imaging small animals a 3T MRI.

II. SYSTEM DESIGN

The parallel spectrometer-based tomographic imaging system, depicted in Fig. 1, couples into a Philips 3T MRI magnet and was developed to be flexible enough to acquire transmission and emission spectra in the NIR. Major system components described below include the spectrograph, detection array, fiber optic transmission of light to and from the tissue surface, the acquisition light source, and MRI coils which incorporate the fiber optic patient or rodent interfaces. Photographs of the system are presented in Fig. 2.

A. Optical detection system

The optical detection system is composed of 16 Princeton/Acton Insight:400F Integrated Spectroscopy Systems (Acton, MA) residing in two custom designed wheeled carts (8020, Columbia City, IN). The Insight 400F consists of a 0.3 m F3.9 imaging spectrograph and a low noise, front illuminated charge coupled device (CCD) (Pixis 400F)

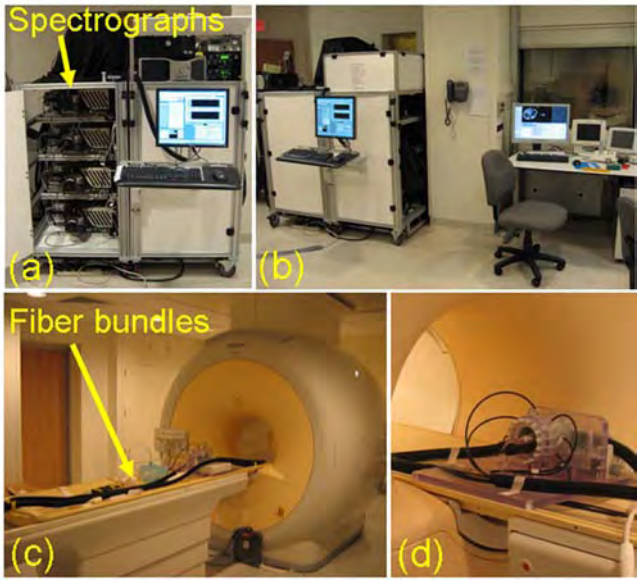

FIG. 2. (Color online) The spectroscopy system (a) is built into two carts which can be wheeled into the MRI control room shown in (b). Four of the insight spectrographs can be seen in the cart on the left in (a). Thirteen meter long fiber bundles extend through ports in the wall directly into the MRI bore (c). The small animal coil is shown in (d) with eight fiber bundles circumscribing a murine subject.

cooled to −70 °C. The 1340×400 pixel CCD is vertically binned to maximize detector area/wavelength providing a binned pixel area of 0.16 mm^2. Manufacturer specifications indicate a dark current of 0.0025 electrons/pixel s and quantum efficiencies of 0.45 at 750 nm and 0.20 at 950 nm. Each spectrograph contains a motorized grating turret holding 300 and 1200 l/mm gratings, which when coupled to the CCD, provide spectral ranges of 60 and 300 nm for a single grating position, respectively. Both gratings are blazed at 750 nm for maximum efficiency in the NIR.

The current system is designed for cw imaging only, as the CCD spectrometer detectors cannot measure rapid signals in the hundreds of megahertz frequency range. Thus, truly quantitative imaging requires acquiring data with both a frequency domain (FD) system and the CCD-based spectroscopy system. This procedure is demonstrated here, and the future hardware integration of the two is outlined in the Discussion.

B. Light collection and delivery

Sixteen custom designed bifurcated fiber bundles (Zlight, Latvia) channel light to and from the imaging domain. Each fiber bundle is composed of eight 13 m long and 400 μm diameter silica fibers which contact the tissue surface. Seven fibers from each bundle connect to the input system of each of the spectrographs, while the eighth, known as a source fiber, branches off to the source coupling system. Since the detection branch of each fiber bundle is fixed to a given spectrograph, the detected light path experiences no fiber-to-fiber coupling between the tissue surface and spectrometer, minimizing losses and providing fully parallel acquisition. Details of the light paths through the spectrograph system are presented elsewhere.[22] The light source is sequen-

Downloaded 16 Jul 2008 to 129.170.203.126. Redistribution subject to AIP license or copyright; see http://rsi.aip.org/rsi/copyright.jsp

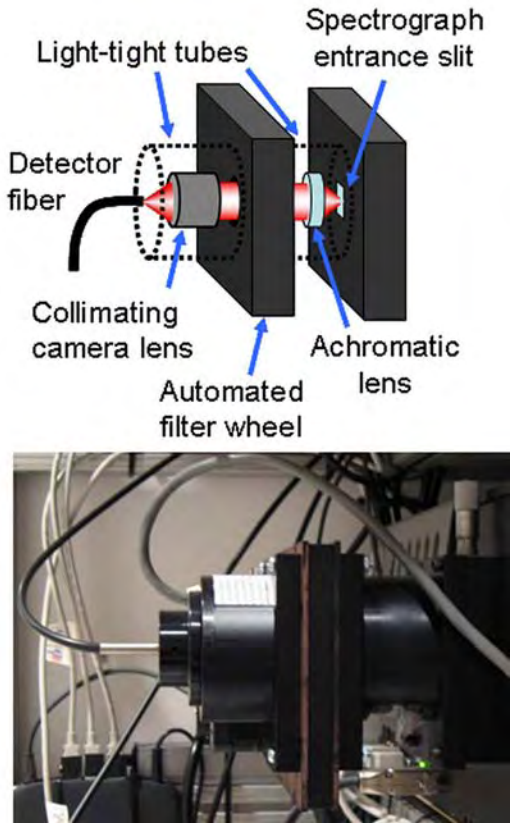

FIG. 3. (Color online) Diagram (top) and photograph (bottom) of the custom designed entrance optics. Lenses collimate the incoming light for filtering with selectable interference or ND filters and focus the light onto the spectrometer.

tially coupled into one of the 16 source fibers using a precision rotating stage (Velmex, Bloomfield, NY). The detector associated with the active source fiber is deactivated, resulting in 15 full-spectrum measurements acquired in parallel for each of the 16 source positions, though the number of source-detector pairs may be reduced for smaller domains.

The seven fibers in the detection branch of each fiber bundle are arranged in a line. These bundles couple to the spectrographs via custom designed input optics mounted on each spectrograph, as depicted in Fig. 3. An F1.4, 25 mm focal length digital camera lens (MegaPixel, Edmund Optics, Barrington, NJ) collects and collimates almost the full cone of light emitted from the detector fibers [numerical aperture (NA)=0.37]. The collimated light passes through a fully automated six-position filter wheel containing two long pass interference filters with 650 and 720 nm cut-ons (Omega, Brattleboro, VT) for fluorescence emission acquisition. Additionally, two neutral density (ND) filters with optical densities (ODs) of 1 and 2 reside in each filter wheel to increase the dynamic range of transmission imaging. Filter wheel positions are automatically adjusted during image acquisition depending on the type of acquisition. A 25 mm diameter, 60 mm focal length NIR achromat (Thorlabs, Newton, NJ) focuses the collimated and filtered light onto the input slit. The F# matching of fiber to spectrograph utilizes the high NA of the fibers to minimize the number of fibers in the bundle. The spectrograph entrance slits are fully opened to maximize photon collection, and the magnified image of the fiber array at the slit plane defines an effective slit width of just over 1 mm. Thus, the system operates at resolutions of about 2.2 and 11.2 nm using the 1200 and 300 l/mm gratings, respectively. The spectral resolution can be increased at the cost of throughput by reducing the input slit width.

Usable dynamic range of the 16 bit CCD chip is over 2.8 orders of magnitude assuming a minimum signal of 100 counts above background. Controlling the camera exposure times between 0.01 and 120 s adds an additional 4 orders of magnitude for a total dynamic range approaching 7 orders of magnitude. This range applies to fluorescence emission measurements which are prefiltered using long pass filters in the single-wheel automated filter selector described above. Since transmission mode measurements are not prefiltering with long pass filters, the ND filters may be used selectively to further enhance the detection performance, resulting in a total effective dynamic range of 9 orders of magnitude. Maximum camera exposure times are limited by the desired total acquisition time and may be increased to further extend the dynamic range in cases for which total acquisition time is not limited.

C. Light sources

The imaging method for a given acquisition determines which light source to incorporate into the imaging sequence. Currently available sources in use include a high power tungsten white light source for broadband transmission measurements and a bank of laser diodes. Since the focus of the work presented here is fluorescence imaging, data for the presented examples were acquired using a 690 nm cw laser diode (Applied Optronics, South Plainfield, NJ) to excite the fluorophore.

D. Patient/animal interface

A unique MRI rodent coil designed in collaboration with Philips Research Europe (Hamburg, Germany) features 16 access holes and nylon set screws to accommodate the spectroscopy fibers in a circular array. While small magnet bore animal systems are restricted to birdcage coil configurations, larger bore commercial clinical MR scanners allow the use of solenoid coil designs. The B_1-field direction of this coil must be oriented orthogonal to the main B_0 field axis. For small animal imaging at 3T, the solenoid coil provides high B_1 sensitivity and good field of view coverage. Calculations of electromagnetic field and coil characteristics were performed from simulations using a commercially available EM program (FEKO), which is based on the method of moments (Fig. 4).

The solenoid coil has an open inner diameter of 70 mm and is built from 8 mm wide strip conductors wound around a fiber glass cylinder. The coil support cylinder is made of glass fiber and is mechanically fixed to a sidewall. The parallel windings are connected as shown in Fig. 5 and the gap between individual strip conductors is 8 mm, providing ample space to accommodate the spectroscopy fibers. Circumscribing the fiber glass coil support cylinder is a removable polycarbonate cylinder containing nylon set screws to affix the spectroscopy fibers.

Downloaded 16 Jul 2008 to 129.170.203.126. Redistribution subject to AIP license or copyright; see http://rsi.aip.org/rsi/copyright.jsp

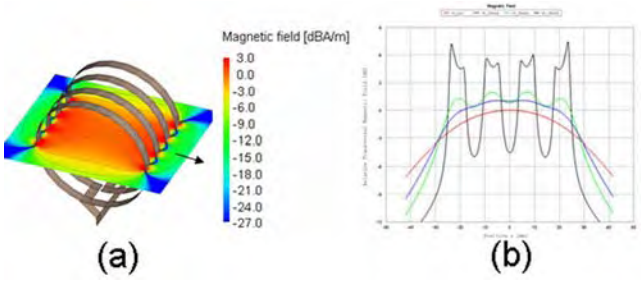

FIG. 4. (Color online) (a) Relative transversal magnetic field of the solenoid coil. The isocenter is set to 0 dB and the arrow shows the B_0 direction. (b) Sensitivity profiles along the coil axis (perpendicular to the main field B_0) for different distances from the isocenter.

The overall inductance of the solenoid is $L_s=1024$ μH at 127 MHz. Sixteen equidistant splits with nonmagnetic capacitors (ATC 100B) are introduced along the conductor to avoid current inhomogeneities (propagation effects). During the transmit phase, the coil is detuned by three independent parallel detuning circuits distributed along the solenoid, which make the coil transparent for the B1 transmit field. Optimized blocking radio frequency chokes prevent rf leakage and provide a high Q factor measured at $Q_L=600$ for the unloaded coil. A low noise preamplifier is directly connected to the solenoid, and optimal noise matching is performed via a low loss pi network.

For mouse brain imaging, a custom designed molded mouse bed is used, also shown in Fig. 5. The bed contains fiber optic access holes to provide stable positioning of eight spectroscopy fibers around the mouse head, reducing the optical data set to a maximum of 56 source-detector pairs.

Larger volumes and patient breast imaging capabilities are provided by a fiber optic ring attached to a commercial 3T MRI breast coil (MRI Devices, Waukesha, WI), depicted in Fig. 6. The current design requires manual fiber positioning using set screws, however, spiral ring and parallel plate geometries may be implemented for more reliable positioning.

E. Automated acquisition

The system is operated using a Dell desktop personal computer running Windows XP Professional. Image acquisition is automated using custom programs written in LABVIEW (National Instruments, Austin, TX) developed with the SI-

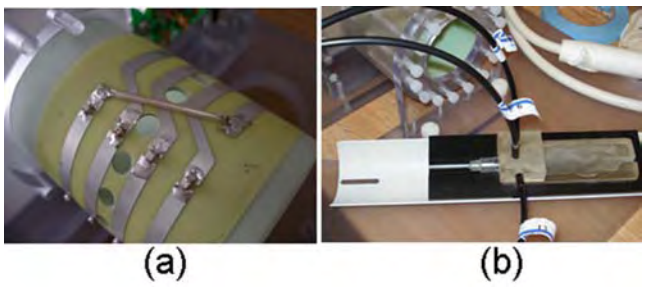

FIG. 5. (Color online) (a) Photograph of the coil layout showing connected strip conductors and holes to provide access for optical fibers. The custom designed mouse bed accommodates the spectroscopy fiber bundles and fits into the rodent coil for simultaneous MR and optical acquisition (b).

FIG. 6. (Color online) The patient interface is a circular array of fibers that couples into a standard MR breast coil (a) although parallel plate geometries are also under consideration (b).

Toolkit camera/spectrometer drivers produced by Rcubed, LLC (Lawrenceville, New Jersey). USB cables connect all camera/spectrometer/filter wheel units to the computer, and the motorized source-coupling stage is connected via a serial cable. A screenshot of the primary acquisition control program is provided in Fig. 7. The user interface is designed to minimize technician training. Imaging modes include fluorescence, transmission, raw data only, system calibration, and basis spectra acquisition, and once a mode is selected, only relevant options pertaining to that imaging mode appear on the screen. Exposure times may be manually set by the user or automatically determined using an optimization routine which performs test exposures to calculate ideal exposure times for image acquisition. Additional options include real-time spectrum calibration and spectral fitting and automatic neutral density filtering to preferentially decrease filter OD as a function of source-detector distance for measurements not involving fluorescence emission.

III. FLUORESCENCE TOMOGRAPHY IMAGE FORMATION

The MRI-guided finite element method (FEM) image reconstruction implementation is described extensively in a previous publication.[8] In general, the approach used here is as follows.

(1) Acquire FD data [photomultiplier tube (PMT) detection system] at the excitation wavelength and use these data to reconstruct for optical properties, μ_{ax} and μ_{sx}'.
(2) Acquire FD data (PMT detection system) at the emission wavelength and use these data to reconstruct for optical properties, μ_{am} and μ_{sm}'.
(3) Acquire cw transmission data by using the fluorescence excitation laser source and the spectrometer detection system.
(4) Acquire cw fluorescence emission data, calibrate these data using the data acquired in part (3), and use the reconstructed optical properties to recover fluorescence yield, a product of the fluorophore's quantum efficiency η and its absorption coefficient, $\mu_{af}(r)$.

Currently, frequency domain data required for parts (1) and (2) are collected using a separate DOT imaging system used in clinical exams and described in Ref. 23. PMT-based frequency domain capabilities are being integrated into the spectrometer system carts to provide frequency domain and

Downloaded 16 Jul 2008 to 129.170.203.126. Redistribution subject to AIP license or copyright; see http://rsi.aip.org/rsi/copyright.jsp

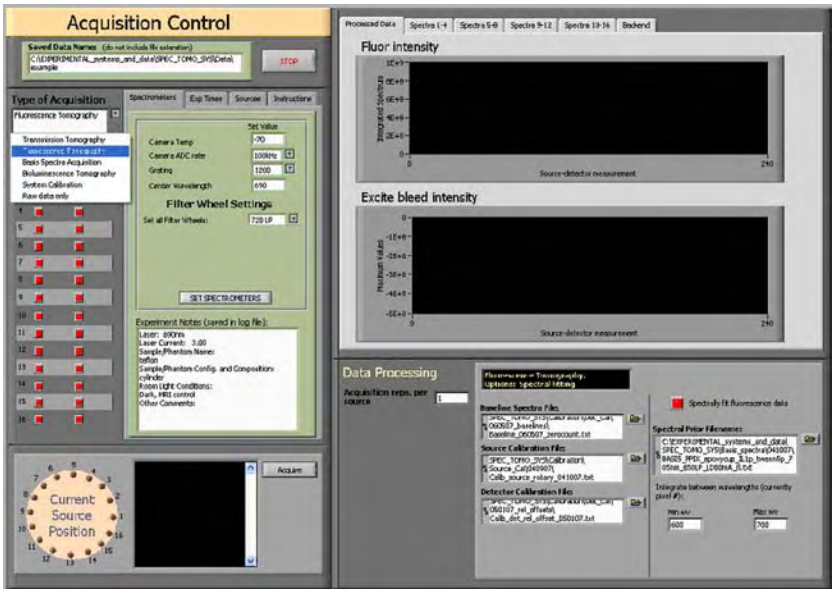

FIG. 7. (Color online) Front panel of the spectroscopy system's image acquisition program.

cw spectroscopic detection in a single system. These modifications are outlined in the Discussion section.

MR images simultaneously acquired with optical data are used to generate the finite element domain for optical tomography image recovery. MR images are segmented using thresholding, region-growing, and manual image manipulation in MATERIALIZE MIMICS software (Ann Arbor, MI). Source/detector fiber optic positions are registered with reference to MR sensitive fiducials attached to the patient or animal fiber interface. Exported mask files are used to generate FEM meshes compatible with the optical tomography modeling and image reconstruction software described in Ref. 8

Two methods are used to incorporate tissue structural information derived from simultaneously acquired MR images into the optical tomography reconstruction algorithm. One approach structures the inverse regularization matrix based on segmented MR images. This is known as a "soft" priors approach since each node independently updates, allowing the recovery of tumor regions not explicitly segmented from the MR image. Alternatively, the "hard priors" approach homogenizes each segmented region and is therefore unyielding in its application of spatial guidance.[24,25]

In the soft priors approach, spatial prior information is incorporated by assuming a "generalized Tikhonov" penalty term that results in a Laplacian-type regularization matrix. To recover images of optical parameters, the difference between measured fluence Φ^{meas} at the tissue surface and calculated data Φ^{C} is minimized. The iterative update equation for the optical properties $\mu=(\mu_a,\kappa)$, where μ_a is the absorption coefficient, κ is the diffusion coefficient, $\kappa=1/3(\mu_a+\mu_s')$, and μ_s' is the reduced scattering coefficient, pertains to steps (1) and (2) above and is given by

$$\Delta\mu_{x,m}=[J^TJ+\beta_{x,m}L^TL]^{-1}J^T(\Phi^{\text{meas}}_{x,\text{trans}_m}-\Phi^{C}_{x,\text{trans}_m}) \qquad (1)$$

for the excitation and emission wavelengths x and m. Once these values are know, the fluorescence yield update can be calculated,

$$\Delta\eta\mu_{af}=[J^TJ+\beta_fL^TL]^{-1}J^T(\Phi^{\text{meas}}_{m}-\Phi^{C}_{m}), \qquad (2)$$

where in both update equations, J is the Jacobian matrix describing the sensitivity of boundary data to the parameter of interest, and β is a fixed fraction multiplied by the maximum value on the diagonal of J^TJ. Spatial prior information is introduced in the dimensionless "filter" matrix L generated using MR images segmented into appropriate tissue regions based on MRI contrast.

The hard priors approach applies stricter constraints than the regularization-based implementation previously described. Nodal values are locked together by implicitly assuming that segmented regions in the imaging domain are homogeneous. In practice, the Jacobian matrix is calculated on a fully resolved mesh at each iteration, but then collapsed into segmented regions for the inversion process. This drastically reduces the update parameter space from the product of number of nodes and number of unknown properties to the product of number of regions and number of unknown properties. Confidence in the segmentation is critical since regions are offered no spatial latitude. Indeed, the hard priors approach is strictly a characterization-based implementation incapable of detection or uncovering false negatives, and therefore does not present as an image recovery problem *per se*.

IV. OPTICAL DATA PROCESSING

The following outlines the data processing procedure for all optical data collected on the spectroscopy system (A–C) as well as additional calibration procedures for fluorescence emission measurements (D).

A. Baseline/dark current correction

Each CCD displays a baseline offset for zero second acquisitions which must be subtracted from the raw spectrum. Multiple repetitions of the baseline offset spectrum were measured for each spectrometer. The median of the repetitions is used as the baseline offset spectrum to be sub-

Downloaded 16 Jul 2008 to 129.170.203.126. Redistribution subject to AIP license or copyright; see http://rsi.aip.org/rsi/copyright.jsp

tracted, pixel by pixel (assuming vertical binning of the CCD chip), from each acquired spectrum. This is done for each spectrometer.

A similar method was used to correct for the dark current of the CCDs. Dark room acquisitions were recorded for a range of exposure times. Measured counts are proportional to exposure time. The counts per exposure time slope was determined per binned pixel for each spectrometer and is used to subtract dark current from recorded spectra. After baseline and dark current correction, spectra are converted to counts per second.

B. Detector calibration

A first order correction is applied to account for heterogeneity in throughput and wavelength dependence for all optical components between the tissue and CCD detector (i.e., detection fibers, input optics, spectrometer optics, and CCD response). Detectors were arranged to circumscribe a 6 cm diameter cylindrical Teflon phantom with an SMA connector attached to the radial center of one end. Light from a high power tungsten white light source was focused into a fiber connected to the centrally located SMA connector. Spectra were recorded with all spectrometers (usually ten repetitions), and interdetector calibration factors were calculated for every vertical pixel bin (total of 1340) for each spectrometer. This was done for each grating and grating position to be used during image acquisitions. Calibration factors are stored and used to scale detected signal in a wavelength dependent manner. This helps reduce the influence of inhomogeneities in the CCD array and partially accounts for throughput variability between detector channels.

A similar approach is used to correct for OD filtering. Since the ND filters have a wavelength dependent response, OD values for every filter were experimentally determined using the spectroscopy system. For a given spectrometer, these values were calculated for each CCD pixel (vertically binned) for each grating/wavelength range selection. In this manner, a calibration file for a given filter setting at a given grating and wavelength setting contains 1340×16 values of optical density, accounting for number of pixels by number of spectrometers.

C. Source calibration

A first order interfiber source strength calibration was recorded by positioning a detector at the radial center of the Teflon cylinder described above. The detected signal from all 16 source fiber positions was used to determine source scaling factors for future acquisition.

D. Fluorescence emission spectral fitting and data-model calibration

Fluorescence emission light is initially decoupled from the often much more intense excitation signal using long pass interference filters which provide between 5 and 7 OD filtering efficiency depending on the filter set and the wavelength selectivity of the spectrograph grating. Even with these components in place, light reaching the CCD retains residual signal not associated with fluorescence emission

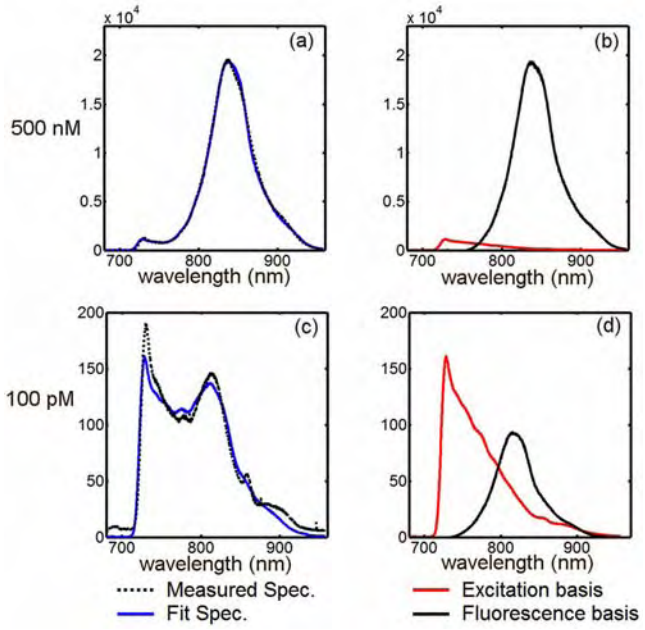

FIG. 8. (Color online) A spectral fitting routine is used to decouple fluorescence spectra from the measured signal. The spectral fitting algorithm determines the relative contribution of the basis spectra [right column, (b) and (d)] which best fits the measured spectrum. Two examples are presented above, both for a 70 mm diameter homogeneous phantom containing intralipid, ink, and ICG [500 nM for graphs (a) and (b) and 100 pM for graphs (c) and (d)].

from the fluorophore target, which can be a significant component of the total signal, especially for cases in which the fluorophore has a low quantum yield or is at low concentrations in the tissue. In order to further decouple the true fluorescence signals, previously recorded "basis spectra" of the residual nonfluorophore originating signal and the pure fluorescence signal are fitted to the data. Each spectrograph is used to record its own fluorescence emission basis spectra and residual excitation basis spectra in a controlled manner. All spectra are normalized to the maximum value. Fitting is accomplished by a linear least squares algorithm that minimizes the summation

$$S = \sum_{i=1}^{N} \{y_i - [aF(\lambda_i) + bG(\lambda_i)]\}^2 \tag{3}$$

with respect to a and b, where y_i is the measured intensity at a given wavelength pixel, F and G are the residual excitation and fluorescence basis spectra, a and b are the coefficients recovered in the minimization procedure, and N is the number of wavelength pixels per spectrum. The algorithm determines the amount of fluorescence emission and excitation cross-talk in the measured spectrum, the sum of which best fits the data in a least squares sense. This procedure is applied to each recorded fluorescence spectrum, a total of 240 spectra for a given acquisition. The spectral fitting procedure is demonstrated for two different ICG concentrations in a homogeneous phantom in Fig. 8. In some cases, the fluorescence peak has been observed to shift to longer wavelengths in large phantom volumes. To account for this, the minimization may incorporate the position of the peak as a free parameter. The resulting fluorescence emission peak is inte-

Downloaded 16 Jul 2008 to 129.170.203.126. Redistribution subject to AIP license or copyright; see http://rsi.aip.org/rsi/copyright.jsp

grated to provide a single fluorescence intensity measurement for a given source-detector pair.

Integrated fluorescence emission measurements are calibrated in the following manner:

$$\Phi_{fl_i}^{\text{calib}} = \Phi_{fl_i}^{\text{meas}} \frac{\Phi_{x_i}^{\text{model}}}{\Phi_{x_i}^{\text{meas_spec}}}, \tag{4}$$

where the index i indicates a single data point or source-detector pair. Φ_x^{model} is the intensity boundary data calculated from the images of μ_{ax} and μ_{sx}' recovered using the frequency domain measurements from the PMT clinical system. This calculated, or "model," boundary data must correspond to the spectrometer fiber positions, which do not necessarily have to be identical to those used in the frequency domain system. The quotient in Eq. (4) essentially provides a scaling factor for the fluorescence measurements which accurately scales the fluorescence data to the FEM model and accounts for inter-detection channel throughput and fiber coupling discrepancies. An initial estimate for the iterative reconstruction algorithm is determined using a homogeneous fitting routine. This procedure uses the bisection method to minimize the data-model misfit, assuming a homogeneous distribution of fluorescence yield.

V. SYSTEM PERFORMANCE

A. Repeatability

An 8.6 cm diameter homogeneous phantom composed of silicone, titanium dioxide, and India ink was used to measure the repeatability of transmission mode measurements using the spectroscopy system. Optical properties of the phantom were approximately 0.004 and 1.91 mm^{-1} for the absorption and reduced scattering coefficients, respectively. Measurements were repeated at each source-detector position using the 690 cw laser source. For a single vertically binned pixel array, the average and maximum standard errors at the laser peak are 1.4% and 1.8%, respectively, if fiber positions were not changed in between measurements. These increase to 18.3% and 19.5% with fiber repositioning, indicating that fiber coupling is the most significant source of error in these measurements. If pixels are binned throughout the laser peak, the average and maximum standard errors change to 0.28% and 0.37% for fibers remaining in contact with the phantom and 14.8% and 16.3% for repositioned fibers.

Determining measurement repeatability in fluorescence mode is less straightforward given the signal dependence on fluorophore concentration, absorption spectrum, and quantum yield. For this study, a 70 mm diameter liquid phantom containing DPBS, 1% intralipid, India ink, and 10 nM ICG was used to determine measurement repeatability. This measure was calculated in two ways, one considered only the raw data for a given binned pixel array and resulted in a mean standard error of 0.7% and maximum standard error of 1.4% for the pixel array at the fluorescence peak. The second measure was determined based on the integrated intensity from the full calibration and spectral fitting routine, resulting in an average standard error of 0.6% and maximum standard error of 1.8%. It is clear that fiber positioning variability would dominate the data error for fluorescence measurements in this case. However, fluorescence measurement data offer a unique opportunity to account for fiber coupling variability. This is accomplished by calibrating the fluorescence measurements to the transmission measurements in the same geometry, as described in Sec. IV D. This provides inherent stability to systematic error, though is not unique to spectrometer-based detection which in and of itself does not necessarily provide a signal to noise ratio (SNR) advantage over more traditional detection schemes used for fluorescence tomography. The benefit of spectrometer based detection is improved separation of the fluorescence signal from background contamination, providing a more accurate ratio, especially for low concentrations of fluorophore.

B. Sensitivity

A 70 mm diameter liquid phantom containing dulbecco's phosphate buffered saline (DPBS), 1% intralipid, and India ink was used to investigate the overall sensitivity of the system to ICG fluorescence. ICG dye dissolved in de-ionized (DI) water was added to the solution to obtain solutions ranging from 10 pM to 1 μM ICG. The optical properties of the intralipid/ink solution μ_a and μ_s' were approximately 0.006 and 1.6 mm^{-1}, respectively. The optical properties at the excitation and emission wavelengths were recovered for each concentration of ICG from data collected using the clinical frequency domain system. Since the domain was known to be homogeneous, these properties were determined in a homogeneous fitting procedure only.

Fluorescence emission and excitation transmission measurements were recorded for each phantom, with a maximum allowed camera integration time of 120 s applied to the fluorescence measurements. The typical data measured across the emission spectrum are shown in Fig. 8(a) for a strong fluorescence signal and Fig. 8(c) for a weak signal. The spectral fitting procedure discussed in Sec. IV D above was used to recover the true fluorescence signal and the nonspecific background contributions, as shown in (b) and (d), respectively. Additionally, to quantitatively compare the spectral fitting procedure to more conventional means of fluorescence filtering, the measured, un-fitted spectra were integrated to simulate 720 nm long-pass filtering. In both cases, integrated values representing fluorescence emission intensities were calibrated as per Eq. (4) and used to determine homogeneous values of fluorescence yield.

Values of fluorescence yield recovered using the two data preprocessing techniques are plotted as a function of known ICG concentration in Fig. 9. The linear fit shown in the figure was computed using the spectrally fit data with the y-intercept forced to zero and indicates a strong linear correlation of recovered fluorescence yield and ICG concentration (R^2=0.99). At concentrations above 1 nM, the fluorescence yield values calculated using data that was filtered only, with no spectral fitting, very closely match the spectrally fit results. Fluorescence signals produced at these fluorophore concentrations dominate the detected signal, a finding consistent with the data shown in Fig. 8. However, fluorescence yield values recovered with spectrally fit data maintain the linear relationship at lower concentrations than those recovered using data without the spectral separation of back-

Downloaded 16 Jul 2008 to 129.170.203.126. Redistribution subject to AIP license or copyright; see http://rsi.aip.org/rsi/copyright.jsp

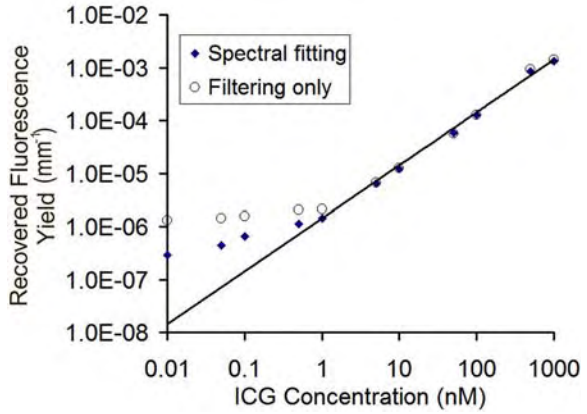

FIG. 9. (Color online) Values of fluorescence yield as a function of ICG concentration in a 70 mm liquid phantom recovered using two methods to process the recorded data. One method uses the spectral-fitting technique to decouple background contamination across the fluorescence emission spectrum, while the other simply integrates the measured spectrum, as would be the case for long pass filtering alone. Values were determined using a homogeneous fitting algorithm for the background optical properties as well as the fluorescence yield.

ground contamination. Clearly, the two techniques diverge at 1 nM. At this concentration, the residuals between the recovered value of fluorescence yield and the linear approximation are 0.4% and 48% for the spectrally fit and filtering-only approaches, respectively. As the fluorophore concentration drops below 1 nM, both techniques lose the consistent linear response observed at higher concentrations, though the filtered-only data show even less sensitivity to changes in fluorophore concentration. At 500 pM, the residuals increase to 57% and 192% for the spectrally fit and filtered-only data processing responses, respectively. Below this level, accurate quantification of fluorescence activity is unlikely in this phantom configuration, however, the spectrally fit data still show a stronger response to changes in fluorophore concentration down to 10 pM. The residuals calculated at the lowest concentration measured were almost five times larger without spectral fitting, clearly indicating a more sensitive, if not accurate, response of the spectral preprocessing technique. It should be noted that since fluorophore quantum yield is not explicitly known in this solution, the calculated slope of the linear regression does not provide information on the actual relationship between true and recovered concentrations, however, the linearity itself is a critical measure of system performance.

C. Phantom imaging

A heterogeneous liquid phantom was used to demonstrate imaging large volumes with imperfect tumor-to-background uptake. The phantom was composed of DPBS, 1% intralipid, and India ink, resulting in background optical properties of $\mu_a = 0.005\ \mathrm{mm}^{-1}$ and $\mu_s' = 1.4\ \mathrm{mm}^{-1}$. ICG dissolved in DI water was added to the phantom volume to obtain a 300 nM ICG solution. A thin-walled plastic cylinder was positioned between the edge and center of the phantom to simulate a 2 cm diameter tumor region. The inclusion consisted of the same solution found in the phantom background, although the ICG concentration was elevated to

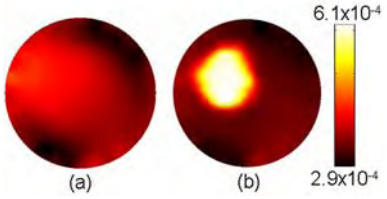

FIG. 10. (Color online) Images of fluorescence yield for a 70 mm diameter liquid phantom containing an ICG heterogeneity. The target-to-background concentration of ICG was 3.3:1. Images reconstructed using spatial soft priors, depicted in (b), are qualitatively more accurate and in terms of recovered contrast than images recovered without the spatial priors implementation (a).

1 μM, providing a total contrast of just over 3.3:1. Background optical properties were determined by imaging the phantom in a separate frequency domain clinical system and values at 785 nm were used for this experiment. The spectroscopy system was then used to acquire excitation intensity and fluorescence emission measurements. Integrated intensities were calibrated to the model as described earlier, and images were reconstructed using an algorithm without spatial guidance as well as the soft spatial priors implementation. The resulting images are shown in Fig. 10. Tumor-to-background contrast can be deciphered in both images; however, the spatially guided implementation provides a more accurate representation of the imaged domain. Inclusion borders are more clearly defined and the image represents substantially higher tumor-to-background contrast.

D. Small animal imaging

An animal pilot study demonstrates the ability of the system to image an epidermal growth factor receptor (EGFR) targeted fluorescent probe in mouse brain tumors. U-251 human glioma tumors were implanted intracranially in male nude mice 19 days prior to the imaging study. Simultaneous gadolinium enhanced T1 MRI and fluorescence tomography acquisition of the population were completed prior to IRDye® 800CW EGF Optical Probe (LI-COR Biosciences, Lincoln, NE) IV administration (1 nM) and at 24 h intervals after injection over the course of 72 h. Eight fibers were used in this study, and fiber-tissue contact positions were determined in reference to MRI sensitive fiducials on the molded mouse bed. For each imaging session, a single coronal slice was segmented into regions using MATERIALIZE MIMICS software. The example in Fig. 11 shows an MR coro-

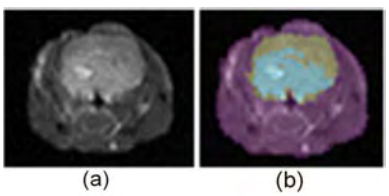

FIG. 11. (Color online) A gadolinium enhanced T1-weighted image shows a coronal slice of a tumor bearing mouse head (a). The image is segmented into three regions using MIMICS software (b), the largest region (violet) identifies the tissue outside of the brain, the second largest region (gray) is the brain itself, and the smallest region (light blue) marks the tumor. The segmented image is used to generate an FEM mesh for spatially guided fluorescence reconstruction.

Downloaded 16 Jul 2008 to 129.170.203.126. Redistribution subject to AIP license or copyright; see http://rsi.aip.org/rsi/copyright.jsp

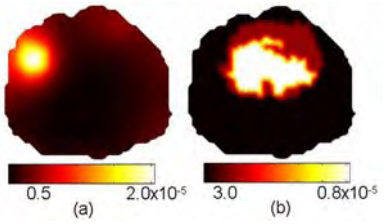

FIG. 12. (Color online) Reconstructed images of fluorescence yield for a tumor bearing mouse using only the outer boundary for spatial priors (a) and using spatial hard priors (b).

nal slice of one mouse 48 h after IRDye® 800CW EGF Optical Probe administration and the resulting MR image. The regionized mask was exported as a bitmap file from which a two dimensional mesh was generated for fluorescence reconstruction.

The spectral fitting technique described in Sec. IV D was used to generate integrated intensity values of fluorescence emission from basis spectra of EGF Optical Probe fluorescence. Reconstructed images with and without the use of hard spatial priors are presented in Fig. 12. The conventional diffuse tomography approach makes no use of the internal tissue structure although the outer boundary of the domain was used in this case. Fluorescence yield values recovered using this approach are highly surface weighted, showing an elevated region of fluorescence activity near the surface of the mouse head, well outside the actual location of the tumor. The diffuse, Gaussian shape of the elevated region is typical of fluorescent molecular tomography imaging without spatial guidance.[3,5,26–31] The use of hard priors, as implemented here, transforms the imaging problem to one of quantification since the recovery of the tumor region size and location is not the ultimate objective. In this case, the tumor region outline is given by a region-growing threshold of the enhanced MR image, and the fluorescence recovery algorithm estimates the fluorescence uptake in that predefined region. An important test will be how the hard priors implementation handles false positives in healthy regions, and nontumor bearing mice, introduced by incorrect MR segmentation, and these studies are ongoing.

VI. DISCUSSION

An MRI-coupled optical tomography system has been developed to image fluorescence yield in a variety of tissue volumes. A unique rodent coil specifically developed for this system provides high resolution MR images of small animals. Through a variety of spatial prior implementations, these images provide the imaging template upon which the fluorescence activity is reconstructed. The system's high sensitivity, low noise CCD detectors were shown to be stable and provide repeatable measurements, the most significant error originating from fiber coupling errors. Fluorescence emission intensity may be scaled to the excitation laser transmitted intensity to account for these errors.

Characterizing the system's sensitivity to fluorophore concentration is complex, given the dependence on concentration, absorption spectra, excitation filtering, and quantum yield. Sensitivity results of a commonly used fluorophore in a reasonably sized phantom were presented and demonstrated a linear response of the fluorescence yield fit to fluorophore concentration down to 1 nM using spectral fitting data preprocessing. Without spectral fitting, recovered values for 1 nM and below are inaccurate, and the sensitivity slope begins to flatten at these concentrations. This reduction in sensitivity is also observed for spectrally fit data, although the decrease in the response slope is less dramatic and does not show up until concentrations of 500 pM. Below this level, there is still a modest response to changing fluorophore concentrations, although the recovered values are clearly inaccurate. This is not caused by a drop in measurement SNR *per se*, as the measured signal even at 10 pM is strong and stable, but may be due to systematic bias in the spectral fitting routine itself, inaccuracies in the basis spectra, or the presence of a contaminating signal with similar spectral characteristics to ICG.

Preliminary imaging studies demonstrate an ability to image low fluorescence contrast (3.3:1 ratio) in relatively large tissue volumes (70 mm diameter), contingent upon the availability of spatial prior information provided by the MRI. Additionally, it was also shown that quantifying the uptake of a targeted fluorophore in a mouse glioma model is feasible and dramatically benefits from the inclusion of structural information, through the synergy of MR imaging and fluorescence estimation of the regionized image. A larger mouse population study is currently underway to further characterize *in vivo* imaging performance, and quantify the variation in estimated uptake of fluorophores in tumors.

The work presented here required the use of a separate frequency domain imaging system to obtain background optical properties and calibrate the fluorescence data to the algorithmic model. This is inconvenient at best and limits many of the advantages of the MRI-coupled imaging system. Importantly, the lack of FD imaging capabilities integrated into the imaging system, background optical properties may not be acquired without repositioning the subject. Integrating PMT-based frequency domain detection into the spectroscopy system is underway. The rotating source coupling stage was constructed with 15 PMT detectors in a design identical to that previously reported.[23] In this configuration, the source branch of the spectroscopy fibers will serve as both light delivery and pickup channels for the PMT's.

The unique system introduced here provides rich spectral information in a variety of diffuse optical imaging modes including broadband NIR transmission and fluorescence at present. In fluorescence mode, the spectrograph system offers several advantages over filtered intensity measurements as spectrally resolved detection provides exceptional wavelength selectivity for excitation filtering. The excitation contamination and nonspecific background can be dramatically suppressed to improve the ability to quantify low level fluorescence, as was shown here. The system may also be used in the future to acquire emission data from multiple fluorophores simultaneously, contingent upon the individual fluorescence peaks being resolved well enough for the spectral fitting technique to extract the contribution from each fluorophore.

Downloaded 16 Jul 2008 to 129.170.203.126. Redistribution subject to AIP license or copyright; see http://rsi.aip.org/rsi/copyright.jsp

ACKNOWLEDGMENTS

This work was funded by the National Institutes of Health Grants No. RO1 CA109558, RO1 CA69544, and U54 CA105480, Philips Research Hamburg, as well as Department of Defense Breast Cancer predoctoral fellowship BC051058.

[1] N. Deliolanis, T. Lasser, D. Hyde, A. Soubret, J. Ripoll, and V. Ntziachristos, Opt. Lett. **32**, 382 (2007).
[2] H. Meyer, A. Garofalakis, G. Zacharakis, S. Psycharakis, C. Mamalaki, D. Kioussis, E. N. Economou, V. Ntziachristos, and J. Ripoll, Appl. Opt. **46**, 3617 (2007).
[3] S. V. Patwardhan, S. R. Bloch, S. Achilefu, and J. P. Culver, Opt. Express **13**, 2564 (2005).
[4] J. Ripoll, R. B. Schulz, and V. Ntziachristos, Phys. Rev. Lett. **91**, 103901 (2003).
[5] R. B. Schulz, J. Ripoll, and V. Ntziachristos, IEEE Trans. Med. Imaging **23**, 492 (2004).
[6] G. Zacharakis, J. Ripoll, R. Weissleder, and V. Ntziachristos, IEEE Trans. Med. Imaging **24**, 878 (2005).
[7] A. Corlu, R. Choe, T. Durduran, M. A. Rosen, M. Schweiger, S. R. Arridge, M. D. Schnall, and A. G. Yodh, Opt. Express **15**, 6696 (2007).
[8] S. C. Davis, H. Dehghani, J. Wang, S. Jiang, B. W. Pogue, and K. D. Paulsen, Opt. Express **15**, 4066 (2007).
[9] A. Godavarty, M. J. Eppstein, C. Zhang, and E. M. Sevick-Muraca, Radiology **235**, 148 (2005).
[10] A. Godavarty, A. B. Thompson, R. Roy, M. Gurfinkel, M. J. Eppstein, C. Zhang, and E. M. Sevick-Muraca, J. Biomed. Opt. **9**, 488 (2004).
[11] A. Godavarty, C. Zhang, M. J. Eppstein, and E. M. Sevick-Muraca, Med. Phys. **31**, 183 (2004).
[12] R. Choe, A. Corlu, K. Lee, T. Durduran, S. D. Konecky, M. Grosicka-Koptyra, S. R. Arridge, B. J. Czerniecki, D. L. Faker, B. Chance, M. A. Rosen, and A. Yodh, Med. Phys. **32**, 1128 (2005).
[13] A. Corlu, R. Choe, T. Durduran, K. Lee, M. Schweiger, S. R. Arridge, E. M. Hillman, and A. Yodh, Appl. Opt. **44**, 2082 (2005).
[14] A. Corlu, T. Durduran, R. Choe, M. Schweiger, E. M. Hillman, S. R. Arridge, and A. G. Yodh, Opt. Lett. **28**, 2339 (2003).
[15] A. Li, Q. Zhang, J. Culver, E. Miller, and D. Boas, Opt. Lett. **29**, 256 (2004).
[16] S. Srinivasan, B. W. Pogue, B. Brooksby, S. Jiang, H. Dehghani, C. Kogel, W. A. Wells, S. P. Poplack, and K. D. Paulsen, Technol. Cancer Res. Treat. **4**, 513 (2005).
[17] S. Srinivasan, B. W. Pogue, S. Jiang, H. Dehghani, C. Kogel, S. Soho, J. J. Gibson, T. D. Tosteson, S. P. Poplack, and K. D. Paulsen, Acad. Radiol. **13**, 195 (2006).
[18] S. Srinivasan, B. W. Pogue, S. Jiang, H. Dehghani, and K. D. Paulsen, Appl. Opt. **44**, 1858 (2005).
[19] B. Brooksby, S. Jiang, C. Kogel, M. Doyley, H. Dehghani, J. B. Weaver, S. P. Poplack, B. W. Pogue, and K. D. Paulsen, Rev. Sci. Instrum. **75**, 5262 (2004).
[20] M. Guven, B. Yazici, X. Intes, and B. Chance, Phys. Med. Biol. **50**, 2837 (2005).
[21] X. Intes, C. Maloux, M. Guven, B. Yazici, and B. Chance, Phys. Med. Biol. **49**, N155 (2004).
[22] B. W. Pogue, Z. Li, C. Carpenter, A. Laughney, V. Krishnaswamy, S. C. Davis, S. Jiang, and K. D. Paulsen, International Society for Optical Engineering (SPIE) BiOS at Photonics West, San Jose, California, 2008 (unpublished).
[23] T. O. McBride, B. W. Pogue, S. Jiang, U. L. Osterberg, and K. D. Paulsen, Rev. Sci. Instrum. **72**, 1817 (2001).
[24] H. Dehghani, B. W. Pogue, S. Jiang, B. Brooksby, and K. D. Paulsen, Appl. Opt. **42**, 3117 (2003).
[25] M. Schweiger and S. R. Arridge, Phys. Med. Biol. **44**, 2703 (1999).
[26] V. Ntziachristos, C. H. Tung, C. Bremer, and R. Weissleder, Nat. Med. **8**, 757 (2002).
[27] E. Graves, J. Ripoll, R. Weissleder, and V. Ntziachristos, Med. Phys. **30**, 901 (2003).
[28] V. Ntziachristos, E. A. Schellenberger, J. Ripoll, D. Yessayan, E. Graves, A. Bogdanov, Jr., L. Josephson, and R. Weissleder, Proc. Natl. Acad. Sci. U.S.A. **101**, 12294 (2004).
[29] E. E. Graves, R. Weissleder, and V. Ntziachristos, Current Molecular Medicine **4**, 419 (2004).
[30] G. Zacharakis, J. Ripoll, R. Weissleder, and V. Ntziachristos, IEEE Trans. Med. Imaging **24**, 878 (2005).
[31] E. E. Graves, D. Yessayan, G. Turner, R. Weissleder, and V. Ntziachristos, J. Biomed. Opt. **10**, 0440191 (2005).

Downloaded 16 Jul 2008 to 129.170.203.126. Redistribution subject to AIP license or copyright; see http://rsi.aip.org/rsi/copyright.jsp

Spectral Distortion in Diffuse Molecular Luminescence Tomography in Turbid Media

Scott C. Davis[1], Brian W. Pogue[1], Stephen B. Tuttle[1], Hamid Dehghani[1,2], Keith D. Paulsen[1]

1. Thayer School of Engineering, Dartmouth College, Hanover, New Hampshire 03755

2. School of Physics, University of Exeter, Exeter, UK EX4 4QL

Scott.C.Davis@dartmouth.edu, Brian.W.Pogue@dartmouth.edu

Manuscript in Press

ABTRACT

The influence of tissue optical properties on the shape of near-infrared (NIR) fluorescence emission spectra propagating through multiple centimeters of tissue-like media is investigated. Experimentally measured fluorescence emission spectra measured in 6 cm homogeneous tissue-simulating phantoms shows dramatic spectral distortion which results in emission peak shifts of up to 60 nm in wavelength. Measured spectral shapes are highly dependent on the photon path-length and the highly scattered photon field in the NIR amplifies the wavelength-dependent absorption of the fluorescence spectra. Simulations of the peak propagation using diffusion modeling describe the experimental observations and confirm the path-length dependence of fluorescence emission. Spectral changes are largest for longer path-length measurements, and this will be most dominant in human tomography studies in the NIR. Spectrally resolved or multi-wavelength band-pass measurements are required to detect these changes, and may be essential to interpret such effects, which would otherwise be attributed to erroneous intensity measurement. This phenomenon is analogous to beam hardening in x-ray tomography, which can lead to image artifacts without appropriate compensation. The

peak shift toward longer wavelengths, and therefore lower energy photons, observed for NIR luminescent signals propagating through tissue may readily be described as a beam softening phenomenon.

Manuscript in Press

INTRODUCTION

Diffuse spectroscopy and imaging of tissue using luminescent signals from molecular reporters has become a major area of interest in recent years[1-4]. Much of this research is focused on exploiting novel biochemical probes, developing new detection strategies, improving image recovery methods[5-8], and coupling luminescence detectors to existing imaging systems[9,10]. Image recovery or quantitative spectroscopy of tissue requires accurate light transport modeling which is now a fairly mature field of research which has seen substantial growth since the early 1990s[11]. While fluorescence molecular imaging and spectroscopy systems for use in small animals[4,10,12-16] have evolved to the point of commercial availability and clinical trials in humans are underway[17], some of the more subtle complexities of the signal acquisition remain to be examined. One important consideration that has not been investigated in detail, especially in the near-infrared (NIR), is the interaction between the remission spectrum of the reporter and the intervening tissue through which the light transport occurs prior to detection. In particular, changes in spectral emission can be detected which are intimately linked to the tissue optical properties and the path-length of signal travel involved. In this study, a systematic evaluation of NIR spectral shift has been completed using simulations and tissue phantoms.

As interest in fluorescence spectroscopy for tissue diagnosis grew, researchers began to develop methods to compensate for spectral distortion due to tissue optical properties in order to recover intrinsic fluorescence spectra. Original work reported by Wu et al.[18], Durkin et al.[19] and Richards-Kortum et al.[20], examined photon migration, Kubelka-Munk and exponential models, respectively, to extract intrinsic autofluorescence

Manuscript in Press

signals from the measured distorted spectrum emitted from tissue. In 1996, Durkin et al.[21] compared several modeling approaches and determined that a partial least squares method yielded an accurate spectral correction. Analytical expressions derived by Gardner et al.[22] were used to extract spectra measured through tissue samples on the order of 1 cm. In 2001, Müller et al.[23] provided a comprehensive investigation of the effects of absorption and scattering on intrinsic fluorescence extraction based on a photon migration model.

All of these efforts were focused on tissue spectroscopy in the visible spectrum where autofluorescence is high and the significant photon attenuation restricts the distances over which light signals can be measured to a few centimeters. The relatively low attenuation in the near-infrared (NIR) allows measurable light penetration over 10 cm, though elastic scattering ensures most photons will change direction within 1 mm of entering the tissue. Photon propagation in the NIR is commonly modeled using the diffusion approximation to the radiative transport equation. While Patterson and Pogue[24] developed a general construct for modeling fluorescence propagation through homogeneous tissues based on diffusion theory, they did not consider the spectral distortion in the detected emissions directly. Some investigators[25,26] have recognized the inherent depth information contained in the spectral distortion and have demonstrated the ability to localize fluorescent layers in tissue simulating phantoms by calculating the ratio of emitted intensity at different wavelengths.

With the development of NIR diffuse tomography for imaging endogenous tissue contrast through centimeters of tissue, extensions of the theoretical framework to incorporate fluorescence detection have been sought to enhance the disease-to-normal

Manuscript in Press

tissue contrast and target molecular processes using fluorescent contrast agents[27-33]. Systems have been developed to collect fluorescence intensities from an array of source-detector positions surrounding the tissue of interest and model-based reconstruction techniques have been used to recover fluorescence activity by matching the modeled and measured data using optimization techniques. Most experimental systems employ one or more band-pass or long-pass filters to separate the excitation signal from the fluorescence emission, but rarely has the capability to resolve the fluorescence spectrum been incorporated. Recently, it was shown[10,34] that a spectrally resolved fluorescence tomography scanner that employs spectrometer detection can record fluorescence spectra emitted from tissue. Ignoring the spectral changes in deep tissue imaging may have implications for quantitative accuracy of the recovered images, especially for systems that use relatively large emission wavelength ranges. Since wavelength-dependent attenuation of the fluorescence emission increasingly distorts the measured spectrum as photon path-length increases, the effect is expected to become more pronounced when imaging through larger tissue domains, such as the human breast.

This work investigates NIR fluorescence emission distortion using homogeneous turbid phantoms and diffusion based modeling. The model platform, NIRFAST, has been developed previously[34,35] using the Finite Element Method (FEM) which allows consideration of arbitrarily shaped domains with heterogeneous optical properties. Here, the model system is extended to calculate spectrally resolved emission spectra at discrete wavelengths based on fluorescence spectra of dilute solutions and wavelength-dependent optical properties of tissue. Experimentally measured spectra are compared with spectra generated using the model system. Phantom geometries are representative of the

Manuscript in Press

dimensions to be encountered in tomographic imaging of fluorescence activity *in vivo* and the potential implications that spectral distortion has for tomographic imaging of fluorescence are discussed.

EXPERIMENTAL DETAILS

Phantom design

Phantoms designed to simulate the optical properties of commonly imaged tissue types, typically adipose and fibro-glandular breast tissue, were used to investigate the spectral distortion of the detected emission of a distributed fluorescent drug. Two techniques were used to produce tissue-simulating phantoms[36,37]. Liquid phantoms were composed of water or phosphate buffered solution (PBS) and intralipid, which is a fatty suspension that scatters light much like real tissue. Typically, a 1% intralipid solution can be used to mimic tissue scattering in the NIR. The fluorescent contrast agent may then be added in the desired concentration. Absorbing suspensions such as India ink or whole blood may also be added to provide appropriate amounts of optical absorption beyond that introduced by the fluorophore, though these were not used in this study. Though simple to prepare and flexible in terms of composition, the container walls introduce unwanted heterogeneity and light piping effects.

Gelatin phantoms composed of gelatin extracted from porcine skin (Sigma Aldrich), TiO_2, blood and the exogenous contrast agent can be made to closely mimic heterogeneous tissue without artificial boundaries. The mixing procedure used here began by stirring 40g of Type A porcine skin gelatin (Sigma Aldrich) into 500ml water or PBS. Once dissolved, the solution was heated to about 40 C in a microwave oven until

Manuscript in Press

the solution was fully transparent (approximately 1 minute). Immediately after heating, the solution was stirred for 40 minutes. In cases where scattering was required, 0.4g of TiO_2 powder (Sigma Aldrich) was slowly added at the beginning of the stirring procedure. It is critical that the media appear homogeneously cloudy with few visible aggregates of TiO_2 after 20 minutes of stirring. Towards the end of the 40 minutes, the fluorescent drug was added while the solution is still viscid. Once mixed well, the solution was poured into a mold lined with petroleum jelly and refrigerated for at least one hour. The cured phantom slid out of the mold easily. Photographs of liquid and gelatin phantoms used in this study are shown in

Manuscript in Press

FIGURE CAPTIONS

Fig. 1.

The fluorescent drug investigated was Lutetium Texaphyrin (LuTex), a water soluble dye developed as a photodynamic therapeutic sensitizer. It is a texaphyrin based molecule with lutetium in the center to induce a large triplet state splitting[38]. The absorbance and fluorescence emission peaks in dilute solution occur at approximately 735 nm and 750 nm, respectively. Fig. 2 shows a normalized fluorescence emission spectrum of LuTex in a dilute solution of DI (deionized) water measured by a standard fluorometer (Yvon Jobin).

Experimental system

The measurement system was a fluorescence tomography scanner designed to detect low levels of light emitted from thick tissue samples (up to 10 cm). A detailed description of this instrument can be found in Davis et al.[10]. The imaging array used in the studies reported here consisted of 16 source/detector fibers surrounding a cylindrical tissue phantom as shown in Fig. 3. Each fiber is bifurcated with one branch terminating on a rotary stage which serially couples light from a 690 nm CW laser diode into any one of the fibers. The other branch couples light from the phantom surface into one of 16 Insight:400F Spectroscopy units with cooled CCD detection (Princeton Instruments, Acton MA). Automated filter wheels filter the detected light before it enters the spectrograph slit. In the studies presented here, 720 nm long pass filters were used to suppress the excitation light in the measured fluorescence emission signal. In this study, only a single source fiber was illuminated and fluorescence measurements recorded at

Manuscript in Press

various locations around the tissue phantom and thus the system was not used to acquire tomographic data.

Modeling Light Propagation

Near-infrared light propagation in tissue is often modeled by the diffusion approximation, a simplification of the radiative transport equation applicable in media dominated by photon scattering. Modeling fluorescence excitation and emission in tissue is accomplished through a system of diffusion equations which describe the photon field produced by incident excitation light and fluorescence emission from a distributed fluorophore. Specifically, the excitation source, $q_0(r)$, produces an excitation fluence rate, $\Phi_x(r)$, throughout a medium with optical properties $\mu_{ax}(r)$ and $\mu_{sx}^{/}(r)$ representing the absorption and reduced scattering coefficients respectively. The field of excitation photons drives the fluorescence emission which propagates through the tissue subject to optical properties $\mu_{am}(r)$ and $\mu_{sm}^{/}(r)$ at the emission wavelengths. The coupled equations describing this process are presented for the continuous wave case which matches the instrumentation in

Manuscript in Press

FIGURE CAPTIONS

Fig. 1 [27,32]:

$$-\nabla\cdot\kappa_x(r,\lambda_x)\nabla\Phi_x(r,\lambda_x)+(\mu_{ax}(r,\lambda_x))\Phi_x(r,\lambda_x)=q_0(r,\lambda_x) \quad (1)$$

$$-\nabla\cdot\kappa_m(r,\lambda_m^i)\nabla\Phi_{fl}(r,\lambda_m^i)+(\mu_{am}(r,\lambda_m^i))\Phi_{fl}(r,\lambda_m^i)=\Phi_x(r)\eta(\lambda_m^i)\mu_{af}(r) \quad (2)$$

where subscripts *x* and *m* represent the excitation and emission fluence at wavelengths λ_x and λ_m, respectively and the diffusion coefficient is $\kappa_{x,m}=\frac{1}{3(\mu_{ax,m}+\mu_{sx,m}')}$. The source term in Eq. (2) is a product of the excitation photon field and the fluorescence yield, defined as $\eta(\lambda_m^i)\mu_{af}(r)$, which itself is a product of the fluorophore's quantum efficiency η and its absorption coefficient, $\mu_{af}(r)$, at the excitation wavelength.

Unlike the excitation field, which is assumed to arise from a light source at a single excitation wavelength, the emission spectrum of the fluorophore can cover several hundred nanometers. To account for this spectral bandwidth in the numerical model, Eq. (2) is discretized over a wavelength range indicated by the index *i*. Though the excitation field and fluorophore absorption coefficient in the source term of Eq. (2) do not depend on emission wavelength, the fluorescence source strength varies with wavelength based on the shape of the emission spectrum of the fluorophore. This is introduced into the model through a wavelength-dependent fluorescence quantum yield, $\eta(\lambda_m)$. The fluorescence emission propagates through the tissue subject to wavelength-dependent optical properties, $\mu_{am}(r,\lambda_m)$ and $\mu_{sm}'(r,\lambda_m)$, which must be modeled to accurately describe the fluorescence spectrum measured at the tissue surface. In practice, this is

Manuscript in Press

accomplished by first calculating the excitation field in Eq. (1), and then solving for the emission field in Eq. (2) at wavelength λ_m^i for each *i*.

Type III boundary conditions (also known as Robin or mixed) are used to describe the fractional loss of photons at the tissue-air interface. The flux leaving the external boundary is described by:

$$\Phi_{x,m}(\xi) + 2A\hat{\mathbf{n}} \cdot \kappa_{x,m}(\xi)\nabla\Phi_{x,m}(\xi) = 0 \tag{3}$$

where ξ is a point on the external boundary, and *A* is derived from Fresnel's law and depends upon the relative refractive index (RI) mismatch between tissue, Ω, and air;

$$A = \frac{2/(1-R_0) - 1 + \left|\cos\theta_c\right|^3}{1 - \left|\cos\theta_c\right|^2} \tag{4}$$

where θ_c is the angle at which propagation from within the domain undergoes total internal reflection at the boundary and

$$R_0 = \frac{(n_1 / n_{AIR} - 1)^2}{(n_1 / n_{AIR} + 1)^2}. \tag{5}$$

The FEM is used to discretize the domain of interest for numerical modeling of the light propagation which was performed with the NIRFAST software package developed for forward and inverse diffuse tomographic imaging of tissue. A complete description of the numerical implementation can be found elsewhere[8,34,35,39].

Manuscript in Press

The emission spectrum of LuTex was modeled from 700 nm to 850 nm in intervals of at most 10 nm. Some intervals were smaller given the availability of information at additional wavelengths. The extinction spectrum of LuTex was measured directly using a Cary 50 UV-Vis spectrophotometer (Varian, Inc., Palo Alto CA). Absorption coefficients at each wavelength were calculated as a sum of the constituent chromophores, usually oxygenated and deoxygenated hemoglobin, water, and the exogenous agent of interest, however, since whole blood was not used in the phantom experiments, only water and LuTex were considered in the numerical portion of the study. Published values for the extinction spectrum of water, compiled by Prahl[40], were used to calculate the absorbing contribution of water. Scattering properties of tissue in the NIR are commonly modeled using an empirical approximation integrated into the NIRFAST software[41].

Manuscript in Press

RESULTS AND DISCUSSION

Phantom results

Emission spectra measured through homogeneous gelatin and water phantoms containing 5 μM LuTex and no scattering media are presented in Fig. 4. The phantoms were 60 mm diameter cylindrical shapes with a single source and multiple detectors around the outer surface in one plane. Data presented are for different source-detector position on the boundary. As the photon path-length increases, the influence of the media changes the emission spectra modestly and thus the emission peak is not significantly distorted when measured through these phantoms.

In turbid phantoms of the same size, the emission spectra change dramatically. LuTex emission spectra measured for a range of source-to-detector distances around a cylindrical turbid phantom are presented in Fig. 5. Data for spectra measured through both gelatin and liquid phantoms are shown and illustrate the significance of the peak distortion through several centimeters of turbid media. Source-detector distances were 1.1, 3.3, 4.9, and 5.9 cm for the spectra included in the figure. Within 1 cm, the measured fluorescence spectrum is similar to the dilute sample, though a secondary peak is evident around 800 nm in both phantoms. As the source-detector distance increases, the spectra are changed more dramatically. The secondary peak becomes increasingly prominent and as the propagation distance increases, the entire spectrum settles to a single peak at 820 nm.

Photon path-length may be altered by source-detector geometry or by changes in scattering properties. Fig. 6 demonstrates the influence of intralipid concentration on the measured emission spectrum. The spectral changes observed as result of increasing intralipid concentration are similar to those observed with increasing source-detector distance, as expected.

Manuscript in Press

Diffusion modeling

When modeling photon propagation through the phantoms, it was assumed that the dominant absorbers were water (100%) and LuTex. Extinction spectra of water and LuTex were used to calculate the absorption coefficients at discrete wavelengths across the range covered by the emission spectrum. These values are plotted as a function of wavelength in Fig. 7 and illustrate the large change in absorption due mostly to the

fluorophore's absorbance. These values were used to determine the fluorescence intensity at each wavelength throughout the emission spectrum.

Emission intensities determined from the diffusion model at discrete 10 nm wavelength intervals from 700 to 850 nm are shown in Fig. 8 for the same source-detector positions measured through phantoms and presented in Fig. 5. Experimental data from intralipid phantoms are also plotted for comparison (blue line) and the red dotted line represents the fluorescence peak in a dilute solution. All spectra are normalized to their peaks. Significantly, the general trends recorded in the phantom experiments are also observed for the numerical model. At the detector nearest the source, about 1 cm, the measured fluorescence emission peak is shifted about 10 nm to the red and a small secondary peak is visible at 810 nm, similar to what was observed in the phantom data. This corresponds to a very small bump in the absorption spectrum at 800 nm, which emerges as a dip in the emission spectrum and creates the secondary peak. Increased source-detector distances result in more substantial changes to the emission spectrum, and an amplification of the influence of the small elevation in absorption at 800 nm. The fluorescence distortion recorded at the detector positioned just over 3 cm from the source results in a peak at 790 nm and a more pronounced dip at 800 nm is observed, producing a stronger secondary peak. The original peak at 750 nm is almost entirely absorbed. At longer source-detector distances, the emission peak settles at 830 nm, similar to the phantom results, though the increase of absorption at 800 nm is more pronounced for the simulation results.

Qualitative assessment of Fig. 8 reveals reasonable agreement between model and experimental observations in turbid phantoms in terms of emission spectrum shape,

Manuscript in Press

especially for detector locations far from the source. Pearson correlation coefficients between the model and data were calculated as 0.50, 0.90, 0.97 and 0.94 for the source-detector distances of 1.1, 3.3, 4.9, and 5.9 cm, respectively. The presence of tissue scattering increases the path-length of photons propagating through the tissue, which in turn amplifies the influence of the tissue's absorption spectrum. The significance of the peak distortion also indicates that the primary source of fluorescence detected at the far-source detectors is generated close to the source excitation source, where the excitation field is most intense, and then propagates through the tissue. This is an expected result since photon penetration depth at the excitation wavelength is lower than within the emission wavelength range due to higher absorption.

Implications for fluorescence tomography in deep tissue

The extent of the spectral distortion observed will depend on the fluorophore used, the tissue chromophore composition, and the excitation and measurement geometry. Other drugs used for imaging may experience less distortion than that associated with LuTex. However, the observed phenomenon has implications for quantitative fluorescence tomographic imaging. Clearly, the results presented here indicate that spectrally resolved or band-pass filtering is preferred over long-pass filtering of fluorescence signals.

To demonstrate the extent to which spectrally unresolved data impacts fluorescence imaging in deep tissue, a simulated example using an 86mm circular test domain to represent a coronal slice of a human breast is considered. To create a realistic test domain, tissue optical properties were calculated directly using the extinction spectra

Manuscript in Press

of the dominant endogenous chromphores and typical tissue concentrations of those chromophores. LuTex was assumed to be the exogenous fluorrophore and extinction coefficients of both endogenous and exogenous chromophores used in this example are shown in Fig. 9 along with the spatial distributions of the chromophores for the coronal slice under consideration. In this case, two small Lutex heterogeneities were included at contrasts of just over 3:1 and 2.5:1 over the background. A large heterogeneity with contrast in hemoglobin and water was also added. Scattering properties were held constant in the domain.

Noise-free data were generated using the forward model described above and signal contamination due to excitation cross-talk and tissue autofluorescence was ignored. Images of fluorescence yield were recovered using diffusion-based optimization reconstruction techniques described extensively elsewhere [34,35]. Identical reconstruction algorithms were used to consider data detected using one of two measurement approaches. The first approach assumed that measured data was fully wavelength resolved. The intensity recorded at the tissue surface at a single wavelength was extracted and optical properties at that wavelength were used in the model-based reconstruction algorithm. The second approach simulated an experimental system using only long-pass filters. Since spectral selectivity within the emission spectrum is impossible in this configuration, the measured spectrum at each detector was integrated. Tissue optical properties were chosen to match those at 750 nm, the fluorescence emission peak in dilute solution. Although the spatial heterogeneity of these optical properties was assumed to be known exactly at this wavelength, the lack of spectral

Manuscript in Press

resolution does not account for the variation of optical properties across the integrated spectrum.

Reconstructed images using both techniques are shown alongside the target image of fluorescence yield in Fig. 10. The only difference between the two approaches arises from the handling of the detected fluorescence spectra. Images reconstructed using spectrally resolved data at a single wavelength show accurate recovery of fluorescence activity in the domain. Recovered values in the contrast enhanced regions are slightly off target values, though this is expected given the reported trade-off between enhanced region size and recovered contrast[42]. Overall, quantification and localization are excellent. Certainly, this is to be expected given the simple geometry and noise-free data. However, the data-model misfit error introduced by integrating the full spectrum is too much for the imaging algorithm and complete breakdown in imaging performance is observed, even for this relatively simple domain. The data provide no ability to localize or quantify fluorescence contrast enhancement. The failure of the algorithm using these data indicates that the long-pass filtering approach is intractable for experimental imaging, making spectrally-resolved detection imperative for accurate image recovery. The extent to which this applies can be investigated by varying the wavelength range over which the spectrum is integrated to determine the widest filter band width at which image artifacts are insignificant.

The dramatic influence of chromophore absorption on the fluorescence spectrum leaving the tissue clearly indicates that the spectral shape contains information related to the location of the emitting source. It is reasonable to postulate that this information can be exploited to improve tomographic fluorescence imaging *in vivo*, presuming spatial

Manuscript in Press

distributions of tissue chromophore concentrations are known *a priori* and the measured emission spectrum contains insignificant background signal. Similar approaches have been used in bioluminescence imaging of small animals[43,44] and may easily be adapted to fluorescence image reconstruction.

SUMMARY

The problems of spectral shift are well known in many imaging applications such as x-ray computed tomography, where high atomic number materials can cause a larger than expected attenuation of the longer wavelength photons, and shift the spectrum to higher energies, a phenomenon known as beam hardening[45]. Luminescent peaks propagating through tissue in the NIR, on the other hand, exhibit shifting towards lower energy photons, a phenomenon which softens the photon field. The principles in both cases are quite similar in that the spectrum to be detected is not attenuated equally as it traverses the medium.

A dramatic fluorescence emission peak shift in the NIR was demonstrated in tissue simulating phantoms, and this effect is especially pronounced when the tissue path-lengths over which the light signal is measured become larger. Thus, the effect will likely have a greater impact on imaging human organs than in small animal applications. The influence of tissue absorption was shown to produce the spectral distortion, an effect amplified by increasing photon path-lengths caused by tissue photon scattering or extended source-to-detector distances. Emission spectra escaping the tissue phantom can be modeled reasonable well using a finite element formulation of diffusion theory, especially for source-detector distances over 2 cm. These spectral changes should be

Manuscript in Press

considered for fluorescence tomography imaging through several centimeters of tissue. Use of spectrally resolved detection allows quantification of this change, and may be the only reliable way to track intensity changes which would otherwise appear erroneous.

ACKNOWLEDGEMENTS

This work was funded by the National Institutes of Health grants RO1 CA109558, RO1 CA69544, U54 CA105480, Philips Research Hamburg, as well as Department of Defense Breast Cancer pre-doctoral fellowship BC051058.

Manuscript in Press

REFERENCES

[1] V. Ntziachristos, J. Ripoll, L. V. Wang, and R. Weissleder, Nature Biotechnology **23,** 313-320 (2005).

[2] V. Ntziachristos, G. Turner, J. Dunham, S. D. Windsor, A. Soubret, J. Ripoll, and H. A. Shih, Journal of Biomedical Optics **10,** 0640071--640078 (2005).

[3] W. Wang, S. Ke, Q. Wu, C. Charnsangavej, M. Gurfinkel, J. G. Gelovani, J. L. Abbruzzese, E. M. Sevick-Muraca, and C. Li, Molecular Imaging: Official Journal of the Society for Molecular Imaging **3,** 343-51 (2004).

[4] G. Zacharakis, J. Ripoll, R. Weissleder, and V. Ntziachristos, IEEE Transactions on Medical Imaging **24,** 878-885 (2005).

[5] E. E. Graves, J. P. Culver, J. Ripoll, R. Weissleder, and V. Ntziachristos, Journal of the Optical Society of America, A, Optics, Image Science, & Vision **21,** 231-41 (2004).

[6] S. Srinivasan, B. W. Pogue, C. M. Carpenter, P. K. Yalavarthy, and K. D. Paulsen, Med. Phys. **34,** 4545-4557 (2007).

[7] G. M. Turner, G. Zacharakis, A. Soubret, J. Ripoll, and V. Ntziachristos, Optics Letters **30,** 409-411 (2005).

[8] P. K. Yalavarthy, B. W. Pogue, H. Dehghani, and K. D. Paulsen, Med. Phys. **34,** 2085-2098 (2007).

[9] C. M. Carpenter, B. W. Pogue, H. Jiang, H. Dehghani, K. D. Paulsen, W. A. Wells, J. Forero, C. Kogel, J. B. Weaver, S. P. Poplack, and P. A. Kaufman, Optics Letters **32,** 933-935 (2007).

[10] S. C. Davis, B. W. Pogue, R. Springett, C. Leussler, P. Mazurkewitz, S. B. Tuttle, S. L. Gibbs-Strauss, S. S. Jiang, H. Dehghani, and K. D. Paulsen, Rev. Sci. Instr. **79** (2008).

[11] S. R. Arridge, Inverse Problems **15,** R41-R93 (1999).

[12] N. Deliolanis, T. Lasser, D. Hyde, A. Soubret, J. Ripoll, and V. Ntziachristos, Optics Letters **32,** 382-384 (2007).

[13] H. Meyer, A. Garofalakis, G. Zacharakis, S. Psycharakis, C. Mamalaki, D. Kioussis, E. N. Economou, V. Ntziachristos, and J. Ripoll, Applied Optics **46,** 3617-3627 (2007).

[14] S. V. Patwardhan, S. R. Bloch, S. Achilefu, and J. P. Culver, Opt. Exp. **13,** 2564-2577 (2005).

[15] J. Ripoll, R. B. Schulz, and V. Ntziachristos, Physical Review Letters **91,** 5 (2003).

[16] R. B. Schulz, J. Ripoll, and V. Ntziachristos, Optics Letters **28,** 1701-3 (1701).

[17] A. Corlu, R. Choe, T. Durduran, M. A. Rosen, M. Schweiger, S. R. Arridge, M. D. Schnall, and A. G. Yodh, Optics Express **15,** 6696-6716 (2007).

[18] J. Wu, M. S. Feld, and R. P. Rava, Appl. Opt. **32,** 3585-3595 (1993).

[19] A. J. Durkin, S. Jaikumar, N. Ramanujam, and R. Richards-Kortum, Appl. Opt. **33,** 414-423 (1994).

[20] R. Richards-Kortum, R. P. Rava, M. Fitzmaurice, L. L. Tong, N. B. Ratliff, J. R. Kramer, and M. S. Feld, Ieee Transactions on Biomedical Engineering **36,** 1222-1232 (1989).

Manuscript in Press

[21] A. J. Durkin and R. Richards-Kortum, Lasers in Surgery and Medicine **19,** 75-89 (1996).

[22] C. M. Gardner, S. L. Jacques, and A. J. Welch, Appl. Opt. **35,** 1780-1792 (1996).

[23] M. G. Müller, I. Georgakoudi, Q. Zhang, J. Wu, and M. S. Feld, Appl. Opt. **40,** 4633-4646 (2001).

[24] M. S. Patterson and B. W. Pogue, Appl. Opt. **33,** 1963-1974 (1994).

[25] J. Svensson and S. Andersson-Engels, Opt. Exp. **13,** 4263-4274 (2005).

[26] J. Swartling, J. Svensson, D. Bengtsson, K. Terike, and S. Andersson-Engels, Appl. Opt. **44,** 1934-1941 (2005).

[27] D. Y. Paithankar, A. U. Chen, B. W. Pogue, M. S. Patterson, and E. M. Sevick-Muraca, Appl. Opt. **36,** 2260-2272 (1997).

[28] H. B. Jiang, Appl. Opt. **37,** 5337-5343 (1998).

[29] D. J. Hawrysz and E. M. Sevick-Muraca, Neoplasia **2,** 388-417 (2000).

[30] M. J. Eppstein, D. J. Hawrysz, A. Godavarty, and E. M. Sevick-Muraca, Proc. Natl. Acad. Sci. USA **99,** 9619-24 (2002).

[31] V. Ntziachristos and R. Weissleder, Optics Letters **26,** 893-895 (2001).

[32] A. B. Milstein, O. Seungseok, K. J. Webb, C. A. Bouman, Q. Zhang, D. A. Boas, and R. P. Millane, Appl. Opt. **42,** 3081-3094 (2003).

[33] A. Godavarty, A. B. Thompson, R. Roy, M. Gurfinkel, M. J. Eppstein, C. Zhang, and E. M. Sevick-Muraca, J. Biomed. Opt. **9,** 488-96 (2004).

[34] S. C. Davis, H. Dehghani, J. Wang, S. Jiang, B. W. Pogue, and K. D. Paulsen, Optics Express **15,** 4066-4082 (2007).

[35] D. S. Kepshire, S. C. Davis, H. Dehghani, K. D. Paulsen, and B. W. Pogue, Appl. Opt. **46,** 1669-1678 (2007).

[36] S. Jiang, B. W. Pogue, T. O. McBride, M. M. Doyley, S. P. Poplack, and K. D. Paulsen, Journal of Electronic Imaging **12,** 613-620 (2003).

[37] B. Pogue and M. Patterson, J. Biomed. Opt. **11,** 0411021-04110216 (2006).

[38] G. Kostenich, A. Orenstein, L. Roitman, Z. Malik, and B. Ehrenberg, Photochem. & Photobiol. **39,** 36-42 (1997).

[39] H. Dehghani, B. W. Pogue, S. Jiang, B. Brooksby, and K. D. Paulsen, Appl. Opt. **42,** 3117-3128 (2003).

[40] S. A. Prahl.

[41] S. Srinivasan, B. W. Pogue, S. Jiang, H. Dehghani, and K. D. Paulsen, Appl. Opt. **44,** 1858-1869 (2005).

[42] S. C. Davis, B. W. Pogue, H. Dehghani, and K. D. Paulsen, Journal of Biomedical Optics Letters **10,** 1-3 (2005).

[43] A. J. Chaudhari, F. Darvas, J. R. Bading, R. A. Moats, P. S. Conti, D. J. Smith, S. R. Cherry, and R. M. Leahy, Phys. Med. Biol. **50,** 5421-5440 (2005).

[44] H. Dehghani, S. C. Davis, H. Jiang, B. W. Pogue, K. D. Paulsen, and M. S. Patterson, Optics Letters **31,** 365-367 (2006).

[45] J. T. Bushberg, J. A. Seibert, J. Edwin M. Leidholdt, and J. M. boone, *The Essential Physics of Medical Imaging,* 2nd ed. (Lippincott Williams & Wilkins, Philadelphia, 2002).

Manuscript in Press

FIGURE CAPTIONS

Fig. 1. Photographs of phantoms used in this study. A liquid intralipid-based phantom (a) readily allows changing of the fluorophore concentration while gelatin phantoms containing $TiOB_{2B}$ scatterer shown in (b) eliminate the need for an external container. Gelatin phantoms without scattering material were also used to assess the emission spectra without scatter (c).

Fig. 2. Normalized LuTex fluorescence emission as measured in dilute concentration (2μg/ml) in deionized water.

Fig. 3. A diagram of the experimental system with 16 spectrometers (Princeton Instruments Inc, Acton MA) is provided in (a) with a photograph shown in (b). Each spectrograph is coupled to a fiber optic which surrounds a tissue phantom in a circular geometry (c). A homogeneous teflon calibration phantom is pictured here with the 16 fibers coupled to the exterior in a circle.

Manuscript in Press

Fig. 4. Fluorescence emission of 5uM LuTex measured in the multi-spectrometer system in phantoms composed of (a) gelatin and (b) De-ionized water. These spectra represent the non-turbid baselines since neither phantom contained significant scattering media.

Fig. 5. LuTex fluorescence emission experimentally measured at different source-detector distances in homogeneous scattering gelatin and intralipid based phantoms. The

circular domain shown represents a cross-section of the cylindrical phantom, illustrating the input (red arrow) and output measurement sites (blue arrows). For illustration purposes, the intensity (shown as logarithm of intensity) of the diffuse excitation field is plotted in the circular region.

Fig. 6. Fluorescence emission spectra through a liquid phantom of DI water and varying concentrations of intralipid are shown. Only spectra measured through intralipid concentrations of 0.1% and above are shown for the two detectors farthest from the source.

Fig. 7. Absorption coefficients of 100% water and 300 nM LuTex are plotted for discrete wavelengths (green line with data points) with LuTex fluorescence emission (red dotted line) in dilute solution, indicating the overlap in absorption and emission at the shorter wavelengths from 700 to 750 nm.

Fig. 8. Diffusion based modeling of the fluorescence peak through a 60 mm diameter phantom, similar to Fig. 5. The dilute emission spectrum of LuTex is shown as dotted lines, and the calculated emission spectrum from diffuse emission through the region is shown at discrete wavelengths (black circles). Experimental measurements are shown in blue for intralipid liquid phantoms. The circular domain shown represents a cross-section of the cylindrical phantom upon which the intensity (logarithm) of the excitation field calculated from the diffusion equation is plotted for illustration purposes.

Manuscript in Press

Fig. 9. Extinction coefficients of chromophores used in the simulation are shown in (a). These are used to calculate tissue absorption coefficients at any wavelength within the NIR. The simulated domain contains contrasts in the various absorbing constituents, the spatial distributions of which are shown in (b).

Fig. 10. Fluorescence yield of LuTex is calculated from the drug concentration and the fluorescence quantum yield. Based on the concentration of LuTex assumed in Fig. 9, the target fluorescence yield is shown in (a). Reconstructing images from data collected with long-pass filtering can be an intractable problem as shown in (b), while resolving the emitted spectrum allows accurate recovery of the true fluorescence activity, as shown in (c). All images shown are in units of mm^{-1}.

Manuscript in Press

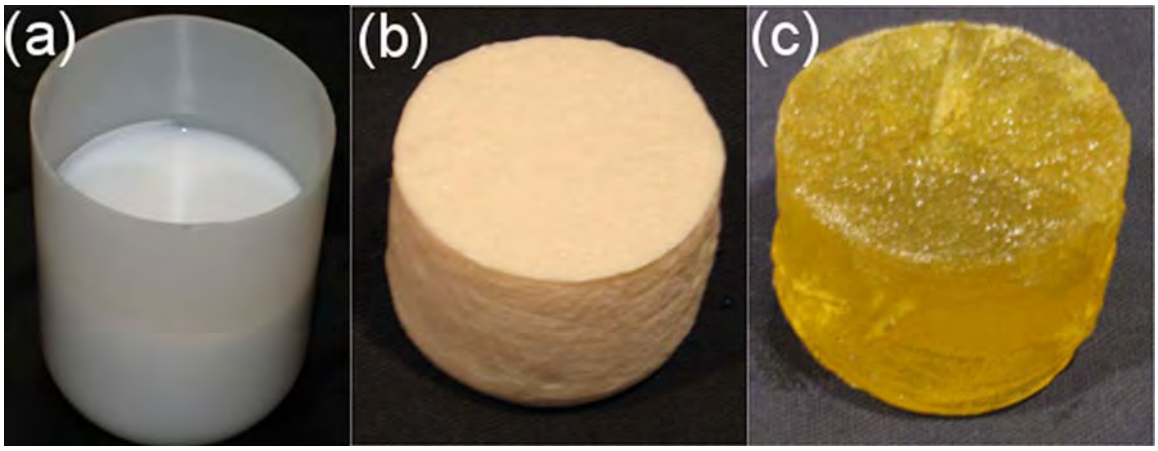

Figure 1.

Press

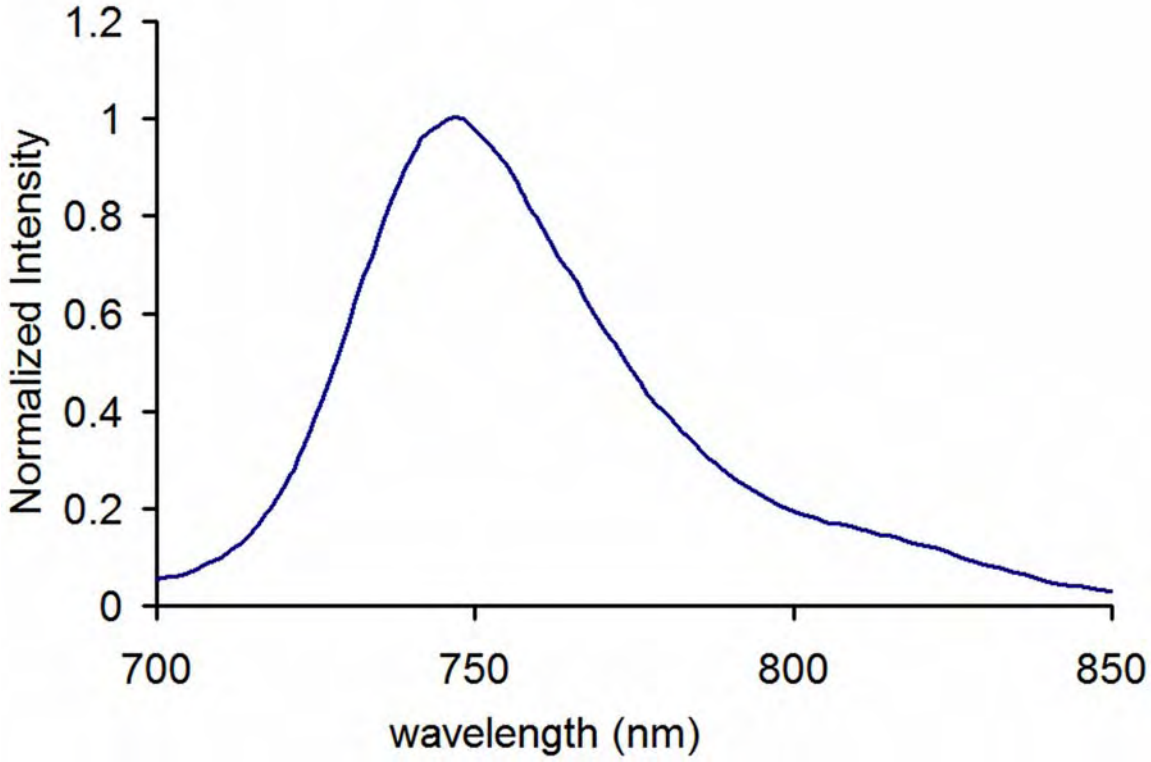

Figure 2.

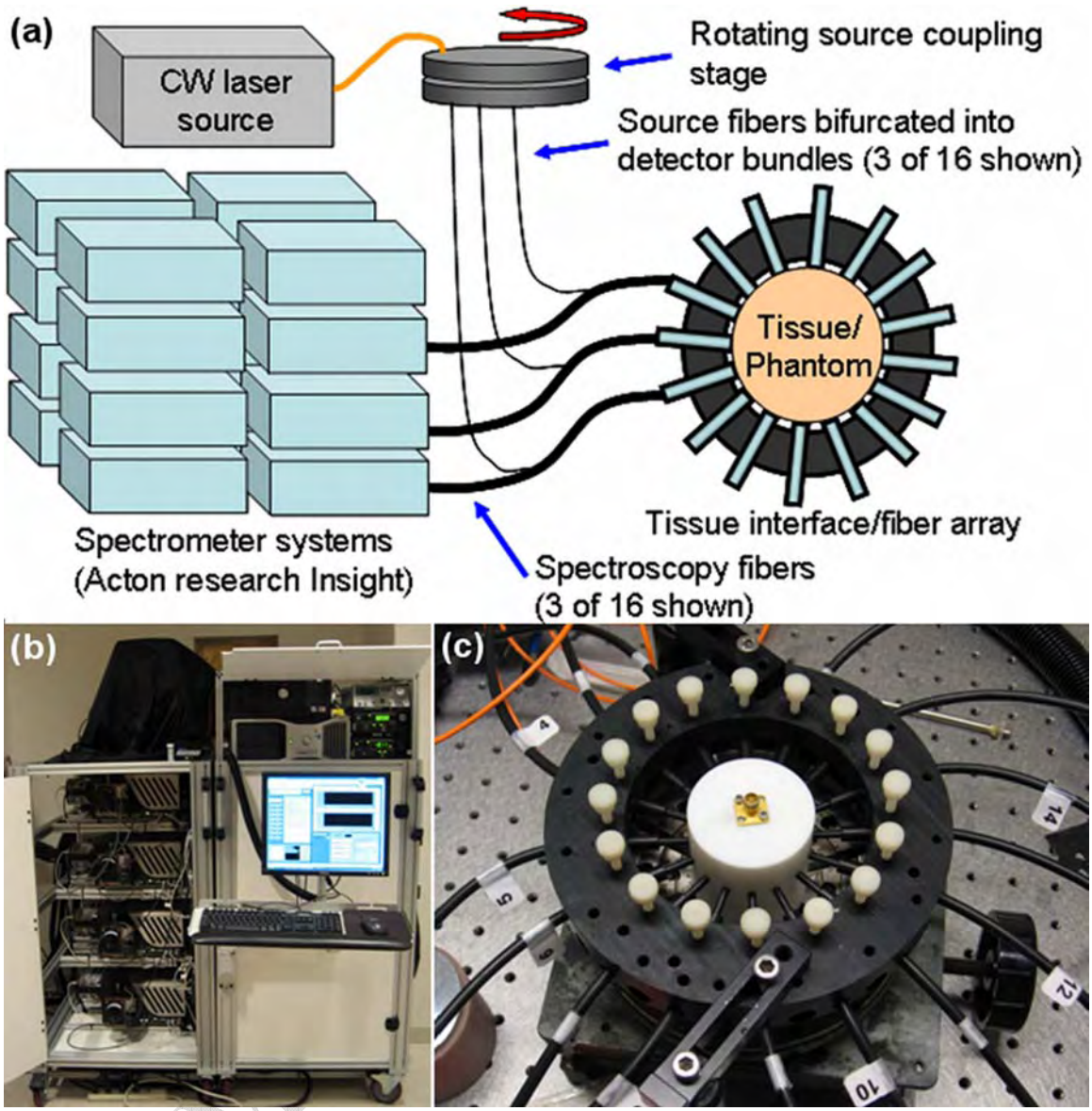
(a)
CW laser source
Rotating source coupling stage
Source fibers bifurcated into detector bundles (3 of 16 shown)
Tissue/ Phantom
Tissue interface/fiber array
Spectrometer systems (Acton research Insight)
Spectroscopy fibers (3 of 16 shown)
(b)
(c)

Figure 3.

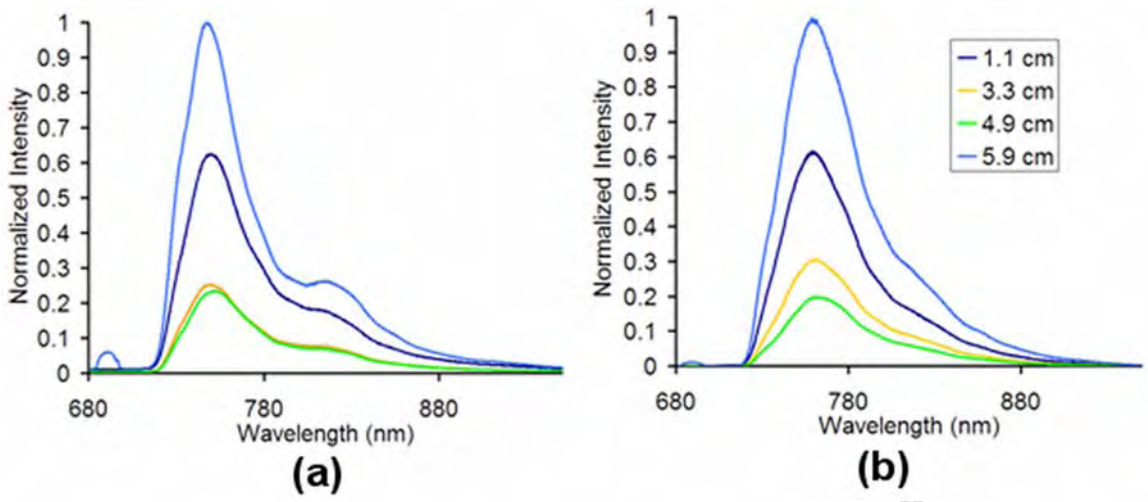

Figure 4.

Manuscript in Press

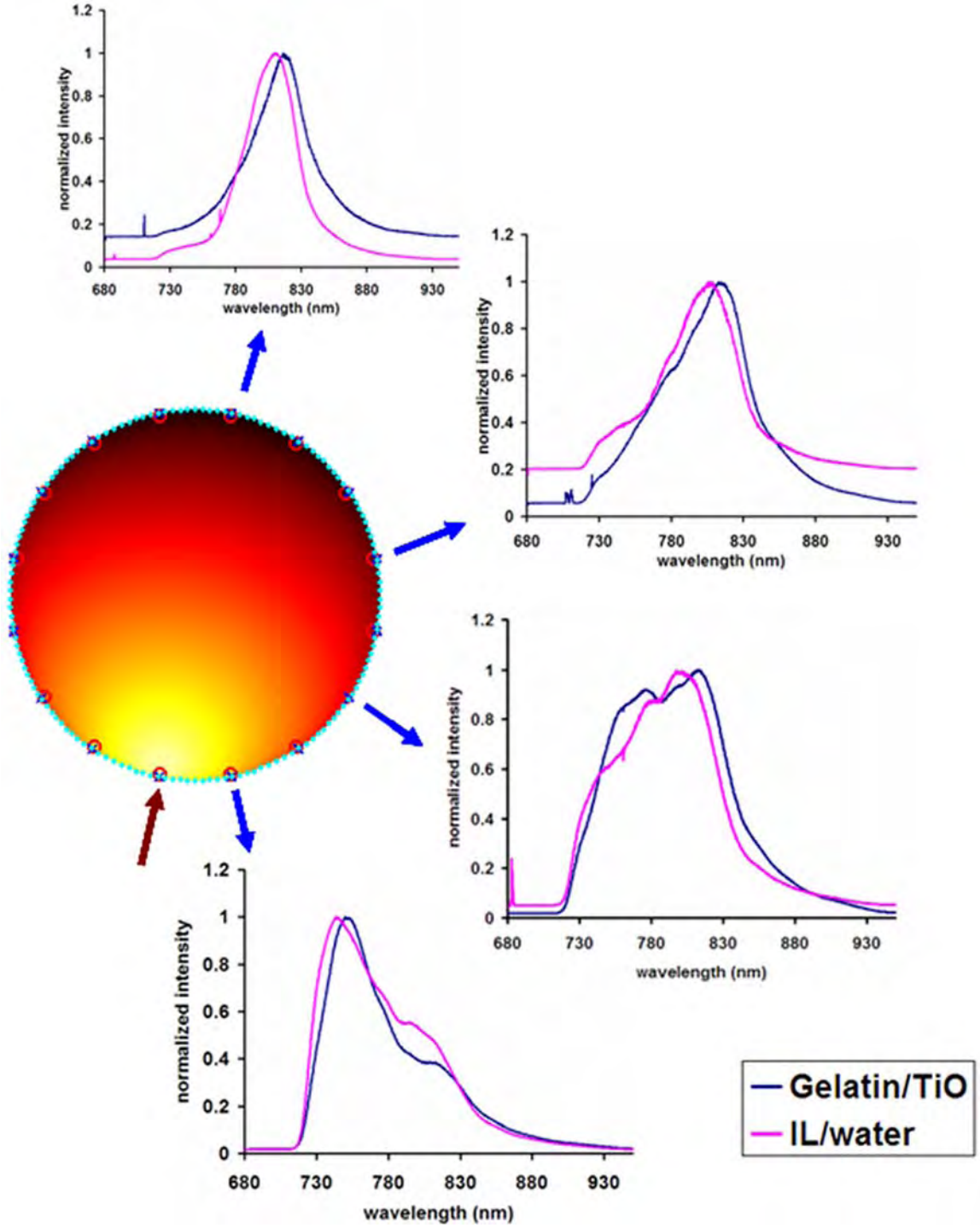

Figure 5.

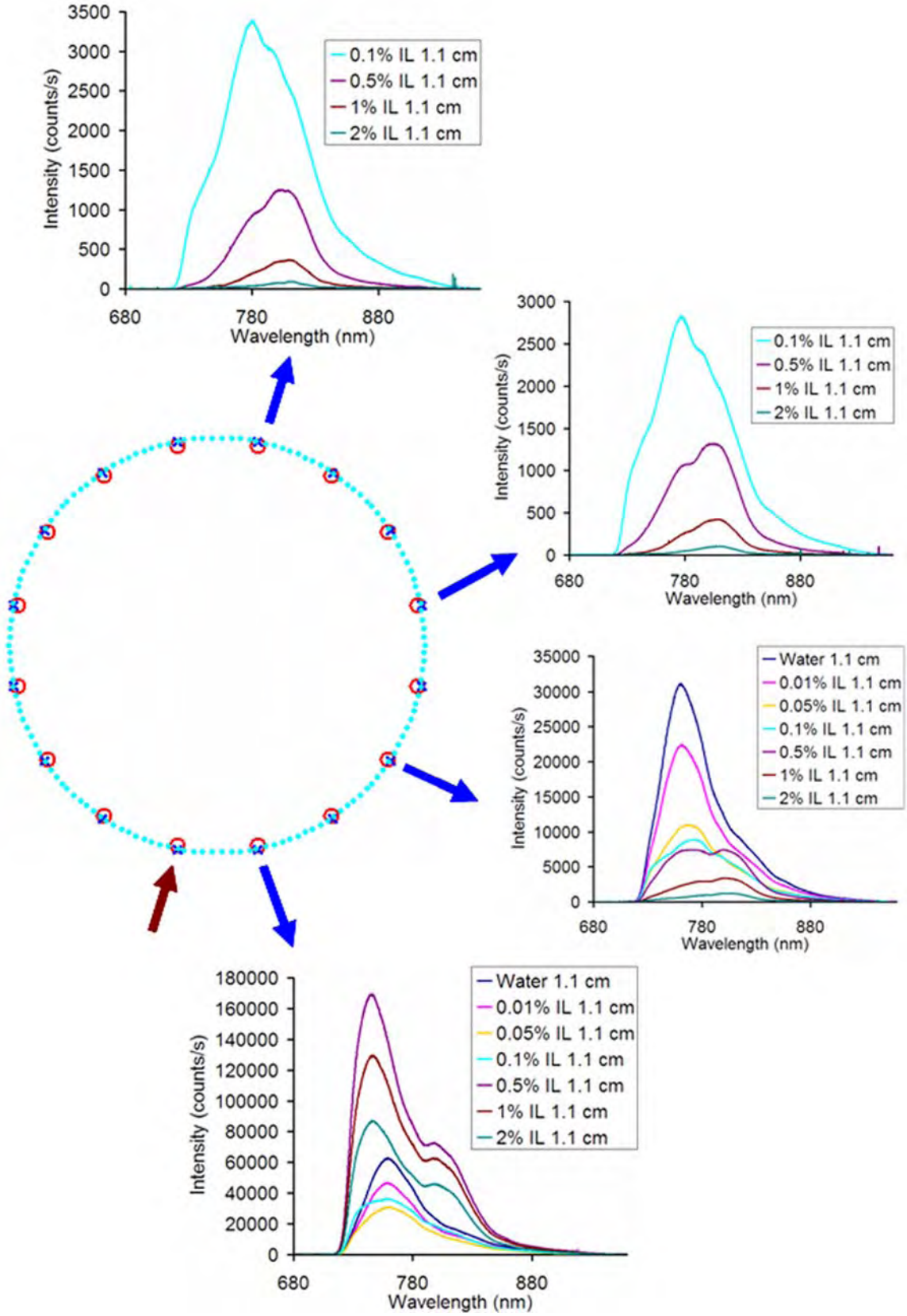
Intensity (counts/s)
Wavelength (nm)
0.1% IL 1.1 cm
0.5% IL 1.1 cm
1% IL 1.1 cm
2% IL 1.1 cm
Water 1.1 cm
0.01% IL 1.1 cm
0.05% IL 1.1 cm

Figure 6.

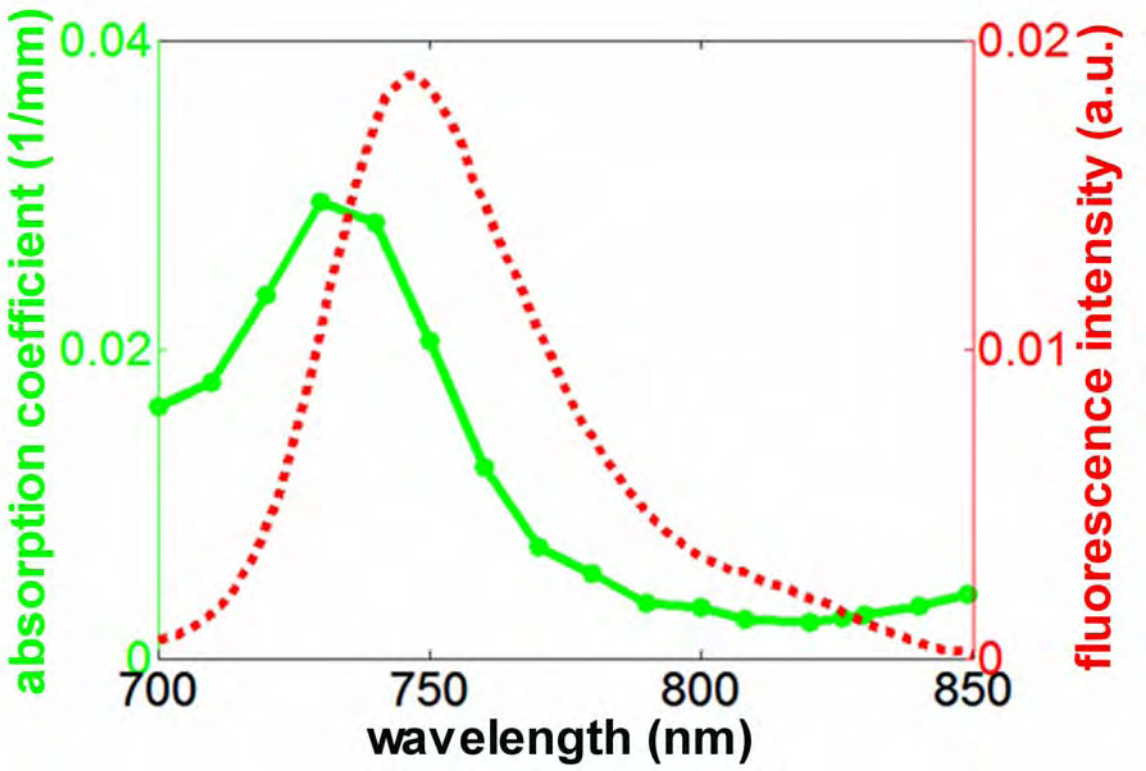

Figure 7.

Manuscript

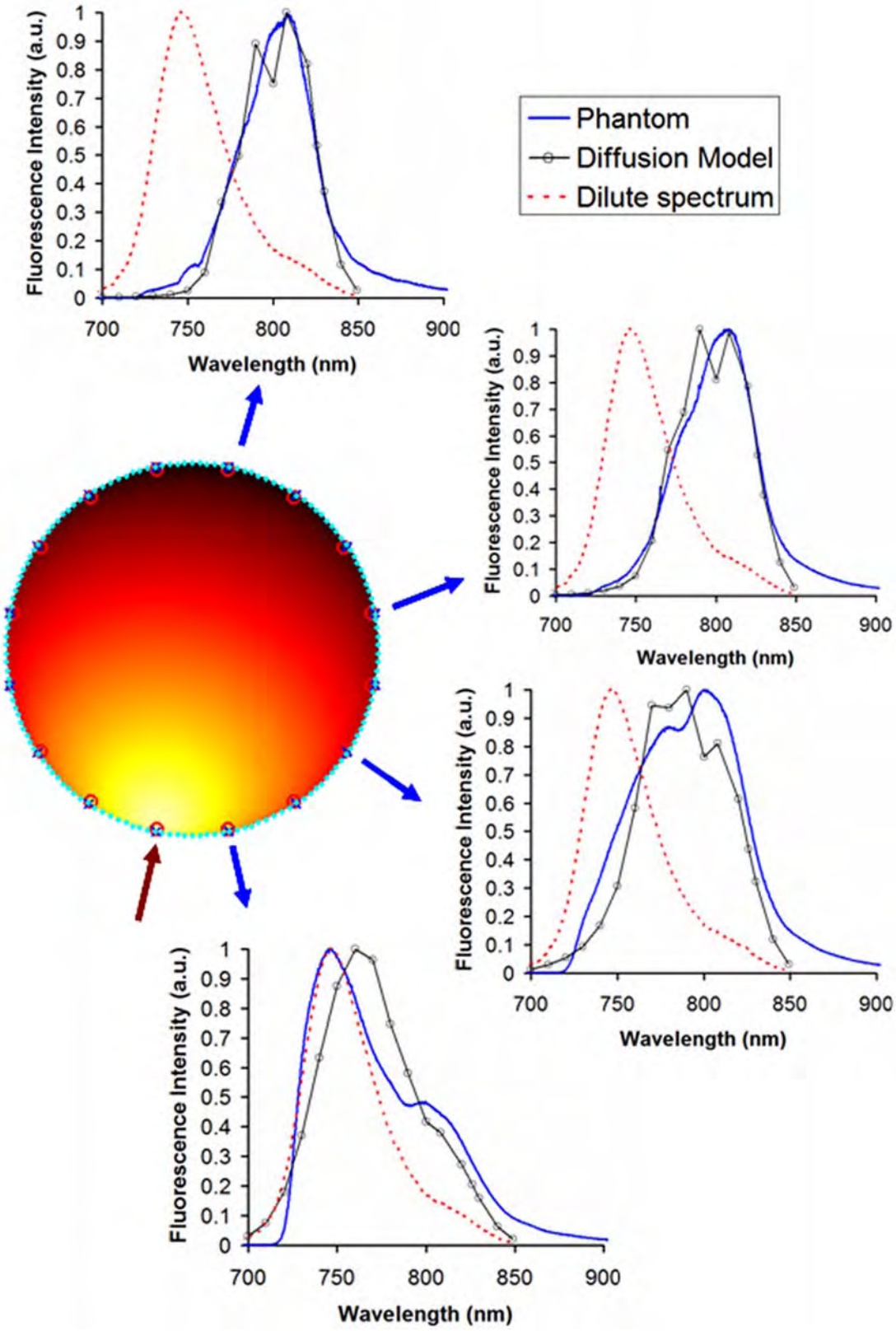
Phantom
Diffusion Model
Dilute spectrum
Fluorescence Intensity (a.u.)
Wavelength (nm)
0
0.1
0.2
0.3
0.4
0.5
0.6
0.7
0.8
0.9
1
700
750
800
850
900

Figure 8.

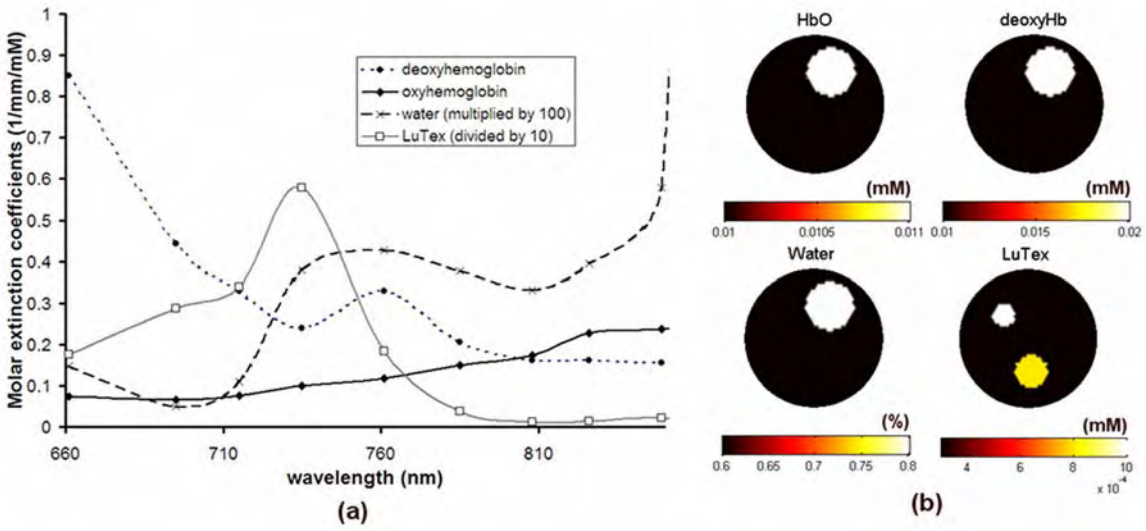

Figure 9.

Manuscript in Press

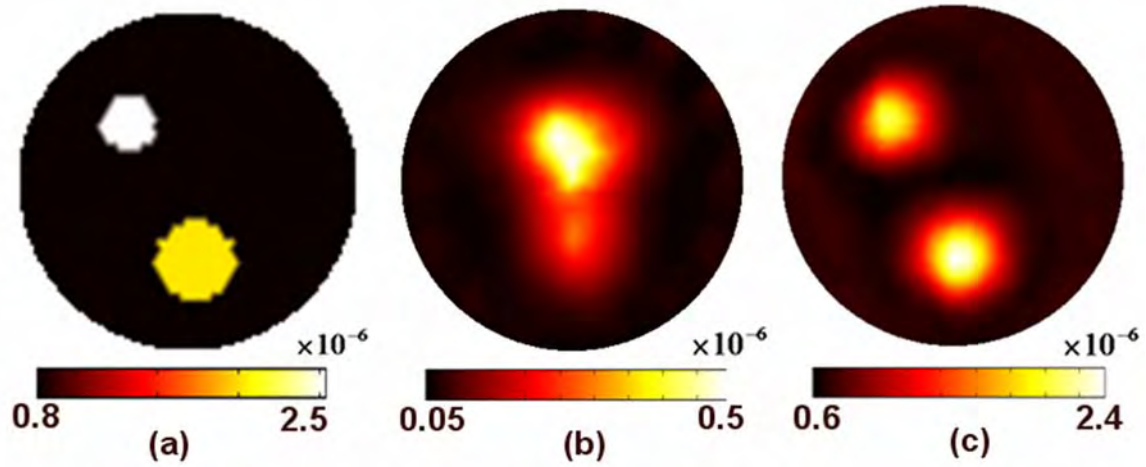

Figure 10.